

# Search for neutrino-induced cascades with 5 years of the AMANDA-II data

## DISSERTATION

zur Erlangung des akademischen Grades  
doctor rerum naturalium  
(Dr. rer. nat.)  
im Fach Physik

eingereicht an der  
Mathematisch-Naturwissenschaftlichen Fakultät I  
Humboldt-Universität zu Berlin

von

Frau Dipl.-Phys. Oxana Actis (geb. Tarasova)  
geboren am 24.01.1981 in Ogudnevo, Gebiet Moskau

Präsident der Humboldt-Universität zu Berlin:  
Prof. Dr. Christoph Marksches

Dekan der Mathematisch-Naturwissenschaftlichen Fakultät I:  
Prof. Dr. Christian Limberg

Gutachter:

1. Prof. Dr. Hermann Kolanoski
2. Prof. Dr. Christopher Wiebusch
3. Dr. Marek Kowalski

eingereicht am: 14. Januar 2008  
Tag der mündlichen Prüfung: 15. April 2008

## Abstract

The Antarctic Muon And Neutrino Detector Array (AMANDA) is a Cherenkov detector deployed in the Antarctic ice cap at the South Pole. We present the analysis of the AMANDA data collected during 1001 effective days of the detector lifetime between the years 2000 and 2004. We focus our search on electromagnetic and hadronic cascades which are produced in charged-current interactions of high-energy electron or tau neutrinos and in neutral-current interactions of neutrinos of any flavor.

There are several advantages associated with the cascade channel in the search for a "diffuse" flux of astrophysical neutrinos. The AMANDA's energy resolution allows us to distinguish between a hard astrophysical spectrum and a soft atmospheric spectrum. In addition, the flux of atmospheric electron neutrinos is lower than that of atmospheric muon neutrinos by one order of magnitude, and the background from downward-going atmospheric muons can be suppressed due to their track-like topology. The low background in this channel allows us to attain a  $4\pi$  acceptance above energies of about 50 TeV.

The number of events observed in this analysis is consistent with the background expectations. Therefore, we calculate an upper limit on the diffuse all-flavor neutrino flux assuming a flavor ratio 1:1:1 at the detection site. A flux of neutrinos with a spectrum  $d\Phi/dE$  falling as  $E^{-2}$  is limited to  $E^2\Phi_{90\%CL} \leq 3.96 \cdot 10^{-7} \text{GeV s}^{-1} \text{sr}^{-1} \text{cm}^{-2}$  at 90% C.L. for a neutrino energy range spanning from 40 TeV to 9 PeV. This upper limit is currently the most sensitive limit on the diffuse all-flavor astrophysical neutrino flux.

### Keywords:

AMANDA, neutrinos, astroparticle physics, cascades

## Zusammenfassung

Das Antarctic Muon And Neutrino Detector Array (AMANDA) ist ein Cherenkov Detektor, der sich im Gletscher der Antarktis am Südpol befindet. Wir präsentieren die Analyse von Daten, die in den Jahren 2000 bis 2004 gesammelt wurden, die einer effektiven Detektorlaufzeit von 1001 Tagen entsprechen.

Die Suche zielt auf den Nachweis von elektromagnetische und hadronische Teilchenschauern, so gennante Kaskaden, die durch Elektron- und Tau-neutrino-wechselwirkung produziert werden können. Die hadronischen Kaskaden können auch über neutrale Ströme Wechselwirkung von Neutrinos aller Arten produziert werden.

Der Kaskadenkanal hat einige Vorteile in der Suche nach einem diffusen Fluss von astrophysikalischen Neutrinos. Durch die gute Energieauflösung des AMANDA Detektors kann man zwischen einem harten astrophysikalische Spektrum und einem weichen atmosphärischen Spektrum unterscheiden. Außerdem ist der atmosphärischen Elektronneutrinos Fluss um eine Größenordnung kleiner als der atmosphärische Myonneutrinofluss. Der Untergrund von atmosphärischem Myonen aus Luftschauern kann unterdrückt werden, weil diese als Spuren im Detektor erscheinen und leicht zu identifizieren sind. Mit der hohen Untergrundunterdrückung ist es möglich die Analyse über einen Raumwinkel von  $4\pi$  für Energien  $\geq 50$  TeV zu erstrecken.

Die Anzahl von gefundenen Ereignissen in dieser Analyse stimmt mit der Erwartung von Hintergrundereignissen überein. Deshalb berechnen wir eine obere Grenze für den diffusen Neutrinofluss aller Neutrinoarten, unter der Annahme, dass alle Neutrinoarten im Verhältnis 1:1:1 auftreten. Die obere Grenze für einen Neutrinofluss im Energiebereich von 40 TeV bis 9 PeV mit einem Spektrum von  $d\Phi/dE \propto E^{-2}$  ist  $E^2\Phi_{90\%CL} \leq 3.96 \cdot 10^{-7} \text{GeV s}^{-1} \text{sr}^{-1} \text{cm}^{-2}$  bei einem Konfidenzniveau von 90%. Dies ist momentan die niedrigste Grenze für einen diffusen Neutrinofluss aller Neutrinoarten.

### Schlagwörter:

AMANDA, Neutrino, Astroteilchenphysik, Kaskaden



# Contents

<b>1</b>	<b>Introduction</b>	<b>3</b>
<b>2</b>	<b>High-Energy Neutrinos in Astroparticle Physics</b>	<b>5</b>
2.1	High-Energy Cosmic Rays . . . . .	5
2.2	Neutrino Production and Physical Properties . . . . .	10
2.2.1	Neutrino Production . . . . .	10
2.2.2	Neutrino Oscillations . . . . .	11
2.3	Gamma-Ray Astronomy . . . . .	13
2.4	Possible Sources of High-Energy Neutrinos . . . . .	14
2.4.1	Active Galactic Nuclei . . . . .	15
2.4.2	Gamma Ray Bursts . . . . .	17
2.4.3	Supernova Remnants . . . . .	18
2.4.4	Exotic Neutrino Sources . . . . .	18
2.4.5	Atmospheric Neutrinos and Muons . . . . .	19
2.5	Diffuse High-Energy Neutrinos . . . . .	20
<b>3</b>	<b>High-Energy Neutrino Detection</b>	<b>23</b>
3.1	Neutrino Interactions . . . . .	23
3.2	Event Signatures and Cherenkov Radiation . . . . .	26
3.2.1	Event topologies . . . . .	26
3.2.2	Cherenkov radiation . . . . .	28
3.3	Physics of Cascades . . . . .	29
3.3.1	Electromagnetic Cascades . . . . .	29
3.3.2	Hadronic Cascades . . . . .	31
<b>4</b>	<b>The AMANDA Detector</b>	<b>33</b>
4.1	AMANDA Set-Up . . . . .	33
4.2	DAQ and Trigger systems . . . . .	37
4.3	Digital Optical Modules for IceCube . . . . .	38
4.4	Optical Properties of the Ice . . . . .	40

---

<b>5</b>	<b>Data Samples</b>	<b>45</b>
5.1	Experimental Data . . . . .	45
5.2	Signal Event Simulation . . . . .	46
5.3	Atmospheric Muon Background Simulation . . . . .	48
5.4	The AMANDA Detector Simulation . . . . .	50
<b>6</b>	<b>Event Reconstruction</b>	<b>53</b>
6.1	Hit Cleaning . . . . .	54
6.2	A First-Guess Algorithm for Cascades . . . . .	56
6.3	Vertex Position Reconstruction . . . . .	57
6.4	Energy Reconstruction . . . . .	61
6.5	Iterative Muon Likelihood Fit . . . . .	63
<b>7</b>	<b>Data Analysis</b>	<b>65</b>
7.1	First-Level Filter . . . . .	66
7.2	Second-Level Filter . . . . .	68
7.2.1	Likelihood Vertex Position Reconstruction . . . . .	68
7.2.2	Energy Likelihood Reconstruction . . . . .	69
7.3	Additional Quality Cuts . . . . .	69
7.4	Final Selection . . . . .	73
7.4.1	Discriminating Parameter $Q_s$ . . . . .	73
7.4.2	Cut Optimization . . . . .	76
<b>8</b>	<b>Systematic Uncertainties</b>	<b>81</b>
8.1	Ice Properties and Photon Propagation . . . . .	81
8.1.1	Photon-Propagation Simulation . . . . .	82
8.1.2	PTD and PHOTONICS Comparison . . . . .	84
8.2	Photo-Multiplier Efficiency . . . . .	86
8.3	Other Possible Systematic Effects . . . . .	88
8.3.1	Summary of systematic uncertainties . . . . .	90
<b>9</b>	<b>Results</b>	<b>93</b>
9.1	Final Sample . . . . .	93
9.2	Detector Effective Volume . . . . .	95
9.3	Detector Effective Area . . . . .	98
9.4	Limits on the Diffuse Flux of Neutrinos . . . . .	99
9.4.1	Event Upper Limit . . . . .	100
9.4.2	Flux Upper limit . . . . .	101
<b>10</b>	<b>Summary</b>	<b>107</b>
<b>11</b>	<b>Outlook</b>	<b>109</b>

## CONTENTS

---

vii

A The Remaining Events	125
B PTD and Photonics Comparison	127





# List of Figures

2.1	Differential energy spectrum of cosmic rays observed by different experiments. The picture is adapted from [Hil06]. . . .	6
2.2	Schematic view of Fermi acceleration across a shock front in interstellar gas. . . . .	8
2.3	The gamma-ray energy as a function of the redshift, with a list of the dominant processes responsible for attenuation. Figure adapted from [LM00]. . . . .	15
2.4	Schematic view of the unification model for AGN. According to the different viewing angle, different morphologies are observed. Picture adapted from [Tlu03]. . . . .	16
2.5	The flux for atmospheric muons and muon and electron neutrinos, weighted with $E^3$ . The solid line corresponds to the detailed MC simulation, while the dashed ones follow from analytical calculations. This picture was adapted from [GIT96].	20
2.6	Expected $(\nu_\mu + \bar{\nu}_\mu)$ fluxes for diffuse emission from known and expected sources. See text for details. The picture was adapted from [LM00]. . . . .	22
3.1	Charged-current and neutral-current neutrino cross sections. Note the Glashow-resonance peak at $E_\nu \sim 6.3$ PeV. Figure adapted from [Kow04]. . . . .	25
3.2	Charged-current and neutral-current interactions for neutrinos of all three flavors. . . . .	27
3.3	The event topologies (track- and cascade-like) for the products of neutrino interactions. . . . .	28
3.4	The ratio of the hadronic and the electromagnetic light output for different cascade energies and injected particles. The pictures are adapted from [Kow]. . . . .	31

---

4.1	The AMANDA-A and AMANDA-II detectors. On the right, an Optical Module is shown in order to illustrate its mechanical design. The figure was adapted from [AMAA]. . . . .	35
4.2	A schematic view of the AMANDA Data Acquisition System. . . . .	37
4.3	A schematic view of an IceCube Digital Optical Module. . . . .	39
4.4	Top: the effective scattering coefficient $1/\lambda_{scat}^{eff}$ and the absorption coefficient $1/\lambda_{abs}$ of the ice surrounding the AMANDA detector as functions of the depth. Bottom: the wavelength dependence of $1/\lambda_{abs}$ at two different depths within 40 m from the AMANDA-detector center. Pictures taken from [A <sup>+</sup> 06b]. . . . .	41
5.1	A schematic overview of the Monte Carlo simulation chain employed for our analysis. . . . .	46
5.2	Left: Reconstructed cascade energy for various background Monte Carlo samples. Right: Ratio between the reconstructed energy distribution of the background sample optimized for medium energies and the MC sample simulated using standard settings. All events shown here have passed the vertex likelihood cut $L_{vertex} < 7.1$ (see Chapter 6). . . . .	49
6.1	The ADC amplitude distribution as a function of Time Over Threshold (TOT). . . . .	55
6.2	Dependence of the arrival time probability density functions on the time residual. The left plot shows the $p(t, d)$ distribution for $d=20$ m and the right one the same parameter for $d=100$ m. The parametrization for the residual time (solid line) has been obtained in [Kow99] fitting these distributions. . . . .	58
6.3	The resolution results of the mpe-likelihood vertex reconstruction for the $x, y, z$ vertex position coordinates in the AMANDA detector. . . . .	60
6.4	The resolution for the $x$ and $z$ vertex coordinates obtained from single photo-electron likelihood reconstruction (blue line) compared to the resolution obtained from multi photo-electron likelihood reconstruction (red curve). . . . .	61
6.5	The performance of the energy reconstruction with AMANDA using phit-pnohit algorithm. Left: the energy resolution for 1 TeV cascades. Right: The reconstructed energy resolution as a function of the cascade energy. . . . .	62
7.1	The block-diagram structure of the analysis described in this chapter. . . . .	66

7.2	The parameters returned by the $c$ -first reconstruction. Left: fraction of early hits over the total number of hits. Right: direct hits in the 200 ns time window. Experimental data, signal and background MC distributions are shown. . . . .	67
7.3	Reconstructed cascade energy for data of different years used in the analysis. . . . .	68
7.4	The mpe-likelihood vertex reconstruction parameter. The events shown here passed the first-level cuts. Experimental data, background MC and a hypothetical $E^{-2}$ electron neutrino signal are shown in the plot. . . . .	69
7.5	Left: reconstructed cascade energy for events which passed the vertex likelihood cut. Right: reconstructed energy for events which passed all quality cuts. Both pictures show the comparison of experimental data (20% of the full 5-year sample) to atmospheric muon background MC. . . . .	70
7.6	Energy likelihood reconstruction quality parameter as a function of the reconstructed cascade energy. The plots show an $E^{-2}$ signal MC, atmospheric muon background MC and experimental data (from left to the right). The red line is the two-dimensional cut defined in Eq. (7.1). . . . .	71
7.7	The reconstructed cascade vertex radial distance between the detector center and the vertex as a function of the reconstructed cascade energy. An $E^{-2}$ ( $\nu_e + \bar{\nu}_e$ ) signal, background MC and experimental data are shown. The red line corresponds to the two-dimensional cut of Eq. (7.2). . . . .	72
7.8	Experimental data, $E^{-2}$ ( $\nu_e + \bar{\nu}_e$ ) signal and background simulation as a comparison for the three parameters used to build the quality function, $Q_s$ . . . . .	74
7.9	Distribution of the discriminating parameter $Q_s$ . The distributions of experimental data, signal and background MC are normalized to 1. Events shown passed all the quality selection criteria defined before the final level selection. . . . .	76
7.10	The reconstructed cascade energy for the quality parameter cut $Q_s^{cut} > 0.92$ . The distributions of signal and background MC are normalized to the 20% of the experimental data shown here. The power-law fit to the background, shown as a black solid line, was used for the cut optimization. . . . .	78

---

7.11	Left: Average upper limit for a $\nu_e$ flux as a function of the energy cut. The distribution is shown for $Q_s^{cut} > 0.92$ . Right: The average upper limit, according to the energy optimization, is shown as a function of $Q_s^{cut}$ . The minimum corresponds to the best average upper limit for a $\nu_e$ flux equal to $2.7 \cdot 10^{-7} (E/GeV)^{-2}/(GeV s sr cm^2)$ . . . . .	79
8.1	The difference between the ice modeling concepts of PTD and PHOTONICS is shown. In PTD (left plot) each Optical Module has its own ice properties and the photon detected by each individual module is assumed to propagate through an ideal isotropic ice with the same properties of the detecting module. In PHOTONICS (right plot), the correct anisotropic ice properties are taken into account. . . . .	83
8.2	Left: a comparison of the reconstructed cascade energy for the PTD, PHOTONICS <sub>M</sub> and PHOTONICS <sub>A</sub> signal Monte Carlo samples. Right: the $(\nu_e + \bar{\nu}_e)$ effective area. For both distributions, the shown events passed all analysis cuts. . . . .	85
8.3	Left: photon collection efficiencies of Optical Modules normalized to the average efficiency for 2001 data. Right: average sensitivity for each string. Pictures are adapted from [Lan05].	87
8.4	Left: photon collection efficiencies of Optical Modules normalized to the average efficiency for 2003 data. Right: difference between the photon collection efficiency of the Optical Modules obtained from the data collected in years 2001 and 2003. . . . .	88
9.1	Reconstructed cascade energy distributions for experimental data, $E^{-2} (\nu_e + \bar{\nu}_e)$ signal and background Monte Carlo. . . . .	93
9.2	Effective volume for $\nu_e, \nu_\mu$ and $\nu_\tau$ as a function of the neutrino energy. . . . .	96
9.3	Effective volume for $\nu_e, \nu_\mu$ and $\nu_\tau$ as a function of the neutrino energy and the zenith angle. The two upper plots show the effective volume for neutrinos coming from the southern hemisphere and the plots below correspond to events from the northern hemisphere which propagated through the Earth. . . . .	97
9.4	Left: the effective neutrino area of the detector as a function of the neutrino energy. Here, distributions for all neutrino (and anti-neutrino) flavors are shown. Right: the effective area for $\bar{\nu}_e$ in the energy region of the Glashow resonance. . . . .	98

9.5	The AMANDA detector effective neutrino area is shown as a function of the neutrino energy for four different ranges of the zenith angle. Distributions for electron, muon and tau neutrinos are shown separately. The tau regeneration effect is mainly visible in the two lower plots, which correspond to the up-going neutrinos. . . . .	100
9.6	The upper limits on a diffuse neutrino flux from sources with an $E^{-2}$ energy spectrum are shown for muon and all-flavor analysis. All-flavor upper limits were divided by a factor of three, assuming the flavor ratio at the Earth to be $\phi_{\nu_e+\bar{\nu}_e} : \phi_{\nu_\mu+\bar{\nu}_\mu} : \phi_{\nu_\tau+\bar{\nu}_\tau} \approx 1 : 1 : 1$ . . . . .	102
9.7	Flux prediction for several models of astrophysical neutrino sources (left) and atmospheric neutrinos due to charm production (right). . . . .	105
A.1	The six events of the experimental data sample which have passed all the analysis selections are displayed from the side of the AMANDA detector. . . . .	126
B.1	The number of hits (left) and the number of channels (right) as a comparison of the three signal Monte Carlo samples generated with PTD (blue), PHOTONICS <sub>M</sub> (red) and PHOTONICS <sub>A</sub> (green) tables. . . . .	127
B.2	Distributions of the $x$ , $y$ and $z$ reconstructed cascade vertex coordinates for the PTD, PHOTONICS <sub>M</sub> and PHOTONICS <sub>A</sub> Monte Carlo. All events shown in these distributions passed the vertex likelihood cut $L_{vertex} < 7.1$ . . . . .	128
B.3	Resolution of the $x$ , $y$ and $z$ coordinates for PHOTONICS <sub>M</sub> , PHOTONICS <sub>A</sub> and PTD. . . . .	128



# List of Tables

5.1	Run periods, effective detector up-time and number of triggered events used for the multi-year (2000-2004) cascade search performed in this work. . . . .	46
5.2	Summary of the atmospheric muon background samples used in this analysis. . . . .	50
7.1	The efficiencies of the analysis for experimental data, several types of background and an $E^{-2}$ ( $\nu_e + \bar{\nu}_e$ ) signal. . . . .	66
8.1	Summary of $E^{-2}$ ( $\nu_e + \bar{\nu}_e$ ) signal expectations, expected rates from atmospheric $\nu_e$ and $\nu_\mu$ and atmospheric muons for Monte Carlo samples produced with PHOTONICS <sub>M</sub> and PHOTONICS <sub>A</sub> . All numbers are shown as percentage of the rates obtained using PTD simulations. . . . .	85
9.1	The observables and the reconstructed quantities of the six experimental events which passed all analysis cuts. . . . .	94
9.2	The event rates for experiment and expected background from atmospheric muons, electron and muon neutrinos including the systematic uncertainties. . . . .	95
9.3	The summary of expected event rates from various astrophysical and atmospheric prompt neutrino models. The assumed event upper limit with all systematic uncertainties is $\mu_{90\%} = 5.28$ . . . . .	104
B.1	Summary of space resolution for Monte Carlo produced with PTD and PHOTONICS. . . . .	129





# Chapter 1

## Introduction

Astronomy is among the oldest sciences which fascinated humanity: the nature of the cosmos has always been the subject of direct observations and theoretical speculations.

From ancient times to the end of the nineteenth century, the only mean to investigate the heavens has been the observation of photons at optical wavelengths. During the last century, new powerful methods have been developed, and nowadays the detection spectrum for photons spans from radio wavelengths to x-rays and gamma rays. Photon astronomy has been spectacularly successful, and today we know about the cosmic microwave background and the existence of gamma ray bursts and active galactic nuclei.

Nevertheless, the investigation of photons leave unanswered the main important questions of astrophysics: what are the sources which originate the observed flux of high-energy particles reaching the Earth's atmosphere, the so-called cosmic rays, and the mechanisms responsible for the acceleration of the latter.

Direct measurements of cosmic rays do not allow us to localize their origin, since their trajectories are deflected by interstellar magnetic fields. However, cosmic rays are produced in association with photons and neutrinos, which are obviously not affected by any magnetic interaction. Although photon astronomy proves successful for analyzing the spectrum of cosmic rays at intermediate energies, above a few TeV gamma rays interact with the cosmic microwave background, producing electron-positron pairs. Therefore, the sky is opaque to high-energy gamma rays.

Neutrinos can be considered the privileged astrophysical messengers for the investigation of the cosmic-ray spectrum at very-high energies: carrying no electromagnetic charge and being weakly interacting, they can reach the Earth's atmosphere without being deflected, and could give us a unique insight in the properties of the galactic and extragalactic sources generating

cosmic rays. Unfortunately, for the same reasons, they are elusive particles, and peculiar detection methods have to be developed. Due to the small neutrino cross section, a neutrino detector has to employ a huge target mass of the order of giga-tons.

The first attempts to use neutrinos in the context of astroparticle physics date back the 1960's, when it was suggested that the ocean could represent a suitable medium for the detection of neutrinos with energies ranging from the GeV to the PeV region. The pioneering experiment BAIKAL [A<sup>+</sup>06c] is operating since more than 10 years, and recently the ANTHARES [A<sup>+</sup>05c] and NEMO [A<sup>+</sup>07b] telescopes started their operations in the Mediterranean sea. The AMANDA detector, instead, was built between 1995 and 2000 in a layer of ice close to the geographical South Pole, and recently it became part of the IceCube observatory currently under construction.

Neutrino searches can follow two different strategies. The first possibility is to search for neutrino emission from point-like sources. The second one is to focus on neutrino detection from unresolved sources; it becomes essential when the neutrino flux from a particular source is too small to be detected by point-source techniques. The combination of signals coming from different sources isotropically distributed across the Universe can result in a detectable neutrino signal.

The topic of our analysis is the search for the diffuse flux of astrophysical neutrinos using the data collected by the AMANDA telescope from 2000 to 2004. In particular, we focus our work on the reconstruction of electromagnetic and hadronic cascades induced by neutrinos of all flavors.

The outline of this dissertation is as follows. After giving in Chapter 2 a brief overview of high-energy astrophysics, we discuss in Chapter 3 the principles of neutrino detection. Next, in Chapter 4, the features of the AMANDA detector are introduced. The experimental data sample and the Monte Carlo simulation performed for this analysis are described in Chapter 5. Chapter 6 deals with the algorithms used for the reconstruction of neutrino-induced cascade-like events. The analysis performed with the 5 years of the AMANDA data is described in Chapter 7, and the estimate of the systematic error for the analysis is discussed in Chapter 8. We show the results obtained in our analysis in Chapter 9. Finally, Chapter 10 contains our summary and conclusions and Chapter 11 is devoted to an outlook.

# Chapter 2

## High-Energy Neutrinos in Astroparticle Physics

In this chapter we discuss the basic concepts of astroparticle physics, with special emphasis on the role played by high-energy neutrinos.

The existence of a high-energy neutrino flux was suggested by the investigation of high-energy cosmic rays and their possible sources, described in Section 2.1. In Section 2.2 we discuss production mechanisms and physical properties of high-energy neutrinos. Section 2.3 deals with gamma-ray astronomy and its relation to high-energy neutrino physics. In Section 2.4 we give an overview of all the existing models for galactic and extragalactic neutrino production, showing the related theoretical predictions. Finally, the expectations for the detectable diffuse neutrino flux are discussed in Section 2.5.

### 2.1 High-Energy Cosmic Rays

High-energy cosmic rays (CRs) are charged particles which move through the space with a velocity close to the speed of light. Their origin is currently one of the major unsolved mysteries of astrophysics, even if researchers are moving closer to a solution. CRs consist of about 85% protons, 14% alpha particles (helium nuclei), 1% electrons and other elementary particles, as well as a tiny fraction of nuclei heavier than helium. Three categories of CRs are recognized: galactic, extragalactic and low-energy solar CRs ejected by the Sun during solar flares.

The energies at which CRs have been observed range from  $10^7$  eV up to about  $10^{20}$  eV. High-energy CRs come from all parts of the sky and, for energies below  $10^{19}$  eV, their original directions are fully randomized by

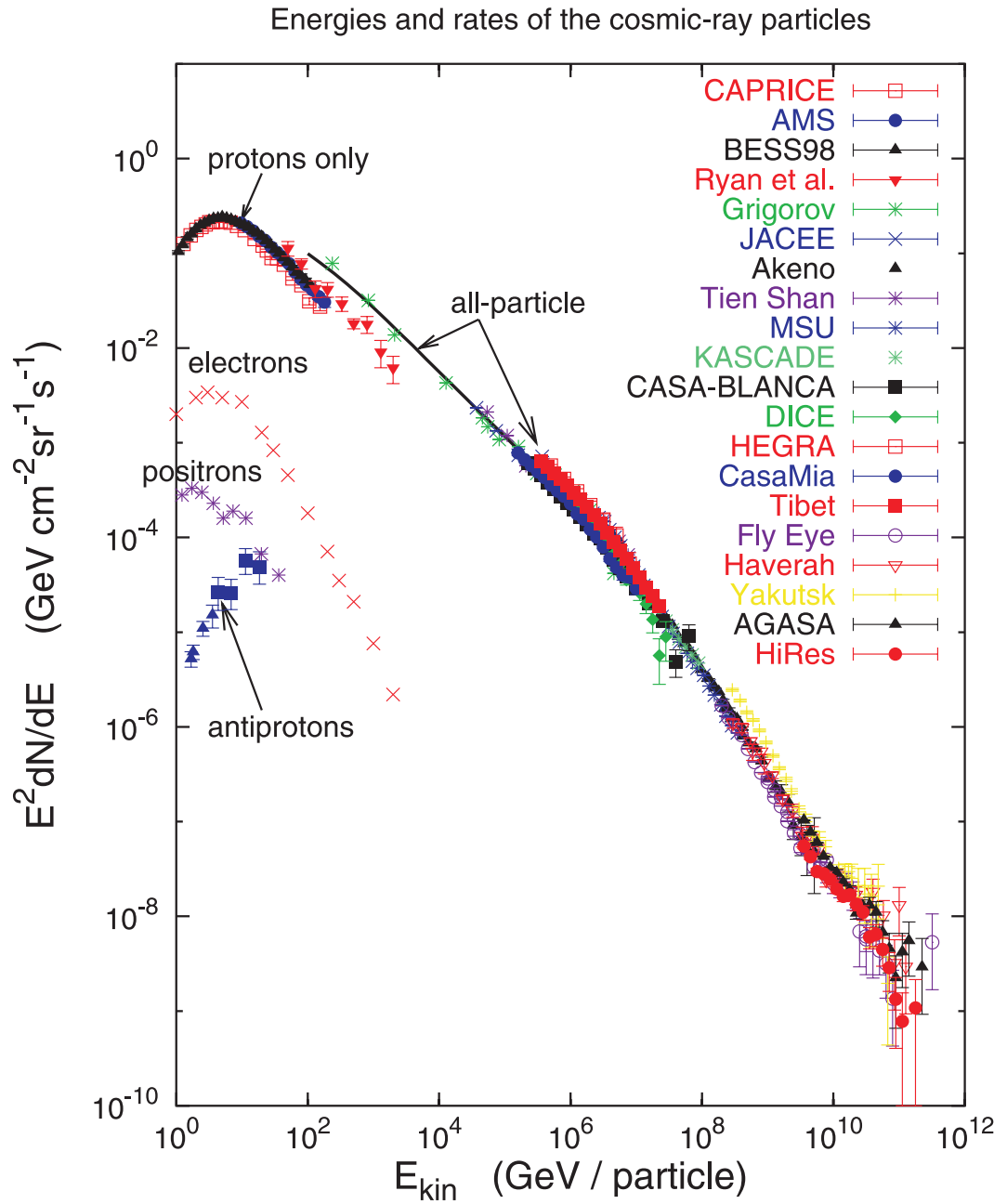


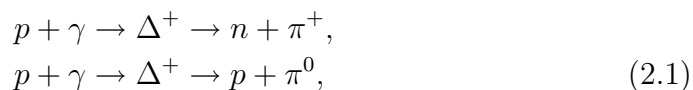
Figure 2.1: Differential energy spectrum of cosmic rays observed by different experiments. The picture is adapted from [Hil06].

galactic and intergalactic magnetic fields. For this reason, it is not possible to use the observed direction of CRs to identify their sources.

Figure 2.1 shows the differential energy spectrum of CRs. The spectrum follows a broken power law,  $dN/dE \propto E^{-\gamma}$ , with a spectral index  $\gamma \sim 2.7$  up to an energy of about  $3 \cdot 10^{15}$  eV. Above this energy the spectral index changes abruptly to  $\gamma \sim 3.0$ , a phenomenon known as spectral knee. The change in the spectral slope at the knee is generally related to the transition of dominating CR sources from galactic to extragalactic ones. At energies of  $3 \cdot 10^{18}$  eV the slope of the spectrum changes back to  $\gamma \sim 2.7$ . This change of the slope is known as spectral ankle.

Several experiments, some of which are indicated in Figure 2.1, have contributed to the present knowledge of the CR energy spectrum, and many others are going to take place to help to unravel the enigma of galactic and extragalactic CRs. On the one hand, it is possible to explore the low-energy part of the spectrum using primary CRs, which can be directly detected only by high-precision instruments above the Earth's atmosphere, as balloon experiments and satellites: two examples are represented by EGRET [H<sup>+</sup>99] and GLAST [D<sup>+</sup>00]. On the other hand, high-energy CRs, after colliding with atoms and molecules in the upper atmosphere, generate secondary particle showers, which are used for indirect measurements through detectors located on the Earth's surface.

Particles with energies higher than  $10^{19}$  eV cause the main important questions of astrophysics which do not have an answer yet: what is the origin of these particles and how they acquire their energies. Nowadays there is no available theoretical model for explaining the mechanism responsible for the acceleration of ordinary particles to such energies <sup>1</sup>. Moreover, the sources of particles with energies above  $10^{19}$  eV must be relatively close, because CRs at these energies interact with the 2.7 K relic cosmic microwave background producing pions:



a fact which results in a reduction of the energy of the original CRs. This effect was predicted in 1966 by Greisen, Zatsepin and Kuz'min and is known as the GZK cut-off [Gre66, ZK66]: beyond an energy of about  $4 \cdot 10^{19}$  eV, no CRs should be observed. The AGASA [H<sup>+</sup>94] collaboration reported about the unexpected observation of CRs beyond the GZK cut-off. However, the

---

<sup>1</sup>When this work was finalized, the Auger collaboration reported about the first evidence of the correlation between ultra high-energy CRs and Active Galactic Nuclei [AUG07].

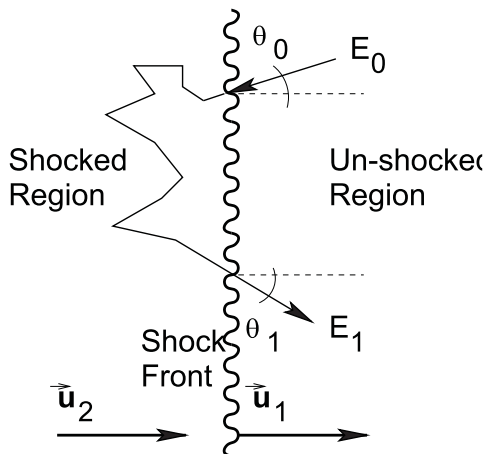


Figure 2.2: Schematic view of Fermi acceleration across a shock front in interstellar gas.

HiRes and AUGER collaborations have shown recently the drop in the CR flux spectrum around the GZK cut-off [A<sup>+</sup>, Y<sup>+</sup>].

So far, the sources of very high-energy CRs remain unknown, and some of the candidates will be discussed in the following sections. In the past years, the identification of these sources has been the main reason to investigate neutral particles like neutrinos, since their propagation in space is not affected by irregular magnetic fields in and outside the galaxy. With a neutrino telescope of sufficient sensitivity, it should be possible to detect these sources and reveal the processes responsible for the very high-energy release.

Before discussing in more detail neutrino production and physical properties, let us have a closer look at the CR production mechanism which can explain the observed spectrum of CRs for a spectral index  $\gamma \sim 2.7$ : first-order Fermi acceleration.

### Fermi acceleration

In Figure 2.2 we illustrate the so-called first-order Fermi acceleration [Fer49], considering a shock front moving in interstellar gas. The acceleration mechanism takes place due to different magnetic inhomogeneities behind and ahead the shock front. A charged particle which passes through the shock front, in fact, is repeatedly scattered between the two sides of the front by these magnetic inhomogeneities, and it gains energy for each iteration of the process. As we will see, the mean energy gain depends linearly on the shock front velocity: therefore, this process is called *first-order* Fermi acceleration.

Let us describe the process in more detail. A shock front travels with

velocity  $\vec{u}_1$ , while the shocked interstellar gas behind the front moves with velocity  $\vec{u}_2$ . A particle crosses the shock front with energy  $E_0$  and angle  $\theta_0$ . In the frame of the shocked gas the energy of the particle is:

$$E'_0 = \Gamma E_0 (1 - \beta \cos \theta_0), \quad (2.2)$$

where  $\beta = |\vec{u}_2|/c$  is the speed of the shocked gas,  $c$  is the speed of light in vacuum and  $\Gamma = (1 - \beta^2)^{-1/2}$ . Magnetic fields in the shocked region produce elastic scattering of the particle, which bounces back with energy  $E'_1 = E'_0$  and angle  $\theta'_1$ . The energy in the original coordinate system when the particle crosses the shock front back is:

$$\begin{aligned} E_1 &= \Gamma E'_1 (1 + \beta \cos \theta'_1) \\ &= \Gamma^2 E_0 \left[ 1 - \beta (\cos \theta_0 - \cos \theta'_1) - \beta^2 \cos \theta_0 \cos \theta'_1 \right]. \end{aligned} \quad (2.3)$$

The average energy gain for this process can be evaluated computing the average values for the cosines of the two angles,  $\langle \cos \theta_0 \rangle$  and  $\langle \cos \theta'_1 \rangle$ , assuming isotropic scattering in the rest frames of the shocked and un-shocked regions. This is a non-trivial computation, because one has to take into account the probability distribution for a particle to cross the shock front with a given angle: the result reads as  $\langle \cos \theta'_1 \rangle = -\langle \cos \theta_0 \rangle = 2/3$ . The average energy gain for one acceleration cycle follows from Eq. (2.3):

$$\langle E_1 - E_0 \rangle = \{ [1 - \beta (\langle \cos \theta_0 \rangle - \langle \cos \theta'_1 \rangle)] - 1 \} E_0 \sim \frac{4}{3} \beta E_0, \quad (2.4)$$

where we have neglected terms proportional to  $\beta^2$ . After  $n$  cycles, the particle gains energy up to  $E_0 (1 + \epsilon)^n$ , where  $\epsilon = \frac{4}{3} \beta$ . Therefore, in order to reach a given energy  $E$ , the particle has to be accelerated through a number of cycles given by:

$$n = \frac{\log(E/E_0)}{\log(1 + \epsilon)}. \quad (2.5)$$

Let us assume now that the probability for the particle to escape the acceleration region is  $P_{esc}$ ; the probability for the same particle to escape this region after  $n$  cycles, will then be  $P_{esc}(1 - P_{esc})^n$ . Using Eq. (2.5), the differential flux of the particles reads as:

$$\frac{dN}{dE} \sim (1 - P_{\text{esc}})^n = \left(\frac{E}{E_0}\right)^{\frac{\log(1-P_{\text{esc}})}{\log(1+\epsilon)}} \sim E^{-\gamma}. \quad (2.6)$$

An evaluation of  $P_{\text{esc}}$  for non-relativistic shock fronts [Gai90] gives  $\gamma = 2 + \frac{4}{M^2}$ , where  $M$  is the Mach number of the shock front. In the case  $M \gg 1$ , the spectral index is  $\gamma = 2$ .

Note, however, that the calculations presented here rely on a number of simplifications. More precise computations give a value for the spectral index at the source  $\gamma \sim 2.2$  [G<sup>+</sup>90]. It is also known that the energy-dependent leakage of CRs out of the Galaxy modifies the spectrum slope by  $\Delta\gamma \sim 0.3 - 0.6$ . Adding everything up, the first-order Fermi acceleration leads to a power law with an index  $\gamma \sim 2.7$ .

## 2.2 Neutrino Production and Physical Properties

The observed cosmic-ray energy spectrum and the known sources of non-thermal, high-energy gamma radiation can be used as a guidance for the possible neutrino source candidates. In this Section we give a short overview of the neutrino production mechanisms and we discuss the most peculiar property of neutrinos: neutrino oscillations.

### 2.2.1 Neutrino Production

For very high-energy CRs all potential sources can be divided into two classes:

- bottom-up models, which assume that CRs are accelerated up to energies of about  $10^{20}$  eV [Sig01];
- top-down models, where CRs result from the decay of very-heavy particles [Sig01, BS00].

Possible candidates for the first class are Active Galactic Nuclei and Gamma Ray Bursts; both will be described in Section 2.4. The second model class, instead, assumes the existence of yet-undiscovered heavy exotic particles with masses  $\geq 10^{21}$  eV.

Bottom-up models predict a large flux of high-energy neutrinos and gamma rays in CR acceleration processes. High-energy neutrinos are mainly produced by the decay of charged pions, generated by the interactions of accelerated protons and nuclei with target protons or photons:



$$\begin{aligned}
p + X &\rightarrow \pi^\pm + Y \\
&\hookrightarrow \mu^\pm + \nu_\mu(\bar{\nu}_\mu) \\
&\hookrightarrow e^\pm + \bar{\nu}_\mu(\nu_\mu) + \nu_e(\bar{\nu}_e), \\
p + X &\rightarrow K^\pm + Y \\
&\hookrightarrow \mu^\pm + \nu_\mu(\bar{\nu}_\mu) \\
&\hookrightarrow e^\pm + \bar{\nu}_\mu(\nu_\mu) + \nu_e(\bar{\nu}_e), \\
p + \gamma &\rightarrow \pi^+ + n \\
&\hookrightarrow \mu^+ + \nu_\mu \\
&\hookrightarrow e^+ + \bar{\nu}_\mu + \nu_e.
\end{aligned} \tag{2.7}$$

Gamma rays are decay products of neutral pions in the same primary interaction, for example:

$$\begin{aligned}
p + X &\rightarrow \pi^0 + Y \\
&\hookrightarrow 2\gamma.
\end{aligned} \tag{2.8}$$

Charged CRs are affected by intergalactic magnetic fields and gamma rays by dust layers and infrared light. Neutrinos, instead, can propagate through the space with almost no interaction. This makes neutrinos promising candidates to reveal the direction of the emitting source. However, the detection of neutrinos is not a trivial task because they are just weakly interacting.

An important remark concerns Eq. (2.7): the decay of mesons and muons is such that electron and muon neutrinos carry almost the same energy and their flux follows closely the CR spectrum. Moreover, from the reactions outlined in Eq. (2.7), we expect the neutrino flux ratios to be  $\phi_{\nu_e}^s : \phi_{\nu_\mu}^s : \phi_{\nu_\tau}^s \sim 1 : 2 : 0$  at the production source. However, as it will be shown now, neutrinos arrive at the detector side with an equal ratio for all neutrino flavors due to neutrino mixing.

## 2.2.2 Neutrino Oscillations

Without enough knowledge about the properties of the source, one cannot reliably estimate the absolute neutrino flux. However, the prediction for the ratio expectation can be made with a rather high precision.

On the way from the production source to the Earth, neutrinos undergo oscillations [Pon]. This was a popular topic for discussion since the middle of the last century, and later it was proved and established by the observation of the Super Kamiokande [F<sup>+</sup>98] and SNO [A<sup>+</sup>02] experiments.

The first condition for the theoretical explanation of the neutrino oscillation process is that neutrinos have a mass. Indeed, as it is described in [S<sup>+</sup>06, M<sup>+</sup>06], the current limit for the masses of the three neutrino flavors

is:

$$\sum_l m_{\nu_l} < 1.2 \text{ eV}. \quad (2.9)$$

The second condition is that the flavor eigenstates  $|\nu_\alpha\rangle$  of the neutrinos are not their mass eigenstates  $|\nu_i\rangle$ , but the following superpositions:

$$|\nu_\alpha\rangle = \sum_{i=1}^3 U_{\alpha i}^* |\nu_i\rangle, \quad (2.10)$$

where latin letters,  $i = (1, 2, 3)$ , denote mass eigenstates, and greek ones,  $\alpha = (e, \mu, \tau)$ , flavor eigenstates. In addition,  $U$  is the unitary Maki-Nakagawa-Sakata (MNS) matrix:

$$U_{MNS} = \begin{pmatrix} U_{e1} & U_{e2} & U_{e3} \\ U_{\mu1} & U_{\mu2} & U_{\mu3} \\ U_{\tau1} & U_{\tau2} & U_{\tau3} \end{pmatrix}, \quad (2.11)$$

which plays a similar role as that of the Cabibbo-Kobayashi-Maskawa matrix for the quark sector of the Standard Model.

In order to study neutrino-flavor mixing, or *neutrino oscillations*, we start with the temporal evolution of a given mass eigenstate, described by the solution of the Schrödinger equation:

$$|\nu_j(L)\rangle = e^{-i(E_j t - p_j L)} |\nu_j\rangle, \quad (2.12)$$

where  $E_j$  and  $p_j$  are the energy and momentum of  $|\nu_j\rangle$  in the laboratory frame, and  $t$  and  $L$  give the time and space coordinates. Being neutrinos extremely relativistic, we can set  $t \sim L$ ; in addition, since their masses are very small, we can approximate the energy-momentum relation  $E_j = (p_j^2 + m_j^2)^{1/2}$  writing  $E_j \sim p_j + (m_j^2)/(2E_j)$ . Eq. (2.12) becomes then:

$$|\nu_j(L)\rangle = e^{-i \frac{m_j^2}{2E_j} L} |\nu_j\rangle. \quad (2.13)$$

The time evolution of a flavor eigenstate follows from Eq. (2.10) and Eq. (2.13):

$$|\nu_\alpha(L)\rangle = \sum_j U_{\alpha j}^* |\nu_j(L)\rangle \sim \sum_j U_{\alpha j}^* e^{-i \frac{m_j^2}{2E} L} |\nu_j\rangle, \quad (2.14)$$

where  $E$  is the average energy over the various mass eigenstates. Using the unitarity of the MNS matrix to invert Eq. (2.10), it follows that, after a distance  $L$ , a neutrino born as  $|\nu_\alpha\rangle$  turns into the superposition of *all* flavor eigenstates:

$$|\nu_\alpha(L)\rangle \sim \sum_\beta \sum_j U_{\alpha j}^* e^{-i \frac{m_j^2}{2E} L} U_{\beta j} |\nu_\beta\rangle. \quad (2.15)$$

The probability for a neutrino of flavor  $\alpha$  to oscillate into a flavor  $\gamma$  at a distance  $L$  follows from a bit of algebra and reads as:

$$P_{\alpha \rightarrow \gamma} = \delta_{\alpha\gamma} - 2 \sum_{i \neq j} \operatorname{Re} \left( U_{\alpha i}^* U_{\gamma i} U_{\alpha j} U_{\gamma j}^* \right) \sin^2 \left( \frac{\Delta m_{ij}^2}{4 E} L \right) + \sum_{i \neq j} \operatorname{Im} \left( U_{\alpha i}^* U_{\gamma i} U_{\alpha j} U_{\gamma j}^* \right) \sin \left( \frac{\Delta m_{ij}^2}{2 E} L \right), \quad (2.16)$$

where  $\Delta m_{ij}^2 = m_i^2 - m_j^2$  is the difference between two mass eigenstates.

Assuming oscillations between just two flavors,  $P_{\alpha \rightarrow \gamma}$  is a periodic function with a period fixed by the oscillation length  $\hat{L}$ , whose value in meters reads as:

$$\hat{L} = 4 \pi \frac{E}{\Delta m_{ij}^2} = 2.48 \left( \frac{E}{\Delta m_{ij}^2} \right) [\text{m}]. \quad (2.17)$$

Here we have inserted units of  $h$  and  $c$  and we are assuming that  $E$  is given in MeV and  $\Delta m_{ij}^2$  in  $\text{eV}^2$ .

This analysis is important in order to understand the effect of neutrino propagation from distant ( $>100$  kPc) sources to the detector. The oscillation length, in fact, turns out to be very short compared to astronomical distances even for the highest-energy neutrinos. Therefore, for cosmic neutrinos, one can assume an ideal infinite number of oscillations and evaluate  $P_{\alpha \rightarrow \gamma}$  at the detector side averaging over all possible values assumed during one oscillation length. One obtains:

$$\langle P_{\alpha \rightarrow \gamma} \rangle = \sum_i |U_{\gamma i}|^2 |U_{\alpha i}|^2. \quad (2.18)$$

In this case the observable flux of neutrinos of flavor  $\gamma$ , with a flux  $\phi_{\nu_\gamma}^s$  at the source, is:

$$\phi_{\nu_\gamma} = \sum_\alpha \sum_i |U_{\gamma i}|^2 |U_{\alpha i}|^2 \phi_{\nu_\alpha}^s. \quad (2.19)$$

Therefore, in order to estimate the neutrino flux at the site of the detector, the MNS matrix elements have to be calculated. Using the atmospheric neutrino data [F<sup>+</sup>98] and the results of the CHOOZ experiment [A<sup>+</sup>99], in [AJY00] it was shown that the neutrino flux ratio at the source  $\phi_{\nu_e}^s : \phi_{\nu_\mu}^s : \phi_{\nu_\tau}^s \sim 1 : 2 : 0$  propagates to the flux ratio  $\phi_{\nu_e} : \phi_{\nu_\mu} : \phi_{\nu_\tau} \sim 1 : 1 : 1$  at the detector site. In other words, due to the neutrino oscillation, the probability of neutrino observation becomes comparable for all flavors.

## 2.3 Gamma-Ray Astronomy

Gamma-ray astronomy is tightly related to neutrino astrophysics, since both neutrinos and gamma rays are expected to be produced by hadronic accel-

eration. As shown in Eqs. (2.7) and (2.8), in fact, the results of proton or heavy-nuclei acceleration in astronomical sources are cosmic rays, gamma rays and neutrinos. In addition to the process mentioned in Eq. (2.8), high-energy gamma rays can also be produced by the acceleration of electrons which radiate photons via synchrotron radiation or inverse Compton scattering [Bed98].

From the experimentalist's point of view, gamma-ray and neutrino detection has an essential advantage respect to cosmic-ray one: being both neutral particles, photons and neutrinos are not sensible to galactic and intergalactic magnetic fields, and they can reveal the location of extragalactic sources.

In recent years, gamma-ray astrophysics has been quite successful: the current catalog of gamma-ray point sources with energies above 100 GeV contains 56 sources within our galaxy and 19 sources of extragalactic origin. These sources have been identified with high-energy gamma-ray Cherenkov telescopes, as HESS [A<sup>+</sup>07a] and MAGIC [L<sup>+</sup>04]. In spite of this, it is still unrevealed whether the observed fluxes are due to electron or proton acceleration.

The capabilities of gamma-ray detection in the very high-energy range are limited due to the interaction of gamma rays with star-light and interstellar material. In Figure 2.3, the available and unavailable energy regions for gamma-ray astronomy as functions of the redshift are shown, together with a list of the main processes responsible for gamma-ray attenuation.

Neutrinos, instead, are weakly-interacting particles, and propagate from the source to the observer without interaction. Therefore, they can be used as messengers to reveal the high-energy region, related to the most distant sources (the shadowed region in Figure 2.3); this fact makes high-energy neutrino astronomy extremely important.

## 2.4 Possible Sources of High-Energy Neutrinos

In this Section we discuss possible galactic and extragalactic sources responsible for high-energy neutrino production. We show the most prominent candidates of the bottom-up scenario and give an overview of the exotic particles predicted by top-down models. Moreover, we outline the role played by atmospheric neutrinos.

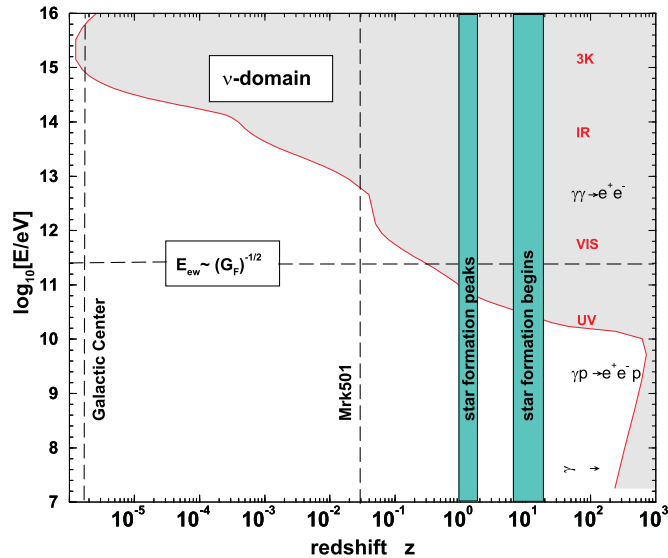


Figure 2.3: The gamma-ray energy as a function of the redshift, with a list of the dominant processes responsible for attenuation. Figure adapted from [LM00].

## 2.4.1 Active Galactic Nuclei

Being one of the brightest gamma-ray sources in the Universe, Active Galactic Nuclei (AGN) are considered to be the best candidate class among possible high-energy neutrino emitters. Although AGN are extremely compact objects, their energy emission is comparable to that of an entire galaxy. Their luminosities have been observed to flare by more than one order of magnitude within an hour [Wee00, HSFP99]. Furthermore, the emission spectrum of AGN ranges over the full electromagnetic spectrum, from radio wavelengths to TeV gamma rays.

The schematic illustration of the standard AGN model is shown in Figure 2.4. In this context, the core of an AGN is a supermassive black hole, with a mass  $\sim 10^8 M_{\odot}$ , located in the center of a galaxy and surrounded by an accretion disk of radius  $\sim 3$  pc. The accretion disk dumps matter into the black hole and, as the material spirals in, relativistic jets of heated matter are ejected perpendicularly to the disk. In addition, in the plane of the accretion disk, a concentric toroidal gas cloud feeds the accretion disk itself [Ree84]. In the AGN model, the highest-energy neutrinos and gamma rays are expected to be ejected along the jet.

There are several classes of recently-discovered galactic objects which are unified to construct the single AGN model. They can be distinguished by

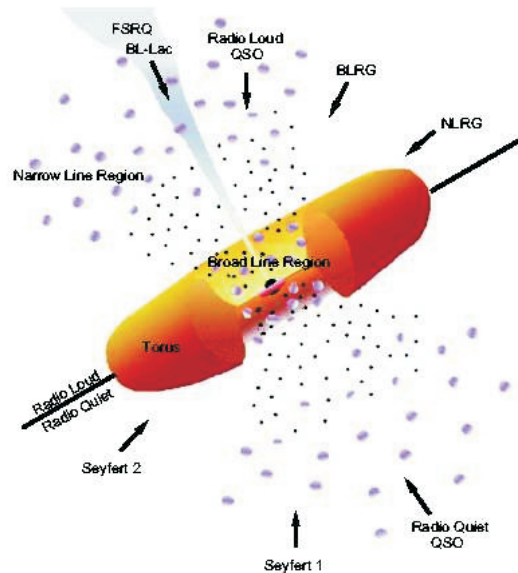


Figure 2.4: Schematic view of the unification model for AGN. According to the different viewing angle, different morphologies are observed. Picture adapted from [Thu03].

their radio flux, the observation angle and the intrinsic source luminosity. An overview of all these classes can be found in [A<sup>+</sup>06a]. The mapping of various AGN classes, according to different observation angles, is illustrated in Figure 2.4. Starting from the viewing point perpendicular to the jet we see: Narrow Line Radio Galaxies (NLRG), Broad Line Radio Galaxies (BLRG), Steep Spectrum Radio Quasars and, looking straight into the jet, BL Lac objects and Flat Spectrum Radio Quasars (FSRQ).

AGN with jets pointing towards the Earth are called *Blazars*. Examples of the closest Blazars with a large boost factor are the Markarian 421 and Markarian 501 (Mrk421 and Mrk501). For these objects, a gamma-ray signal up to energies of 20 TeV has been observed [Q<sup>+</sup>96, K<sup>+</sup>01, A<sup>+</sup>01b].

There are two classes of models available at the moment to explain the observed AGN spectra, known as leptonic [G<sup>+</sup>98] and hadronic [MPE<sup>+</sup>03] acceleration models. In the leptonic models, low-energy synchrotron radiation from electrons is up-scattered to the TeV energy region by inverse Compton scattering of relativistic electrons on abundant photons. Hadronic models, instead, assume that hadrons are accelerated to high energies in the jet and subsequently interact producing  $\pi^0$  mesons. Finally,  $\pi^0$  mesons decay into two photons, which contribute to the observed flux.

It is still an open question whether both hadronic and leptonic processes

take place in AGN gamma-ray production. On the one hand, leptonic models explain well the high-energy component of the electromagnetic AGN spectra. However, they fail to explain the origin of the cosmic-ray spectrum. On the other hand, pure hadronic models do not explain the time correlations between multi-wavelength observations of TeV Blazars [S<sup>+</sup>]. A combined model [MPE<sup>+</sup>03], which includes a mixture of proton radiation and photopion production, fits well to the electromagnetic radiation spectrum of many AGN.

## 2.4.2 Gamma Ray Bursts

Gamma Ray Bursts (GRBs) are the most luminous sources of light known in the universe, and they appear approximately twice per day. They emit gamma rays during a very-short time window, which is typically of about  $10^{-3}$ -10 seconds. The fact that GRBs are randomly distributed on the sky suggests that they have an extragalactic origin [B<sup>+</sup>96]. These objects emit also at lower frequencies, as proven by observations of afterglows [N<sup>+</sup>07].

The most favorable models for a GRB involve a relativistically-expanding fireball, which can be produced by the explosion of a hypernova or the merging of two neutron stars. Ultra-relativistic electrons and protons are then accelerated in the relativistically-expanding fireball itself [MR93].

In this scenario, neutrinos will be produced via the interaction of accelerated protons with the intense radiation field of the burst, as described in Eq. (2.7). Assuming a relativistic-fireball model, the neutrino flux can be calculated as a function of the ratio of protons and electrons in the fireball. The flux spectrum for neutrinos produced in GRBs is described in the model of [WB97] by two power laws:

$$\frac{d\phi}{dE_\nu} = \begin{cases} \frac{A}{E_B E_\nu}, & \text{for } E_\nu \leq E_B \\ \frac{A}{E_\nu^2}, & \text{for } E_\nu \geq E_B, \end{cases} \quad (2.20)$$

where  $E_B$  is the break energy, which depends on the  $\Gamma$  factor of the expanding fireball. Here  $\Gamma = (1 - \beta^2)^{-1/2}$ , where  $\beta$  is the velocity of the relativistic object. Assuming that all high-energy cosmic rays are produced by GRBs, also the normalization constant  $A$  can be constrained. The fireball's  $\Gamma$  factor was determined to be in the range  $10^2 - 10^3$  by afterglow observations [B<sup>+</sup>99, N<sup>+</sup>07].

The estimation of the neutrino rate from GRBs performed in [WB97] concluded that it can be detected by a neutrino telescope of  $1 \text{ km}^3$  size like IceCube.

### 2.4.3 Supernova Remnants

A Supernova Remnant (SNR) is a compact spinning neutron star or a black hole with an expanding shock wave which remained after the supernova explosion of a massive star. When a star collapses, most of the gravitational energy is emitted as neutrinos in the MeV range. The observations of radio and hard X-ray wavelengths from SNRs indicate that relativistic electrons are accelerated in shock fronts.

A rotating neutron star, with a pulsed radio emission, is called *Pulsar*. A constant outflow of particles from the Pulsar surface, along the magnetic-field lines of the Pulsar's magnetosphere, creates the Pulsar wind nebula. There are many pulsars known in the galaxy with different rotation periods ranging from 1 ms to 10 s. The period depends on the age of the object, since it continuously loses energy through magnetic dipole radiation. The detection of high-energy gamma rays up to TeV energies from Pulsars and their nebulas was reported in [H<sup>+</sup>99, A<sup>+</sup>05d]. The most famous of the observed objects is the *Crab* nebula which has an intense and constant flux of photons and is used in gamma-ray astronomy as a calibration source.

In [GA03], the neutrino rates are estimated from the Crab nebula and other similar sources, assuming a hadronic model for the origin of gamma rays. A neutrino telescope of 1 km<sup>3</sup> size, like IceCube, could detect them.

### 2.4.4 Exotic Neutrino Sources

Several models belonging to the top-down scenario assume the existence of very-massive particles which are predicted beyond the Standard Model of particle physics. These particles represent candidates for a non-luminous material, Dark Matter, which is believed to compose about 90% of the mass of our universe.

One example is the class of Weakly-Interacting Massive Particles (WIMPs), proposed by super-symmetric theories. One of the WIMP dark matter candidates is the lightest stable super-symmetric particle, the neutralino. WIMPs may accumulate in the center of massive astronomical objects, like the Earth or the Sun, trapped by gravitational forces. The decay products of the WIMP annihilation, quarks or heavy leptons, would then produce neutrinos. Since the expected neutralino mass is below 1 TeV [JKG96], the energy range of neutrinos from neutralino annihilation must be relatively low compared to the energies of neutrinos produced by proton acceleration in astronomical objects.

Low-energy analysis were performed using the AMANDA data in [B<sup>+</sup>00, Olb03, Dav07], where the limits on the neutrino flux from WIMP annihilation



were settled.

## 2.4.5 Atmospheric Neutrinos and Muons

The main goal of neutrino telescopes is the detection of neutrinos from galactic and extragalactic sources. However, so far only *atmospheric* neutrinos have been detected. They come mainly from pion decay, where the pions are produced in the interaction of cosmic rays with molecules in the Earth's atmosphere.

Air showers produced by cosmic rays contain two types of particles which can be detected by underground and underwater neutrino telescopes: atmospheric muons and neutrinos. Atmospheric neutrinos are produced similarly to the scenario described in Eq. (2.7), through the decay of mesons and muons. The main difference respect to the production within an astronomical object environment is that the Earth's atmosphere is much denser.

Both pion and kaon decays are important sources for muon neutrinos, while electron neutrinos are produced mainly through  $K^\pm$  and  $K_L^0$  decays. Above  $\sim 100$  GeV, the interaction length of pions and kaons in the atmosphere is shorter than their decay length. This leads to the falling of the energy spectrum of the emerging neutrinos as  $dN/dE \sim E^{-3.7}$ . For energies below few GeV the fraction  $\phi_{\nu_\mu}/\phi_{\nu_e}$  is about 2:1, as predicted by Eq. (2.7); however, at  $\sim 1$  TeV the  $\phi_{\nu_\mu}/\phi_{\nu_e}$  ratio is already 10:1 due to the fact that electron neutrinos are nearly-exclusively produced through the decay of  $K_L^0$  mesons.

In addition, the spectrum of atmospheric neutrinos depends on the zenith angle. For high-energy muons the vertical path length through the atmosphere to the Earth's surface is shorter than the muon decay length. Therefore, the high-energy component of the atmospheric neutrino flux is generated primarily close to the horizon. This effect explains the high horizontal flux registered by the detector and the different rates for the vertical flux, which is several times lower [Vol80].

Atmospheric muons and neutrinos are the result of the reactions described by Eq. (2.7). Also mesons containing charm quarks, such as  $D^0$  and  $D^\pm$ , are produced in high-energy interactions in the atmosphere. The semi-leptonic decay of D mesons [Vol80] is a source of neutrinos which are usually called *prompt*, because of the short lifetime of the charmed particles. The prompt neutrino contribution to the general flux is not more than a few percent for energies around 1 TeV. However, with growing energy, their contribution becomes significant.

Figure 2.5 illustrates the flux of atmospheric muons and muon and electron neutrinos. For both spectra the conventional flux, which corresponds to

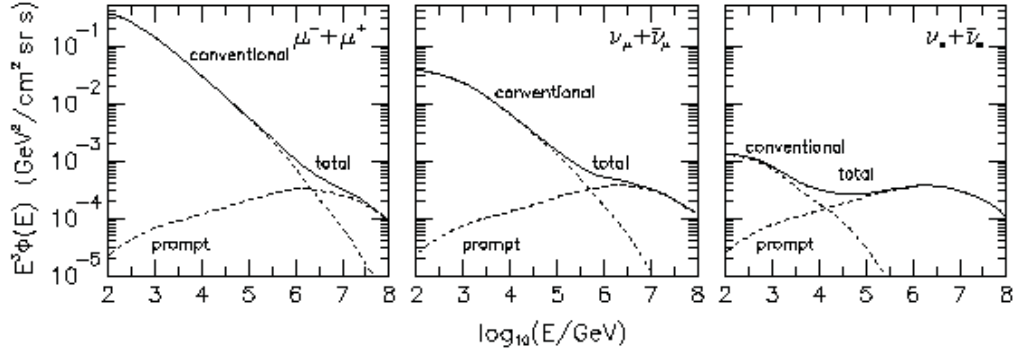


Figure 2.5: The flux for atmospheric muons and muon and electron neutrinos, weighted with  $E^3$ . The solid line corresponds to the detailed MC simulation, while the dashed ones follow from analytical calculations. This picture was adapted from [GIT96].

$\pi$  and  $K$  decays, is dominating at lower energies. The crossing energy, where prompt neutrinos become the dominant source of atmospheric neutrinos, is located at  $\sim 10$  TeV for  $\nu_e$  and at  $\sim 1$  PeV for  $\nu_\mu$ . The flux shown here for prompt neutrinos is based on perturbative Quantum Chromodynamics calculations [GIT96], and currently it represents one of the lowest flux predictions. Because of high uncertainties for the charm production cross-section, the crossing energy is not well known.

The charmed mesons responsible for the prompt flux do not reach the Earth's surface even at the highest energy. Therefore, the prompt flux is isotropic, being independent on the zenith angle. Calculations of charmed meson decays were performed by many groups and can be found in [BNSZ89, VFGS87, GIT96].

## 2.5 Diffuse High-Energy Neutrinos

Whether or not individual sources of high-energy neutrinos are intense enough to be observed, a large neutrino detector such as IceCube will be sensitive to the diffuse flux of neutrinos, looking for signals integrated over the whole sky [LM00]. The diffuse search of astrophysical neutrinos is based on the expectation for the much harder spectrum coming from the shock acceleration (see paragraph on Fermi acceleration), falling as  $d\phi/dE \propto E^{-2}$ , in contrast to the  $d\phi/dE \propto E^{-3.7}$  spectrum for atmospheric neutrinos. An excess of the signal over the expected atmospheric neutrino background would indicate

the existence of an extraterrestrial neutrino flux. Note that a diffuse analysis can be performed by reconstructing events with different topologies (track- and cascade-like, discussed in the next chapter). The work described in this thesis was done investigating cascade-like event signatures.

Presently, there is a big number of theoretical predictions for the diffuse neutrino flux from astrophysical sources. As it was shown in Section 2.3, the neutrino production mechanism must be consistent with the results of gamma-ray and cosmic-ray observations available at the moment. However, there are only some sectors of the energy range where observations of the gamma-ray flux were successfully performed. For example, the region between 30 MeV and 100 GeV was investigated by the EGRET satellite, which measured a diffuse flux [S<sup>+</sup>98]:

$$\phi^\gamma(E) = (1.37 \pm 0.06) \times 10^{-6} E^{-2.1 \pm 0.03} [\text{GeV}^{-1} \text{cm}^{-2} \text{s}^{-1} \text{sr}^{-1}]. \quad (2.21)$$

Figure 2.6 shows the spectrum for the muon neutrino flux expected from known sources and for various theoretical models. The narrow shadowed region, which has the "softest" spectrum, corresponds to the atmospheric neutrino flux. The upper and lower boundaries correspond to the horizontal and vertical directions. The broad solid region, instead, shows the boundaries for the diffuse neutrino flux of our galaxy. The upper bound corresponds to the neutrino flux from the galactic center, while the lower one is related to the flux from the edges of the galactic disk [IT]. Finally, the wide horizontal band illustrates the signal produced by unresolved extragalactic sources from which gamma ray and cosmic ray nucleons freely escape (curved upper boundary), and from which only gamma rays escape (straight upper boundary) [MPR00]. The lower boundary represents a limit for cosmic-ray storage in galaxy clusters [CB98].

The various lines are related to different models:

- (1)  $pp$  interactions in the core of AGN, as proposed by Nellen et al. [NMB93];
- (2) the Stecker and Salamon [SS96] prediction for  $p\gamma$  interactions in the core of AGN;
- (3)  $p\gamma$  collisions in extragalactic photo-production sources, as suggested by Mannheim et al. [MPR00];
- (4) the Mannheim model A for  $p\gamma$  interactions in Blazar jets producing ultra-high-energy (UHE) cosmic rays through neutron escape [Man95];
- (5)  $p\gamma$  interactions due to UHE cosmic rays escaping from radio galaxies and traveling through the 2.7 K cosmic microwave background according to the model of Rachen and Biermann [Wei67, PJ96];

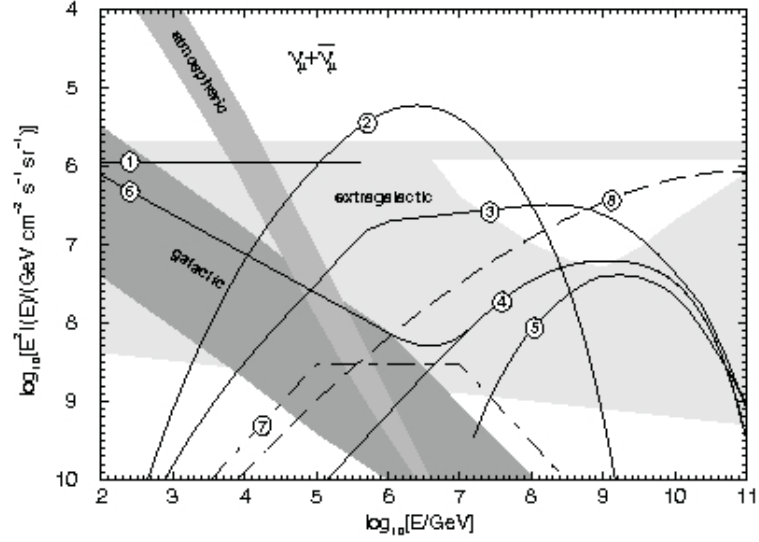


Figure 2.6: Expected  $(\nu_\mu + \bar{\nu}_\mu)$  fluxes for diffuse emission from known and expected sources. See text for details. The picture was adapted from [LM00].

- (6)  $pp$  interactions in host galaxies of Blazar jets as assumed in the model of Mannheim [Man95];
- (7) the GRB model by Waxmann and Bachall [WB97];
- (8) the Sigl et al. [Sig98] and Birkel and Sarkar [BS98] models, where neutrinos are produced in the decay of  $XY$  gauge bosons of mass  $10^{16}$  GeV, creating a topological defect.

Most of the models listed here will be probed and discussed in Chapter 9.

# Chapter 3

## High-Energy Neutrino Detection

Neutrinos are very elusive particles: being weakly interacting, they cannot be directly detected. However, their physics can be investigated through the detection of secondary particles produced by the interaction of neutrinos with molecules of dense mediums like water and ice. The potential of neutrino telescopes, in fact, relies on the possibility of detecting the Cherenkov light emitted by the products of scattering processes involving neutrinos in the initial state. Note that, according to the predictions for the flux of extragalactic neutrinos analyzed in Chapter 2, very-large detector volumes are required in order to detect a statistically-relevant neutrino flux.

In this chapter we discuss the main aspects of neutrino detection. First, in Section 3.1, we give an overview of the most-relevant neutrino scattering processes, showing the behavior of the related cross sections as a function of the neutrino energy. Next, in Section 3.2, we describe the final states of the neutrino interaction processes, which lead to two different kinds of event signatures: in Cherenkov telescopes the signatures are classified as track- or cascade-like. Since in this thesis we focus on cascade-like events, we devote Section 3.3 to discuss the mechanisms of cascade production and development in Cherenkov detectors.

### 3.1 Neutrino Interactions

In the context of the Standard Model of particle physics [Sal68, Gla61, Wei67], neutrinos interact with nucleons through  $W^\pm$ - or  $Z$ -boson exchange. These two processes are known respectively as Charged-Current (CC) and Neutral-Current (NC) interactions. The final products of these reactions are

different: in CC interactions a charged lepton is produced in association with a hadronic cascade; in NC interactions the final state is given by a neutrino of any flavor and a hadronic shower,

$$\text{CC : } \quad \nu_l + N \rightarrow l^- + X, \quad (3.1)$$

$$\text{NC : } \quad \nu_l + N \rightarrow \nu_l + X. \quad (3.2)$$

Here  $l$  represents a given lepton flavor,  $l = (e, \mu, \tau)$ ,  $\nu_l$  is the associated neutrino,  $N$  denotes a nucleon and  $X$  stands for the hadronic final state.

The differential cross section for a CC interaction with an isoscalar nucleon is given by [GQRS96]:

$$\frac{d^2\sigma_{cc}}{dx dy} = \frac{2 G_F^2 M_N E_\nu}{\pi} \left( \frac{M_W^2}{Q^2 + M_W^2} \right)^2 \left[ x q(x, Q^2) + x \bar{q}(x, Q^2) (1 - y)^2 \right]. \quad (3.3)$$

Here  $E_\nu$  is the neutrino energy in the laboratory fixed target frame,  $M_N$  and  $M_W$  are the masses of the nucleon and the  $W$  boson,  $-Q^2$  is the squared momentum transferred from the neutrino to the outgoing lepton and  $G_F = 1.16632 \times 10^{-5} \text{ GeV}^{-2}$  is the Fermi-coupling constant of weak interactions. The Bjorken scaling variables  $x$  and  $y$ ,

$$x = \frac{Q^2}{2 M_N (E_\nu - E_l)}, \quad y = 1 - \frac{E_l}{E_\nu}, \quad (3.4)$$

where  $E_l$  is the energy of the outgoing lepton, describe the fraction of the nucleon momentum carried by the reacting parton ( $x$ ), and the fraction of the neutrino energy transferred to the lepton ( $y$ ). Finally,  $q$  and  $\bar{q}$  are linear combinations of the quark and anti-quark parton density functions (PDFs) of the interacting nucleon.

For NC interactions, the differential cross section can be described by a formula which follows from Eq. (3.3) replacing  $M_W$  with  $M_Z$ , rescaling by an overall factor 1/4 and using different linear combinations of the PDFs.

In contrast to the hadronic interactions of Eq. (3.1) and Eq. (3.2), neutrino-electron scattering can generally be ignored because, being the electron mass  $m_e \ll M_N$ , the cross section is several orders of magnitude lower than the neutrino-nucleon one. However, a notable exception is represented by the so-called Glashow resonance [Gla60]:

$$\bar{\nu}_e + e^- \rightarrow W^- \rightarrow X, \quad (3.5)$$

where  $X$  is a generic final state for the  $W$ -boson decay. At  $E_\nu \sim 6.3 \text{ PeV}$  the total neutrino cross section of this process is about 300 times larger than

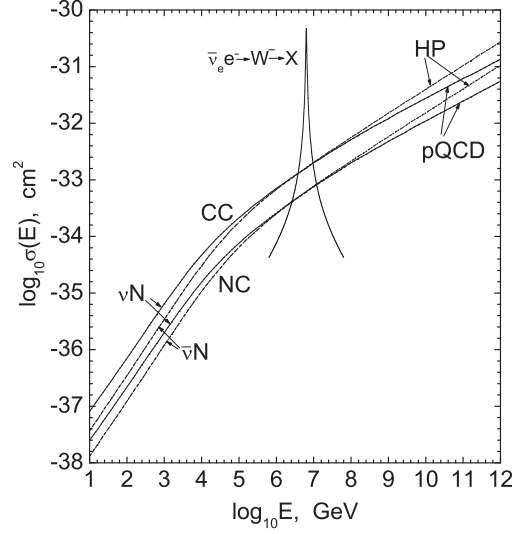


Figure 3.1: Charged-current and neutral-current neutrino cross sections. Note the Glashow-resonance peak at  $E_\nu \sim 6.3$  PeV. Figure adapted from [Kow04].

the neutrino-nucleon one. The total cross section reads as:

$$\sigma_{\bar{\nu}_e e^-} = \frac{2 G_F^2 m_e E_\nu}{(M_W^2 - 2 m_e E_\nu)^2 + \Gamma_W^2} \frac{\Gamma_{W \rightarrow X}}{\Gamma_{W \rightarrow e^- \bar{\nu}_e}}. \quad (3.6)$$

Here  $\Gamma_W$  is the total width of the  $W$  boson,  $\Gamma_W = 2.14$  GeV [Y<sup>+</sup>06],  $\Gamma_{W \rightarrow X}$  is the inclusive decay width into the final state  $X$  and  $\Gamma_{W \rightarrow e^- \bar{\nu}_e}$  is the partial decay width for the decay of the  $W$  boson into a couple  $e^- \bar{\nu}_e$ . The energy range where this process dominates over neutrino-nucleon scattering spans between 3 PeV and 10 PeV.

In Figure 3.1 the neutrino cross sections for CC and NC interactions are shown as functions of the neutrino energy. In addition, the cross-section increase due to the Glashow resonance is illustrated. At low energies, up to few TeV, where  $Q^2 \ll M_W^2 (M_Z^2)$ , the transferred momentum can be neglected and the neutrino-nucleon cross sections are proportional to the neutrino energy. When  $Q^2$  is comparable with  $M_W^2 (M_Z^2)$ , the total cross-section growth is roughly reduced to  $\sigma \sim E^{0.4}$ .

From Eq. (3.4) it follows that, for high-energy neutrinos, one needs a precise knowledge of the PDFs at very-low  $x$  values. Up to  $E_\nu \sim 1$  PeV, the PDFs have been directly measured at collider experiments [A<sup>+</sup>95, D<sup>+</sup>95]. However, since no measurements are available above this energy, predictions for the very high-energy region rely on extrapolations. Therefore, at high energies, the cross section prediction suffers from large uncertainties due to

the extrapolation of the PDFs. In Figure 3.1 two extrapolations of the PDFs are shown, obtained employing perturbative QCD (pQCD) or hard-pomeron exchange (HP).

The increase of the neutrino cross section for high energies is important for two reasons. First of all, when the cross section increases, also the probability to detect neutrinos within the detector target volume grows. This fact can also partially compensate the falling as  $d\Phi/dE \sim E^{-2}$  of the expected astronomical neutrino flux (see Figure 2.1). In addition, with the rise of the cross section, the probability for neutrinos to be absorbed in the Earth before reaching the detector volume increases as well. For instance, the attenuation length for neutrinos of about 50 TeV is equal to the Earth's diameter, and it decreases with the energy growth.

For  $\tau$  neutrinos, however, the absorption process is less relevant due to the so-called  $\tau$  regeneration effect. In a CC interaction, in fact, a  $\nu_\tau$  produces a  $\tau$  lepton which carries most of the primary neutrino energy. The  $\tau$  lepton has a short lifetime,  $\tau_\tau = (290 \pm 1.0) \times 10^{-15}$  s, and rapidly decays to a final state containing a  $\nu_\tau$ . Note that, in about 17% of cases, also electron and muon (anti-)neutrinos can be produced by the  $\tau$ -lepton decay:

$$\begin{aligned} \tau^- &\rightarrow \nu_\tau \bar{\nu}_\mu \mu^- \\ &\hookrightarrow \nu_\mu \bar{\nu}_e e^-. \end{aligned} \tag{3.7}$$

As a result, the free path of  $\nu_\tau$  increases in contrast to the cases of  $\nu_e$  and  $\nu_\mu$ . A detailed computation of the tau regeneration effect can be found in [DRS00].

## 3.2 Event Signatures and Cherenkov Radiation

As we have shown in the previous section, neutrinos can interact with nuclei through Charged-Current (CC) or Neutral-Current (NC) interactions. In this Section we discuss the possible event signatures of the interaction processes and we describe the detection principle of the AMANDA telescope: the Cherenkov technique.

### 3.2.1 Event topologies

For NC interactions, neutrinos of all flavors react in an analogous way, producing a simple hadronic cascade as shown in Figure 3.2(a). The products of CC interactions, instead, show a different behavior for each of the three lepton flavors:



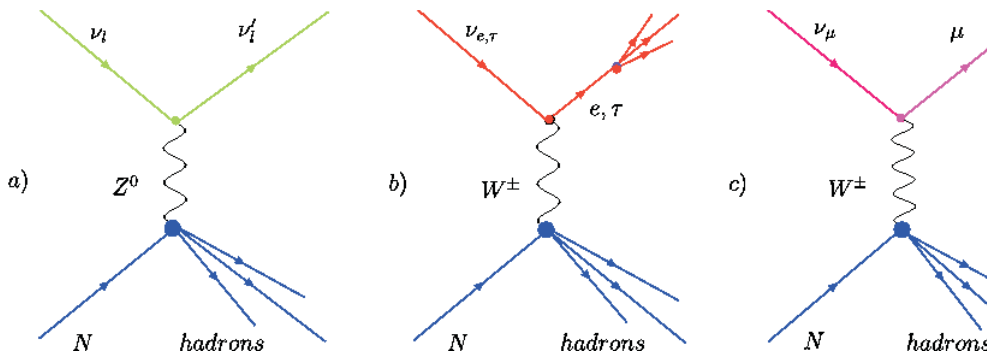


Figure 3.2: Charged-current and neutral-current interactions for neutrinos of all three flavors.

- When an electron neutrino undergoes a CC interaction, the products are an electromagnetic cascade, where the electron radiates photons, and a hadronic shower. This double-cascade production is illustrated in Figure 3.2 (b). Currently, there is no experimental apparatus available to distinguish between a hadronic and an electromagnetic shower: both of them are detected and reconstructed as cascade-like events.
- $\tau$  neutrinos, undergoing CC interactions with nuclei, lead to event topologies very similar to electron-neutrino ones. However, having a very short lifetime, the secondary  $\tau$  lepton rapidly decays, producing an additional shower. At low energies the two cascades, induced respectively by the neutrino interaction and the  $\tau$  decay, cannot be distinguished. At energies above 1 PeV, the  $\tau$ -decay length reaches about 50 m, and increases with the energy. Here the two cascades can be separated by the experimental analysis, and the resulting event signature is known as a *double-bang* event.
- Muon neutrinos produce a muon and a hadronic cascade through a CC-interaction as in Figure 3.2 (c). In this case, the resulting muon can travel for very long distances through the dense medium, in contrast to the local events originated from electron and  $\tau$  leptons. Therefore, although the interaction occurs very far from the detector, the muon track can be reconstructed and the flavor of the interacting neutrino identified by the particular *track-like* signature of the muon.

Summarizing, two event topologies for CC and NC interactions can be distinguished: a unique track-like topology produced by a muon after a CC interaction, and a cascade topology, where the cascade can be a hadronic

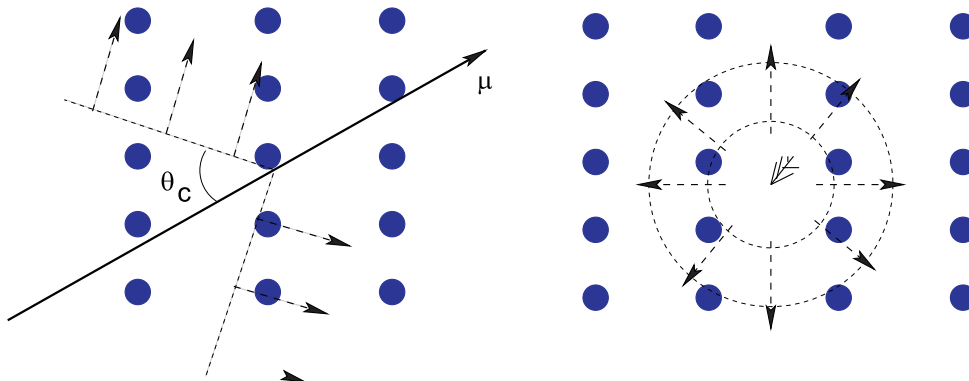


Figure 3.3: The event topologies (track- and cascade-like) for the products of neutrino interactions.

shower or an electromagnetic one. Both event signatures are illustrated in Figure 3.3: the track-like event, as it appears in the detector, is shown on the left side, and the cascade-like event topology can be found on the right.

### 3.2.2 Cherenkov radiation

The AMANDA detector is a Cherenkov neutrino telescope. The aim of the detector is to reconstruct the physical parameters of the incoming neutrinos through the Cherenkov radiation emitted by the secondary charged particles produced by the interaction of neutrinos with nuclei. This method was suggested by Markov [Mar60] in 1960.

Cherenkov radiation is emitted by charged particles traveling in dense media, like ice or water, with a velocity  $v = \beta c$ , which exceeds the velocity of light in the medium,  $v_C = c/n$ , where the refraction index is  $n \sim 1.33$ . Here  $c$  is the speed of light in vacuum and  $v_C$  is known as the Cherenkov velocity threshold for the medium. The emitted Cherenkov light is strongly peaked at an angle  $\theta_C$ :

$$\cos \theta_C = \frac{1}{\beta n(\lambda)}. \quad (3.8)$$

For water and ice at  $\beta \sim 1$  the Cherenkov angle is  $\theta_C \sim 41^\circ$ . The number of photons emitted per unit of track length  $x$  for a particle with charge  $\pm e$  and wavelength  $\lambda$  is given by the Frank-Tamm formula [Jac52]:

$$\frac{d^2 N}{dx d\lambda} = \frac{2\pi\alpha}{\lambda^2} \left[ 1 - \frac{1}{\beta^2 n^2(\lambda)} \right], \quad (3.9)$$

where  $\alpha$  is the fine structure constant.

Although the energy emitted by Cherenkov radiation is only a small part of the continuous energy loss of charged particles, Cherenkov emission is important because of the large number of photons with detectable wavelengths. For a range between  $\lambda = 300 \text{ m}$  and  $\lambda = 600 \text{ m}$ , where ice is a transparent medium and also the glass of the Optical Modules of the detector is almost transparent, one expects an emission of approximately 200 Cherenkov photons per cm.

### 3.3 Physics of Cascades

In this section we discuss the mechanism of electromagnetic- and hadronic-cascade production and development. In addition, details about the estimate of the cascade parameters inside a Cherenkov detector, like AMANDA, are presented.

#### 3.3.1 Electromagnetic Cascades

At low energies, electrons and positrons lose their energy mainly due to ionization processes. However, high-energy electrons, starting from the so-called critical energy  $E_c$ , lose energy in matter predominantly by the radiative processes of bremsstrahlung and pair production. Electrons radiate photons through bremsstrahlung; the photons, interacting with matter, produce electron-positron pairs. The iteration of the process develops an electromagnetic cascade until the energy of the secondary electrons drops below the critical energy,  $E_c$ , and a further cascade development is suppressed. The mean distance after which the energy of the electron is reduced to  $1/e$  of its initial value is known as radiation length,  $X_0$ . The radiative distance for pair production by high-energy photons is related to the radiation length for electron bremsstrahlung, and is given by  $7/9X_0$ .

A simplified model for the electromagnetic cascade development was proposed in 1952 by Bruno Rossi [Ros52], with the following restrictions:

- the incoming charged particles have an initial energy  $E_0 \gg E_c$ , where  $E_c$  is the critical energy;
- each electron with  $E_0 > E_c$  travels for one radiation length and then it transfers half of its energy to a bremsstrahlung photon;
- each photon produced with energy  $E_\gamma > E_c$  travels for one radiation length and then creates an electron-positron pair interacting with matter. Each secondary particle carries half the energy of the original photon;

- electrons with energies less than  $E_c$  cease to radiate and then lose the rest of their energy by collisions.

This simple branching model suggests that after  $n$  radiation lengths the shower will contain  $2^n$  particles, each of them with an average energy given by:

$$E(n) = \frac{E_0}{2^n}. \quad (3.10)$$

The cascade development will stop abruptly when  $E(N) = E_c$ , where  $N$  is the maximum number of radiation lengths in the shower. From Eq. (3.10) it follows that  $2^N = E_0/E_c$ . The cascade length,  $X = X_0 N$ , can be written in terms of the initial and critical energies as:

$$X = X_0 \frac{\ln(E_0/E_c)}{\ln 2}. \quad (3.11)$$

This simplified model leads to an important conclusion. As one can see from Eq. (3.11), the length of the cascade varies proportionally to the logarithm of the primary energy. This is a feature which emerges also from more sophisticated models of the process and is observed experimentally. In ice, the critical energy is  $E_c \sim 80$  MeV and the radiation length is about  $X_0 \sim 40$  cm, so the average cascade length does not exceed a few meters.

The number of photons produced by the electromagnetic cascade in ice is close to  $10^5 \gamma/\text{GeV}$ , a fact which makes such a simulation complicated, since all processes for all secondary particles have to be tracked from the initial energy to the critical energy  $E_c$ . The detailed simulation of the electromagnetic cascades has been performed in [Wie96]. In this simulation, the longitudinal energy deposition of the electromagnetic cascade is described by:

$$\frac{dE}{dn} = E_0 b \frac{(bn)^{a-1} e^{-bn}}{\Gamma(a)}. \quad (3.12)$$

Here  $n = X/X_0$  is the number of radiation lengths,  $\Gamma$  is the Euler Gamma function and  $E_0$  is the initial energy of the cascade. In [Wie96] the parameters  $a$  and  $b$  were obtained by fitting Eq. (3.12) through a simulation with GEANT 3.2.1, assuming the water as a detection medium:

$$a = 2.03 + 0.604 \ln(E_0), \quad b = 0.633, \quad (3.13)$$

where  $E_0$  is given in GeV. Taking into account these parameter values, an electromagnetic cascade of energy close to 100 TeV would reach a length of about 5 m.

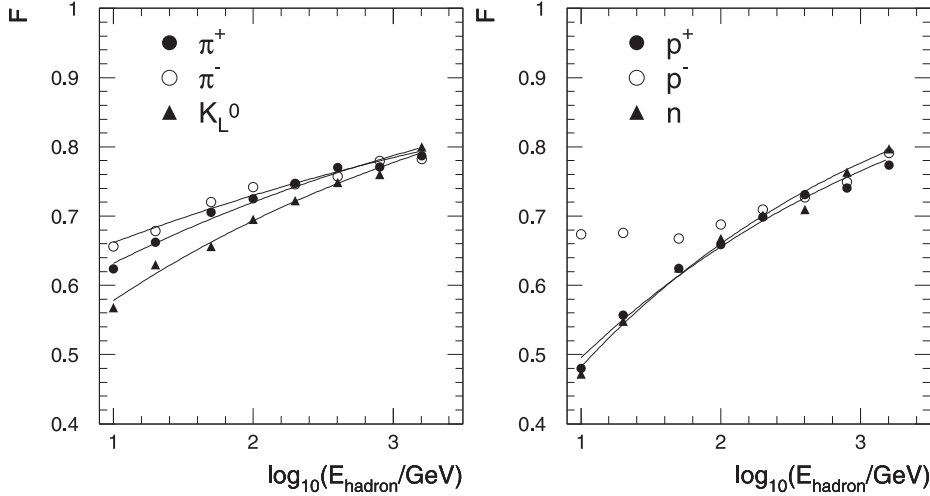


Figure 3.4: The ratio of the hadronic and the electromagnetic light output for different cascade energies and injected particles. The pictures are adapted from [Kow].

### 3.3.2 Hadronic Cascades

The simulation of hadronic cascades is more complicated than the one for electromagnetic showers. In general, the light output of a hadronic cascade is smaller than that of an electromagnetic one for two reasons. Firstly, the Cherenkov radiation threshold for hadrons is higher than the one for electrons, since this parameter depends on the particle mass [Dre02]. Secondly, a part of the cascade energy is transferred to "invisible energy", represented by low-energy neutrinos, which are produced in the shower and cannot be detected.

As we have shown in Eq. (3.11), the total track length of the electromagnetic cascade is proportional to the logarithm of the initial energy. Various processes induced by the particles in the hadronic shower cause a non-linear light output of the hadronic cascade with respect to the initial energy. Hence, a track length has as well a non-linear energy dependence. The ratio for the track lengths of hadronic,  $T_{hadron}$ , and electromagnetic,  $T_{em}$ , cascades of the same energy can be defined as [Kow]:

$$F = \frac{T_{hadron}}{T_{em}}, \quad (3.14)$$

and it is always smaller than 1. A process whose contribution becomes significant with the energy rise is  $\pi^0$  production, with the subsequent  $\pi^0$  decay into two photons; as a consequence, an electromagnetic component is added to the

hadronic cascade [G<sup>+</sup>94]. In order to calculate this contribution, a detailed simulation was performed in [Kow], where electromagnetic and hadronic cascades were simulated using the GEANT 3.4.1 program. The ratio  $F$  was obtained for energies up to 3 TeV and different types of injected particles. In Figure 3.4 the obtained values of  $F$  are shown as functions of the energy for several particles. In the Monte Carlo simulation used in this analysis, a simplified hadronic-cascade description has been used. All hadronic cascades were treated as electromagnetic cascades with a reduced light yield of 80%.

# Chapter 4

## The AMANDA Detector

The AMANDA detector aims at the detection of high-energy neutrino sources and the understanding of cosmic acceleration.

In this chapter we show the main features of the AMANDA detector. In Section 4.1 we give an overview of the various detector devices. Next, in Section 4.2, we describe the Data Acquisition System of the experiment. Section 4.3 is devoted to a recent technological improvement with respect to the AMANDA set-up, the use of the Digital Optical Modules presently implemented in the IceCube detector. Finally, in Section 4.4, we discuss the most-crucial point for the AMANDA experiment: the measurements performed in order to understand the optical properties of the Antarctic ice.

### 4.1 AMANDA Set-Up

The whole AMANDA apparatus is built in the Antarctic ice cap at the geographical South Pole, where the natural material for detection is the clear ice.

A fruitful insight on in-ice detection was gained during the first phase of the AMANDA experiment, when the AMANDA-A detector was deployed under the ice surface between depths of 800 and 1000 m, as shown in Figure 4.1. Here, the contamination of the ice with air bubbles generates multiple photon scattering, a fact which makes almost impossible to perform a good event reconstruction.

Deeper than 1500 m, instead, the air bubbles disappear under the pressure of the upper ice layers. The ice is extremely transparent and can be considered as a perfect medium for neutrino detection. This observation motivated the construction of a new detector, AMANDA-II, deployed between 1550 m and 1950 m under the ice surface. The analysis presented in this thesis relies

completely on the data collected by AMANDA-II during years from 2000 to 2004.

### Structure of the Detector

The basic building blocks of the AMANDA-II detector are the Optical Modules (OMs) with an 8-inch Photo-Multiplier Tube (PMT) enclosed in a spherical glass vessel as the main component. After an OM detects the Cherenkov light emitted by a charged particle, the PMT generates an analog signal. This is subsequently transported from the OM to the readout system through 1.5 km long electrical cables. A schematic representation of an OM is shown in Figure 4.1.

In total, there are 677 OMs assembled to 19 strings. Both strings and modules are distributed regularly and they compose a vertical cylinder with a diameter of 200 m and a height of 500 m. The deployment of the OMs has been done in several steps between the years 1995 and 2000, and the strings inside the detector cylinder are arranged in two circles. The inner circle was deployed between 1995 and 1996 and consists of 10 strings (the so-called AMANDA-B10 configuration). The outer circle is composed of 9 additional strings which were deployed between 1998 and 2000. The complete AMANDA-II 19-string detector is shown in Figure 4.1.

During the five years of deployment, the technique of PMT-signal transmission has been improved, and the various strings show different features, which concern both the electrical cables employed for signal transmission and the OMs.

- *Strings 1-4.* Here high-voltage (HV) power supply and transmission of the analog PMT signal to the surface are performed by coaxial electrical cables. These cables are affected by a high dispersion and, as a result, adjacent pulses cannot be distinguished. Single photo-electron pulses, in fact, are widened up to 200-400 ns. In this set of strings, the OMs use the *Billing* glass spheres, made of low-radioactivity glass. The dark noise rate for these OMs is very low ( $\sim 0.5$  kHz). The disadvantage of the Billing spheres is that the glass becomes opaque for wavelengths below 350 nm reducing the OM detection efficiency.
- *Strings 5-10.* Here twisted-pair electrical cables are used for power supply and signal transmission, and the dispersion for single photo-electron signal is reduced: the width of pulses is narrowed to 100-200 ns. The disadvantage of this cable type is the "cross-talk" (pick-up noise generated by induction) between cable pairs due to a non-optimal shielding: transported pulses induce fake signals in adjacent cables.



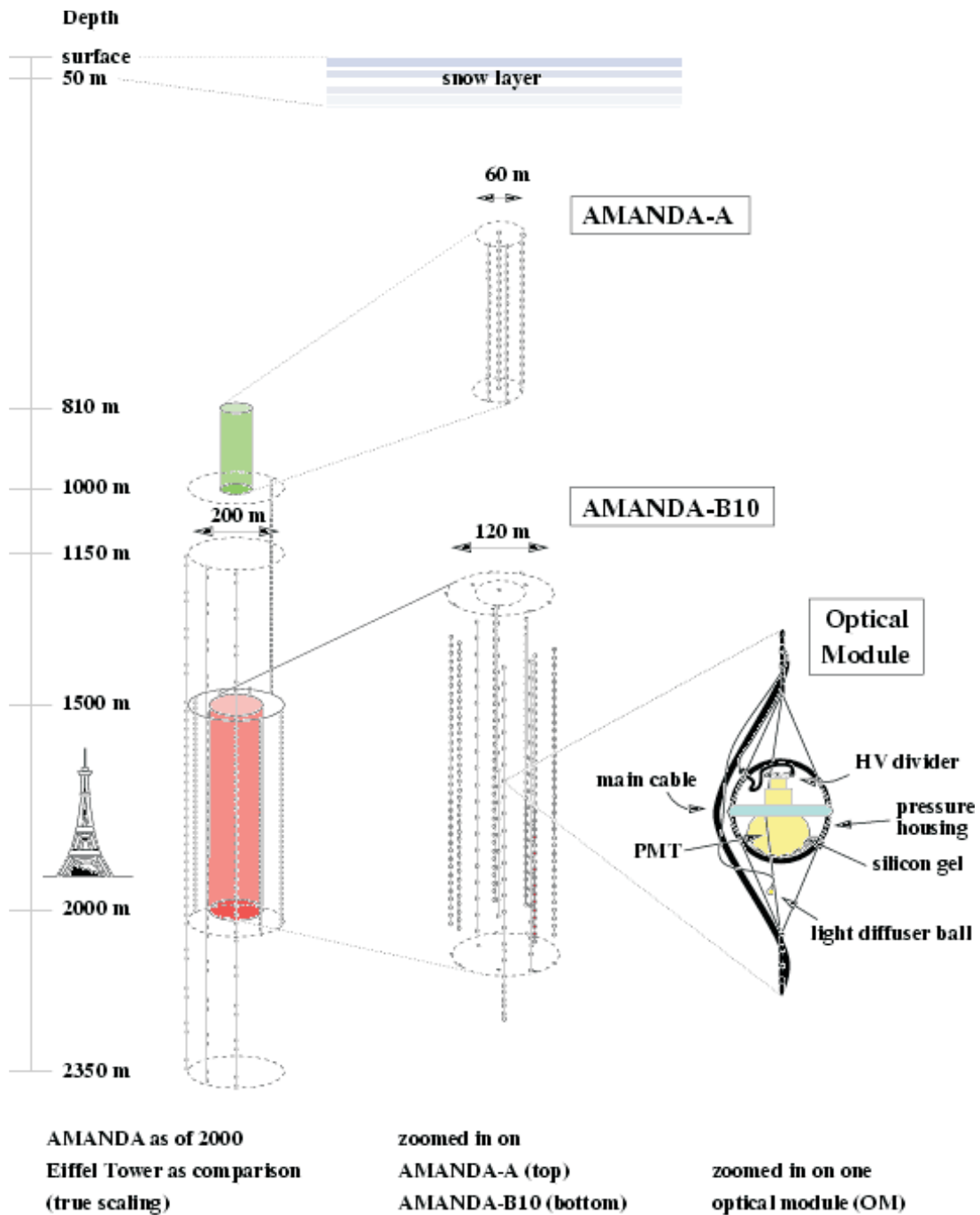


Figure 4.1: The AMANDA-A and AMANDA-II detectors. On the right, an Optical Module is shown in order to illustrate its mechanical design. The figure was adapted from [AMAA].

In this set of strings, the *Benthos* glass spheres are employed, which show an improved UV transparency respect to the Billing vessels. The quantum efficiency of the OMs built with Billing spheres, including glass and gel transmission, is about 25% less than the efficiency of the OMs made with Benthos spheres. However, the noise rate is about twice the one generated by the Billing glass vessels. Benthos glasses are employed also for the next sets of strings.

- *Strings 11-17.* In this set of strings, a Light-Emitting Diode (LED) is employed in order to convert the electrical PMT pulse into an optical one, and then *optical fibers* transport the signal to the readout system. This transition method shows a great improvement in the signal readout: the dispersion disappears and the pulse width becomes about 20 ns. However, optical fibers are more sensitive to mechanical stress effects. Therefore, they were installed together with twisted-pair electrical cables, used as a backup solution. Note that string 17 was stuck during the deployment in the ice, due to irregularities in the drilled hole, before it reached the depth of 1500 m. The HV supply for these strings, as well as for strings 1-10, is provided from the surface via electrical cables.
- *Strings 18.* Here a new technology was used for the OMs, which can be considered as the prototype for the IceCube detector modules. The first improvement is the integration of the HV generator into the OMs. The second and most-important new element is a digital readout system, implemented on the Printed Circuit Board (PCB) inside the Digital Optical Modules (DOMs) on string 18 [H<sup>+</sup>a]. DOMs perform a waveform signal digitization of the signal in order to send *binary* data to the DAQ system via electrical cables. Note that also an analog optical signal transmission is provided in addition to the digital one, as a backup solution.
- *Strings 19.* This string was equipped with Digital-Analog Optical Modules (dAOM) [Sch02] which are similar to the modules used for string 18. The difference is that dAOMs provide an analog readout, but a digital module control.

### **In-Situ Light Sources**

In order to perform detector calibration and measurements of the optical properties of the South Pole ice, a set of in-situ light sources has been deployed together with the OMs. These devices are:

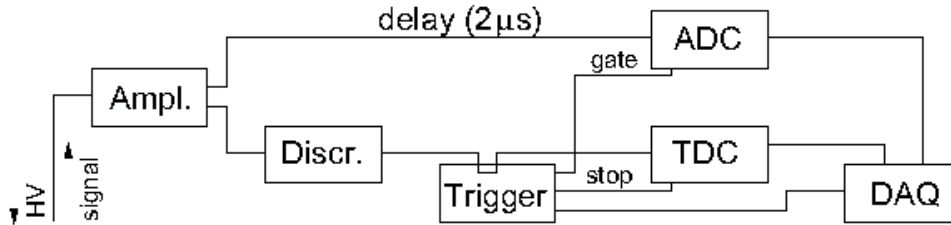


Figure 4.2: A schematic view of the AMANDA Data Acquisition System.

- flashing UV and blue LEDs, with wavelengths of 370 nm and 470 nm;
- nitrogen lasers, emitting UV radiation at 337 nm;
- a steady UV light source, emitting light at 313 nm;
- a "rainbow" module, which produces a steady monochromatic light with an adjustable wavelength between 340 nm and 560 nm.

In addition, an Yttrium Aluminium Garnet (YAG) laser was installed in the AMANDA counting house at the surface. This device emits a green light, which can be fed into the ice through optical fibers and diffuser balls. Measurements of the photon arrival times at different depths and wavelengths were performed in [A<sup>+</sup>06b] and allowed to determine the optical properties of the ice around the AMANDA detector. This step was essential for developing the simulation software which will be later discussed in Chapter 5.

## 4.2 DAQ and Trigger systems

The Data Acquisition System (DAQ) of AMANDA, located in the counting room of the Mapo building (AMANDA counting house), is schematically shown in Figure 4.2.

### DAQ System

At first, the analog PMT pulse generated by an OM passes through a signal amplifier where two signals, *prompt* and *delayed*, are produced. The time delay between the two signals is  $2\mu\text{s}$ , and different amplification gains can be chosen for the prompt and delayed signals.

The prompt signal is filtered by a discriminator, which creates a rectangular pulse whose starting and ending points (leading and trailing edges) are chosen according to a high-voltage (HV) threshold which depends on the individual parameters of each OM. Next, the discriminator output is fed into a Time-to-Digital Converter (TDC), while the copy of the signal is fed into the trigger logic. The TDC can buffer up to 16 values of the measured leading and trailing edge times and has a time resolution of about 1 ns.

The delayed signal is fed into an Analog-to-Digital-Converter (ADC). If the trigger-logic condition is satisfied, a  $10\ \mu\text{s}$  recording window for the delayed signal is opened, and the highest signal amplitude is stored. Because of the  $2\ \mu\text{s}$  delay, the amplitude is measured in the interval  $[-2\ \mu\text{s}, +8\ \mu\text{s}]$  around the trigger time.

The ADC and TDC information is collected by the DAQ computer and gets an absolute time stamp by a GPS clock. All event information is stored on disk and magnetic tapes.

### Trigger Logic

The general AMANDA trigger logic, the so-called *multiplicity* trigger, requires at least 24 pulses for an event within a time window of  $2.5\ \mu\text{s}$ .

Note that two additional triggers are implemented: the *string* trigger and the *space* trigger. The first one is set to a lower-hit multiplicity, and requires that at least 5 OMs of the same string have signal records in a given time window. The space trigger, instead, is formed by the SPACE-2 [A<sup>+</sup>04b] air-shower array on the ice surface, close to the AMANDA location, and it opens a recording window each time a shower has been recorded by the SPACE-2 array. The analysis presented in this thesis relies only on the 24-fold multiplicity trigger.

## 4.3 Digital Optical Modules for IceCube

The AMANDA Digital Optical Modules (DOMs) installed on string 18 [H<sup>+</sup>a] served as prototypes for the DOMs of the IceCube detector, which relies on a more-sophisticated technology. In this section we discuss the design, production and testing of the DOMs.

### Support Electronics

The key idea has been to equip the standard OMs with a built-in support electronics. The light detection part of an IceCube DOM is very similar to

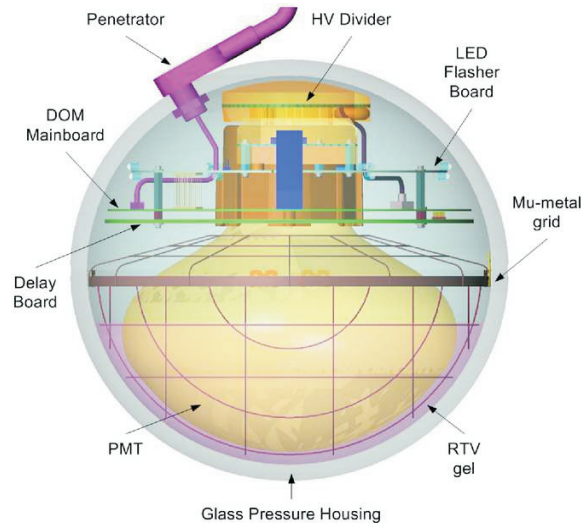


Figure 4.3: A schematic view of an IceCube Digital Optical Module.

that of an AMANDA OM, and it consists of a large-area (12 inch) photomultiplier tube (PMT) enclosed in a glass sphere filled with a transparent optical gel. Compared to the AMANDA OMs, the element of novelty is the support electronics, located around the neck of each PMT, which provides the PMT power supply and digitizes the PMT analog signal. Local digitizing of the signal allows to overcome the problems which would appear during a transmission of an analog signal over a length of some kilometers.

Figure 4.3 shows the schematic view of a DOM with all its components. Concerning the PMTs, the collaboration has chosen the Hamamatsu R7081-02 model, which shows several advantages: a low noise rate,  $< 1$  Hz, at low temperatures of about  $-40^{\circ}\text{C}$ , a high gain and a fast pulse rise-time  $\sim 4$  ns. The HV generator is mounted on top of the PMT serving as a power supply for it. It can be controlled from the surface and produces a voltage up to 2000 V. The gel used to couple the PMT to the glass vessel is a clear gel with good mechanical and optical characteristics. In addition, a magnetic metal cage is set between the glass and the PMT, in order to shield the magnetic field of the Earth, improving the photo-electron collection efficiency.

A flasher board is located below the HV base. It holds 12 bright Light Emitting Diodes (LEDs) which are currently used for calibrating the detector and studying the ice properties. Note that the light emitted by these LEDs can be registered hundreds of meters away from them.

The next layer of the DOM support electronics, below the flasher board, is the most complicated and important one. The Main Board (MB) carries all the components responsible for readout, control, processing and digitization

of the PMT pulses. Two different Analog-to-Digital Convertors are available. There are Analog Transient Waveform Digitizers (ATWDs) which convert the PMT signal into a digital one and have a very good time resolution of  $\sim 3.5$  ns. They also have a wide dynamic range since their 4 input channels are served by different gain paths. Slow pulses (wide waveforms) from distant high-energy events, spread over time scales of a few  $\mu$ s, instead, are digitized by a Fast Analog-to-Digital Convertor (FADC). In both cases, the full waveform information is stored and sent to the readout computers via 2.5 km long twisted copper cables.

### DOM Testing

After the DOM integration, each item undergoes a test cycle, performed in a Dark Freezer Laboratory (DFL), where the temperature conditions are close to the natural one. A final test before installation is then performed at the South Pole. All modules are tested at different temperatures, in a range between  $+20^\circ$  C and  $-55^\circ$  C. The basic functionalities, time resolution, optical sensitivity and the PMT linearity are thoroughly tested in order to select the DOMs appropriate for the deployment <sup>1</sup>.

The first IceCube DOMs were deployed in January 2005, and all of them showed perfect functionality. The final detector configuration assumes up to 4800 in-ice DOMs. Currently (January 2008), more than 2000 DOMs have been deployed and are operating. The remaining DOMs will be deployed during the next 3-4 years. A detailed description of DOM design, integration, testing and deployment at the South Pole can be found in [Tar05, HT06].

## 4.4 Optical Properties of the Ice

The accuracy of neutrino flux measurements performed by the AMANDA detector depends on the correct reconstruction of the optical properties of the South Pole ice, which vary significantly with the depth. The most important parameters which characterize the optical properties are:

- $\lambda_{abs}$ , the *absorption length*. It describes the fraction of light which, during propagation, is absorbed by the ice per unit length. Nowadays, the model used for the description of the absorption process in the ice is the “three-component” model, discussed in detail in [PB97]. According to this model the absorption mechanism shows different features for

---

<sup>1</sup>During the first year of the IceCube installation the author was involved in the DOM testing at DESY and at the pole.

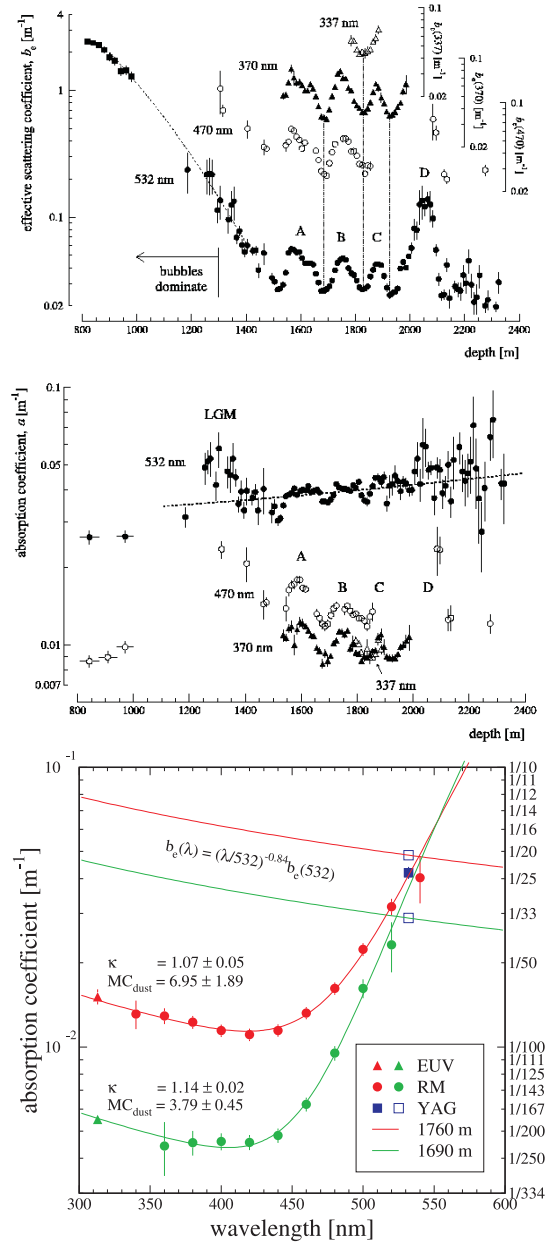


Figure 4.4: Top: the effective scattering coefficient  $1/\lambda_{\text{scat}}^{\text{eff}}$  and the absorption coefficient  $1/\lambda_{\text{abs}}$  of the ice surrounding the AMANDA detector as functions of the depth. Bottom: the wavelength dependence of  $1/\lambda_{\text{abs}}$  at two different depths within 40 m from the AMANDA-detector center. Pictures taken from [A<sup>+</sup>06b].

three regions of the wavelength spectrum. Below 200 nm, absorption increases exponentially, because the radiation is sensible to the electronic band structure of the ice crystals. Between 200 nm and 500 nm, instead, the ice can be considered to be an almost-perfect transparent medium, and absorption is an accidental phenomenon induced by the possible presence of dust molecules. Above 500 nm, finally, absorption is dominated by the presence of  $H_2O$  molecules.

- $\lambda_{scat}^{eff}$ , the *effective scattering length*, is defined in terms of  $\lambda_{scat}$ , the scattering length, and  $\cos \theta$ , the scattering angle, as:

$$\lambda_{scat}^{eff} = \frac{\lambda_{scat}}{1 - \langle \cos \theta \rangle}, \quad (4.1)$$

where  $\langle \cos \theta \rangle$  is the mean value for  $\cos \theta$ . It has been calculated in [HP98] assuming realistic impurities like acid droplets and salt crystals in the ice, and it is given by  $\langle \cos \theta \rangle = 0.94$ . The effective scattering length measures the increase of the path length covered by photons due to scattering processes, and it takes into account the strongly anisotropic angular distribution of the scattering angle. As a matter of fact,  $\lambda_{scat}^{eff}$  determines the delay of the photon arrival times with respect to the case of straight propagation.

The absorption and effective-scattering coefficients  $1/\lambda_{abs}$  and  $1/\lambda_{scat}^{eff}$  for the ice surrounding the AMANDA detector have been experimentally measured using the YAG laser described at the end of Section 4.1.

Figure 4.4 shows the observed values for  $1/\lambda_{abs}$  and  $1/\lambda_{scat}^{eff}$ . Concerning the first plot, we note that at depths between 1500 m and 2000 m, where the OMs of the detector are mainly deployed, the variation of  $1/\lambda_{scat}^{eff}$  is relatively low. In contrast, at depths above 1400 m, it increases dramatically. The peaks A,B,C and D indicate high dust concentrations at the related depths. The middle plot shows the depth profile of the absorption coefficient measured by in-situ light sources. The structure of the dust layers is also visible here, as well as an increase of the coefficient for wavelengths of more than 500 nm. The two curves in the third plot show the wavelength dependence of the absorption coefficient,  $1/\lambda_{abs}$ , as expected from the "three-component" model [PB97].

As a remark on these measurements, we note that the precision of the AMANDA in-situ instruments is of about several meters in depth. The AMANDA measurements are in very good agreement with those obtained with a new device called "dust-logger", deployed together with the first Ice-Cube modules, which has a resolution of 2-3 mm [B<sup>+</sup>05].



---

Finally, let us mention that the deployment of the AMANDA OMs, as well as the IceCube DOMs, has been performed using a hot-water drilling technique. Therefore, the ice inside the holes where the OMs are deployed is probably very different from the surrounding South Pole ice. Since the transition of air bubbles to air hydrate crystals happens on time scales which are not comparable to the the detector lifetime, photon scattering in the hole is dominated by bubbles, leading to an effective scattering length of about 1 meter. However, since the diameter of the holes (about 60 cm) is smaller than the average distance of the photon propagation from the emission point to the OM, the effects of this scattering process are not dramatically large. So far it was not taken into account, but later on it will be implemented in the simulation program.



# Chapter 5

## Data Samples

In order to understand the operations of any detector, experimental data have to be compared with theoretical expectations. The simulations shown in this work were performed using Monte Carlo (MC) techniques, based on large-statistic generation of neutrino signal and atmospheric muon background events. An overview of the simulation chain is presented in Figure 5.1.

After showing the experimental data sample in Section 5.1, we devote Section 5.2 to present the signal simulation procedure. Next, in Section 5.3, we discuss the background simulation. Finally, in Section 5.4, we describe the simulation of the AMANDA detector response.

### 5.1 Experimental Data

The experimental data used for the analysis performed in this thesis were collected by the AMANDA detector between the years 2000 and 2004. For each year, the data were taken during the austral winter, from February until November. The data sample was reduced due to short runs: all runs containing less than 6 files were removed from the sample. In addition, the periods when the detector was not running in a stable way were excluded from the analysis. As a result, the total number of triggered events between 2000 and 2004 is  $8.9 \cdot 10^9$  and the effective life-time of the detector is 1001 days. The list of runs employed for the analysis shown in this work, the detector effective lifetime and the number of triggered events are shown on a year-by-year basis in Table 5.1. The selection of runs was performed on the basis of the AMANDA monitoring data [AMAb].

Year	Runs	Lifetime (days)	Triggered Events
2000	47 - 309	197	$1.37 \times 10^9$
2001	44 - 293	193	$2.00 \times 10^9$
2002	43 - 323	204	$1.91 \times 10^9$
2003	43 - 315	213	$1.86 \times 10^9$
2004	43 - 311	194	$1.72 \times 10^9$

Table 5.1: Run periods, effective detector up-time and number of triggered events used for the multi-year (2000-2004) cascade search performed in this work.

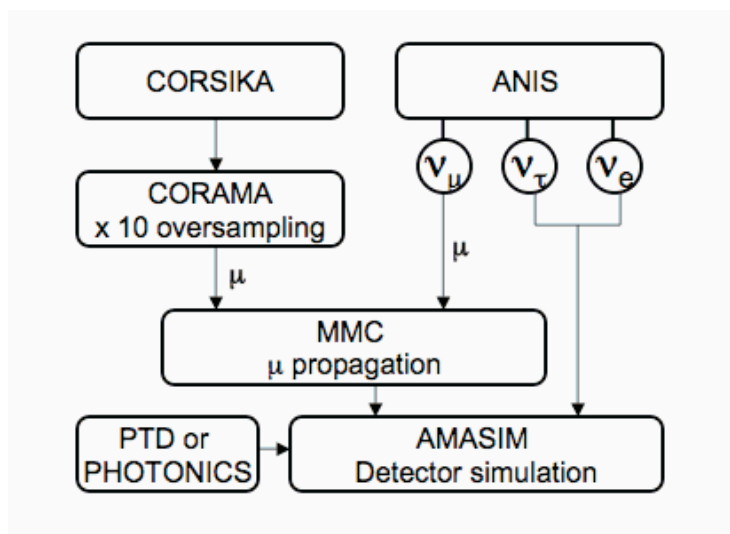


Figure 5.1: A schematic overview of the Monte Carlo simulation chain employed for our analysis.

## 5.2 Signal Event Simulation

For the analysis described in this thesis,  $5 \cdot 10^7$  neutrino signal events were generated for each neutrino flavor. In addition, a large statistics of atmospheric muon background has been simulated. All software programs and settings used for these simulations are described in this section.

### ANIS

In order to simulate neutrino events of all flavors, we used the ANIS (All Neutrino Interaction Simulation) program [GK05]. All possible neutrino interactions, charged-current and neutral-current processes, as well as resonant  $\bar{\nu}_e e^-$  scattering, have been simulated. Note that the related cross-section

data are implemented in ANIS using the CTEQ5 structure functions [L<sup>+</sup>00] as described in [GK05].

Here we give an overview of the program flow of ANIS. At first, primary neutrinos are randomly generated on the surface of the Earth with a  $d\Phi/dE \sim E^{-1}$  energy spectrum. Then, they are propagated to the specified interaction volume around the detector [GK05], taking into account possible absorption and energy-loss effects induced respectively by charged-current and neutral-current interaction processes. Besides absorption and energy loss, ANIS handles also the so-called  $\nu_\tau$ -regeneration effect. As shown in Chapter 3, a  $\tau$  lepton is produced in a charged-current interaction of a  $\tau$  neutrino within the propagation medium. Next, due to its short life-time, the  $\tau$  lepton decays producing a secondary  $\nu_\tau$  and, in about 17% of cases, a secondary  $\nu_\mu$  or  $\nu_e$ . The  $\tau$ -lepton decay is simulated by ANIS using the TAUOLA [JWDK93] program. Note also that the density profile of the Earth used for particle propagation is chosen in ANIS according to the so-called Preliminary Earth Model [DA81].

Once the neutrino has reached the interaction volume of the detector, the final vertex is sampled along the neutrino trajectory within the detection volume. For this analysis the interaction volume was defined as a cylinder with a radius of 300 m and a height spanning  $\pm 300$  m from the detector center. Neutrinos of all flavors have been simulated in an energy range from  $10^2$  GeV to  $10^8$  GeV.

### Event Weighting

After all events have been generated with a  $d\Phi/dE \sim E^{-1}$  spectrum, and with vertex positions equally distributed over the interaction volume, they are re-weighted in order to obtain two distributions: one for extra-galactic neutrino signal events and a second one for atmospheric neutrino background events. The individual weights are obtained from the following variables, which are stored in addition to every simulated event:

- *Flux weight*: this factor performs the normalization of the number of generated events to simulated fluxes. In the case of hypothetical signal simulation, the flux weight was chosen according to the model prediction. The weighting function for atmospheric neutrinos was defined assuming an  $E^{-3.7}$  spectrum according to the model of Lipari [Lip93].
- *Interaction weight*: this factor reflects the probability for each interaction to happen within the detection volume. It depends on the neutrino type, the neutrino energy, the declination of the interacting particle and the density of the target.

## 5.3 Atmospheric Muon Background Simulation

The main background source for the AMANDA experiment is represented by atmospheric muons. Muons are produced when primary cosmic rays (protons or heavier nuclei) interact with molecules of the Earth's atmosphere producing pions and kaons, which subsequently decay to muons, as shown in Eq. (2.7). Typically, neutrino telescopes are built as deep as possible in the detection medium to reduce the probability for atmospheric muons to reach the detector. Nevertheless, the rate of atmospheric muons is several orders of magnitude larger than any signal expectation: the AMANDA detector records every year around  $10^9$  atmospheric muon events, while the registered rate for atmospheric muon neutrino events is close to 300 events.

### CORSIKA

We used the CORSIKA air shower generator [HST<sup>+</sup>] to simulate muon background events. CORSIKA can simulate air showers from primary cosmic rays up to  $10^{20}$  eV. The model used for hadronic interactions is SYBILL 2.1 [EGSL99].

The generated events were distributed over a large surface area using CORAMA [Ste]. In order to increase the simulation speed, each generated event was over-sampled. Each primary particle was used 10 times, thereby randomly shifting the space coordinate and the azimuthal angle of every resulting shower.

### Muon Propagation

Relativistic muons, propagating through matter, lose energy through several processes: ionization, bremsstrahlung, photo-nuclear interaction or pair production. Although some of the energy-loss processes have a discrete nature, the number of such events increases very fast with the energy. Therefore, one can treat such processes as a continuous energy loss. This approximation was used in the MMC [CR] program, which simulates the propagation of the muons through the material. All energy losses producing secondary particles below  $0.5$  GeV were treated as a continuous muon energy loss. Only secondary particles with an energy threshold larger than  $0.5$  GeV were stored for the analysis.

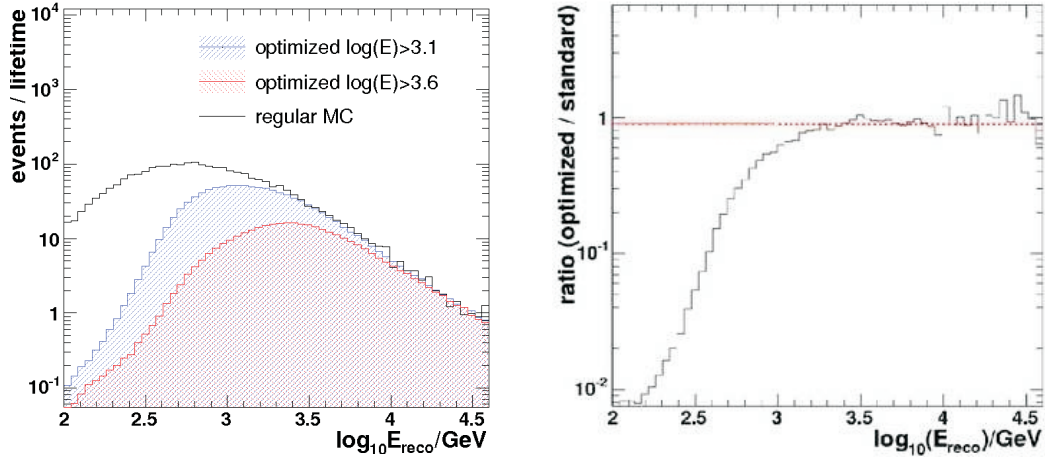


Figure 5.2: Left: Reconstructed cascade energy for various background Monte Carlo samples. Right: Ratio between the reconstructed energy distribution of the background sample optimized for medium energies and the MC sample simulated using standard settings. All events shown here have passed the vertex likelihood cut  $L_{vertex} < 7.1$  (see Chapter 6).

### Optimization of the Atmospheric Muon Simulation

The simulation of the muon background is a very CPU-time consuming task. Using CORSIKA with standard settings for air-shower production, only 15 days of lifetime of background events were simulated. In order to increase these statistics, an optimized simulation chain, proposed in [Kow04], has been used. The method is applicable to high-energy cascades and is based on the following observation: the reconstructed events of higher energies ( $E_{casc} > 1$  TeV) have secondary particles with energies larger than 500 GeV. Increasing the energy threshold for secondary particles, as well as the thresholds for muons and primary particles, one can generate large statistics of background events. Excluding in this way low-energy events, the background event sample which has to be processed is reduced to about 1%, and the same reduction factor applies to the CPU processing time. There were two additional background MC samples produced in this way. The first one was used to estimate the background expectation for events with reconstructed energies above 1.25 TeV and the second one for energies larger than 5.5 TeV.

Table 5.2 summarizes the statistics and the parameters used for those optimized samples. In Figure 5.2, on the left, one can see the distributions of the reconstructed energies for each of the three generated background

samples. The right plot shows the ratio between the standard and optimized MC sample 1. The ratio is nearly constant at higher energies and this sample can be used with an appropriate energy cut at 1.25 TeV.

BG sample	$E_{\text{cut}}^{\text{primary}}$	$E_{\text{cut}}^{\mu}$	$E_{\text{cut}}^{\text{secondary}}$	$E_{\text{reco}}$ range	statistics
standard	800 GeV	300 GeV	0.5 GeV	any energy	15 days
optimized sample 1	3 TeV	1.2 TeV	500 GeV	> 1.25 TeV	880 days
optimized sample 2	20 TeV	3.0 TeV	800 GeV	> 5.5 TeV	4670 days

Table 5.2: Summary of the atmospheric muon background samples used in this analysis.

## 5.4 The AMANDA Detector Simulation

The Cherenkov photons produced by charged secondary particles of the simulated neutrino or muon background events have to be propagated through the AMANDA detector. In order to simulate the AMANDA detector response, the AMASIM [Hun99] program was used. It simulates the detector readout electronics and the data acquisition system for MC events. For each detected photon, a waveform pulse, based on the laboratory measurements of the Photo Multiplier Tube (PMT) response to a photo-electron, is generated. Note that the dark noise of the PMT tubes is also taken into account. In addition, the cases of saturation due to large pulses are handled properly. We refer to Chapter 4 for a more detailed description of the AMANDA readout system.

The first step which needs to be simulated carefully is the propagation of the photon through the ice, and the probability for each Optical Module (OM) to detect it. For this purpose, two programs are used, which compute the photon intensity and time distributions and store them in a set of tables: PTD and PHOTONICS (described in detail in Chapter 8). For this analysis, the newest version of the PHOTONICS program was too slow and not properly tested. Two of the latest PHOTONICS releases, which are twice slower than PTD, were employed to generate a MC sample for systematic studies; the main analysis was then performed with PTD.

For a proper simulation of the OM response, one has to take into account various parameters of the OM components. Firstly, the PMT of the OM has an efficiency of about 25% and this number varies from module to module.



A detailed study of the OM efficiency will be described in Chapter 8. The efficiency of the optical gel and the glass vessel surrounding the PMT is also not the same for all modules, and it contributes to the total OM efficiency.

Apart the well-understood and simulated parts of the AMANDA detector readout, there are several issues which are not taken into account by AMASIM. Electronic component noise and cross-talk caused by twisted pair cables are not simulated for MC events, as well as smaller effects due to the change of the weather conditions for different seasons. In order to bring simulated events in a good agreement with the experimental data, the *hit-cleaning* procedure, which will be described in Chapter 6, was performed for the data samples where hits of non-physical origin are removed and data are subsequently re-triggered. Only those events which passed the re-triggering were used for the event reconstruction.



# Chapter 6

## Event Reconstruction

This chapter describes the methods used to reconstruct cascade-like and muon events. The event reconstruction is based on the arrival times of the Cherenkov photons. The AMANDA detector allows one to reconstruct a set of parameters for both cascade and muon channels. For muons, the track direction, position and time of the interaction, described by the set of variables  $(\theta, \phi, x, y, z, t)$ , can be reconstructed with a good precision using the AMANDA records. A significant advantage of the cascade channel respect to the muon one is a good precision for the energy reconstruction. However, the quality of the cascade direction reconstruction is poor compared to the muon channel. Due to the local cascade light emission, the information on the direction of the incoming particle is lost; the emission can be considered as nearly isotropic. At neutrino energies above 100 PeV, bremsstrahlung and pair-production effects are suppressed by the Landau-Pomeranchuk-Migdal (LPM) effect [LLD53, Mig56], which leads to a longitudinal extension of the cascade and a possible better angular resolution. In this work, neither elongation of the cascades nor LPM effect were taken into account, because at the moment of the analysis these options were not available in the simulation software.

Section 6.1 and Section 6.2 are devoted to the first data processing steps: hit cleaning and first-guess cascade reconstruction. The reconstructions of the cascade vertex position and energy are discussed in Section 6.3 and Section 6.4. Finally, muon track reconstruction is described in Section 6.5.

The reconstruction algorithms for cascade-like events are based on the maximization of the likelihood function, a very-consuming CPU time process. Therefore, a simple *first-guess* method was performed for the full data set. The main aim of this reconstruction is to reduce the muon background and to estimate those parameters which can be subsequently used for the likelihood reconstruction.

## 6.1 Hit Cleaning

The data recorded from the AMANDA detector contain the arrival times of the photons, the number of the fired Optical Modules (OMs) and the amplitude of the signals. All this information is stored on magnetic tapes. Besides information about the Cherenkov light, the data record contains also several types of noise caused by the Data Acquisition System. The dark noise of the PMTs, the electronic noise generated by amplifiers and the noise caused by the cross-talk in neighboring twisted pair cables are effects to be taken into account and removed before the data are processed. In addition, the information from the known set of OMs which are not operating properly must be flagged and not used in the analysis.

### Bad Optical Module removal

There is a known list of OMs which never worked after deployment. The data records related to these OMs are removed from this analysis. In addition, due to aging effects, every year additional OMs become unreliable. This OM selection is done using the AMANDA monitoring data [AMAb]. They provide average numbers for certain passing criteria, i.e. dark noise rates, Analog to Digital Converter (ADC) and Time to Digital Converter (TDC) rates. The description of the selection procedure can be found in [Rib]. The bad OM selection is a very important step for the reconstruction of cascades, especially for the energy reconstruction described later in this chapter. For the data of 2000, there are three periods with separate lists of OMs excluded from the analysis. All other years (2001-2004) have one list per year.

### Time Over Threshold cleaning

In order to remove the noise generated in amplifiers and picked up by cables, as well as the noise due to cross-talk, a Time Over Threshold (TOT) cleaning was performed. Analyzing the TOT distribution of each pulse, i.e. the time between the recorded leading and trailing edges, one can identify the pulses caused by noise. The shape of the noise pulse is different from the photoelectron pulses, and the resulting TOT value is smaller for the noise. In order to remove the hit contribution below the selected value corresponding to the noise signal, an individual cut was developed for each OM; usually it varies between 75 ns and 200 ns. For the set of modules with optical readout, the required cut was  $TOT > 5$  ns because of the lower noise rate for these channels.

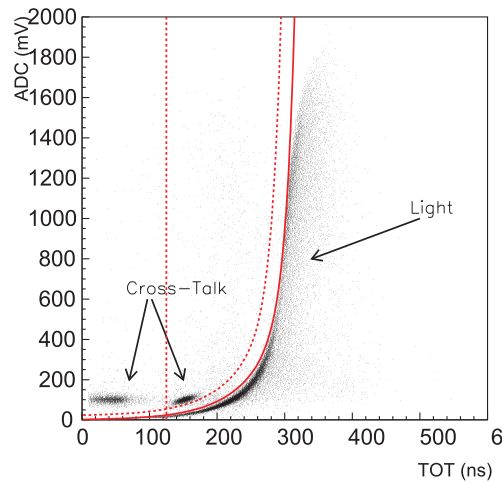


Figure 6.1: The ADC amplitude distribution as a function of Time Over Threshold (TOT).

### Time Window Cleaning

The time window cleaning is based on the observation that most of the light from cascade events and muons passing through the detector is detected in a very short time interval. In fact, a muon crosses the AMANDA detector in less than  $2 \mu s$ . The AMANDA data acquisition system records all pulses in a time interval between  $-22 \mu s$  and  $10 \mu s$  around the event trigger. Applying a more narrow time window  $[-2.5 \mu s, -4.5 \mu s]$ , a large fraction of the dark noise caused by the PMTs is removed.

### Amplitude and isolated hit cleaning

If a hit is isolated in space and time, it is likely to be produced by dark noise. All hits which do not have a partner in any OM in a 500 ns time interval and in a radius of less than 100 m away from the module are removed.

Sometimes it happens that the ADC information of the hit is missing. For example, this is the case for low amplitudes, where the uncertainty on the true arrival time of the hit is getting very large. Also these hits are removed in order to avoid a bias in the event reconstruction.

### Cross-talk Cleaning

Electronic cross-talk occurs in the twisted quad cables used in strings 5-10 of the AMANDA detector. The hit cleaning algorithms described above are not efficient to remove the cross-talk noise; only a TOT cut removes a

significant fraction of the cross-talk. However, since the cross-talk is induced by pulses with high amplitudes, the TOT cut cannot suppress the cross-talk hits without removing a large fraction of the real signal.

A special hit cleaning was developed in order to remove this electronic effect in [Tab02] using the idea that the ADC-TOT correlation is not linear. Figure 6.1 shows the ADC amplitude distribution for Optical Module #149 as a function of the TOT where one can clearly see the cross-talk hit population. The solid line shows the fit function obtained by fitting the photon signal induced by an in-situ light source. The function is shifted by  $-20\text{ ns}$  in TOT and is used as a selection cut, marked in Figure 6.1 by the dotted line, to remove pulses caused by cross-talk which remain on the left side of the line. The vertical line illustrates the TOT cut which is used before cross-talk cleaning and removes part of the cross-talk at an earlier cleaning level. All hits on the right side of the dashed line were used for the event reconstruction.

## 6.2 A First-Guess Algorithm for Cascades

After the hit cleaning, the number of hits in the data sample is still too large to be reconstructed by time consuming reconstruction methods. Here one needs a fast method to estimate the main cascade characteristics and remove selected events which cannot be reconstructed as cascades. Such types of reconstruction methods are known as *first-guess* methods.

A fast algorithm, called *c\_first* [KT01], is placed at the beginning of the reconstruction chain in this analysis. *c\_first* provides a fast estimate of the vertex and the time of the cascade.

The first parameter computed by *c\_first* is the cascade vertex position with respect to the center of the AMANDA detector,  $\vec{r}_c$ . It is estimated as a Center Of Gravity (COG) of the event, according to the distribution of hits in the Optical Modules. Each vertex position,  $\vec{r}_c = \{\vec{r}_{hit}, w_{hit}^1\}$ , is also weighted by the amplitude of the first hit,  $w_{hit}^1$ . The resolution for the first-guess vertex reconstruction is about 14 m inside the fiducial volume of the AMANDA detector, which can be approximated as a cylinder of 100 m radius and 400 m height.

Another parameter estimated by *c\_first* is the cascade vertex time. The algorithm takes into account the fact that photons do not propagate through the ice on a straight line to the OMs, but they are rather scattered. The residual (or delay) time of the photon can be defined as:

$$t_{res} = t_{hit} - t_{vtx} - \frac{d_{hit}c_{ice}}{c} \quad (6.1)$$

Here  $t_{hit}$  is the time of the hit,  $t_{vtx}$  the time of the vertex interaction and  $d_{hit}$  is the distance between the COG and the fired OM. To estimate the vertex-time  $t_{vtx}$  the shifted residual time is calculated:

$$t'_{res} = t_{res} + t_{vtx} = t_{hit} - \frac{d_{hit}}{c_{ice}}. \quad (6.2)$$

In a 200 ns time window, starting at  $t'_{res}$ , one calculates the number of hits,  $N_{dir}^{0:200}$ , which occur within 100 m from the estimated vertex position and have a delay  $t_{res} < 200$  ns. The vertex time is given by the smallest  $t'_{res}$  with a minimal required number of hits,  $N_{dir}^{0:200} > 4$ . If the trigger condition is not satisfied, the cascade vertex time is given by the time of the first hit within a 30 m sphere around the vertex. The time resolution of the vertex reconstruction is about 100 ns. This algorithm returns two important variables which are later used in order to discriminate the signal from the background:

- $N_{early}$ : the number of early hits with a time  $t_{res} - t_{max} < -200$  ns. Here  $t_{max}$  is used instead of  $t_{vtx}$ , and it corresponds to the time residual with the largest number of hits arriving within the next 200 ns. For the cascade hypothesis, the early hits are very unlikely, so one expects only a small number of them.
- $N_{dir}^{0:200}$ : the number of hits in the 200 ns bin after the estimated vertex time. This variable has a large discriminating potential and efficiently allows to separate the background from the signal at the first reconstruction level. More details will be given in Chapter 7.

The estimated vertex position,  $\vec{r}_c = \{\vec{r}_i, w_i^1\}$ , and the residual time,  $t_{res}$ , are used as seeds in more complex reconstruction algorithms which are described in the next section.

## 6.3 Vertex Position Reconstruction

### Single Photo-electron Reconstruction

The reconstruction of the vertex position and time is based on a likelihood minimization method. This method takes into account absorption and scattering of light in the ice and is performed in two steps.

In order to construct the likelihood function for the first reconstruction step, the time information from the first arrival photon is used. Thus, this function is called single photo-electron (*spe*) time likelihood function. To

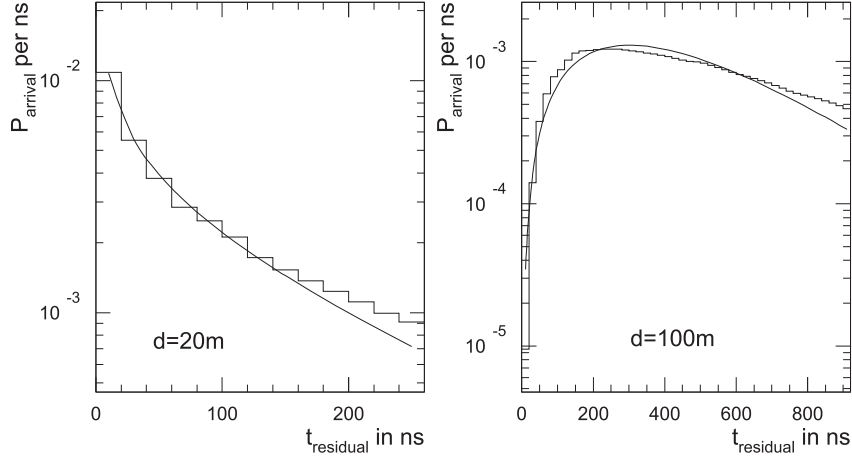


Figure 6.2: Dependence of the arrival time probability density functions on the time residual. The left plot shows the  $p(t, d)$  distribution for  $d=20$  m and the right one the same parameter for  $d=100$  m. The parametrization for the residual time (solid line) has been obtained in [Kow99] fitting these distributions.

construct the likelihood function, the time residual  $t_{res}$  of Eq.(6.1) is used. In the following we simply define:  $t \equiv t_{res}$ . The function is constructed as an analog to a reduced  $\chi^2$  and afterwards minimized:

$$\mathcal{L} = \prod_{hit=1}^{all\ hits} p(t, d), \quad L = \frac{-\log(\mathcal{L})}{N_{hits} - N_{free}}. \quad (6.3)$$

Here  $d$  is the distance between a hit OM and the reconstructed vertex position,  $N_{hits}$  is the total number of hits and  $N_{free} = 4$  is the number of free parameters: three space coordinates and time. The normalized probability density function  $p(t, d)$  for observing a time residual as a function of the distance is called *Pandel function* [Pan96]:

$$p(t, d) = \frac{\tau^{d/\lambda} t^{(d/\lambda-1)} e^{-(t+c_{ice}t/X_0+d/X_0)}}{\Gamma(d/\lambda)}. \quad (6.4)$$

The residual time is strongly correlated with the distance of photon propagation in ice,  $d$ . For distances shorter than the effective scattering length the mean time residual is close to zero. However, for larger distances, the probability for the photon to be scattered increases; therefore, the mean residual time is shifted to later times. The detailed Monte Carlo simulation of light propagation in ice was performed in [Wie96]. The distributions of the residual times obtained from this simulation are shown for two different distances in Figure 6.2.



The parameterization values for the Pandel function were derived in [Kow99] after fitting Eq. (6.4) to a full photon MC simulation. The obtained parameters, scattering time, scattering length and absorption length, are:  $\tau = 98$  ns,  $\lambda = 47$  m and  $X_0 = 450$  m. The smooth line in Figure 6.2 shows a parameterization for 20 m and 100 m distances. As one can see, the parametrization describes the MC distributions only approximately.

The effects of the electronic PMT jitter  $\sigma_{jitter}$  are not included in the parameterization of the Pandel function of Eq. (6.4). In order to properly account for the jitter, one has to convolute the Pandel function with a Gaussian with a width equal to the jitter. This convolution was not computed analytically but the approximation known as *patched* Pandel function was used. Here the Gaussian was added to allow for negative  $t$  values and adapted to be continuous. The resulting function is:

$$p^{patched}(t, d) = \begin{cases} G(t), & t \leq 0 \\ P_2(t), & 0 < t < t_{patched} \\ p(t, d), & t \geq t_{patched}. \end{cases} \quad (6.5)$$

$G(t)$  is a Gaussian function with width  $\sigma_{jitter}$ ,  $P_2(t)$  is a polynomial function of the second order and  $t_{patched} = \sqrt{2\pi}\sigma_{jitter}$ . The parameters of  $P_2(t)$  and  $G(t)$  are chosen such that  $p^{patched}(t, d)$  is a continuous and differentiable function.

### Multi Photo-electron Likelihood Reconstruction

The single photo-electron (spe) likelihood minimization method, based on the patched Pandel function, is the fastest method for the cascade position and time reconstruction. However, for bright cascade events, many photo-electrons contribute to a signal, and each OM registers multiple hits. In this case, the patched Pandel function does not properly represent time residuals, because only the time of the first photon is recorded in presence of other photons.

Assuming the detection of  $N$  photo-electrons, where the first photo-electron has a residual time  $t_{res} = t$ , one can calculate the probability density function for time delays as a function of the distance:

$$p(N, t, d) = N p(t, d) \left[ \int_t^\infty dt' p(t', d) \right]^{N-1}, \quad (6.6)$$

where  $p(t, d)$  is the patched function computed according to the procedure described in the previous section. The integral represents the probability that one photo-electron arrives with a time delay larger than  $t$ . To estimate the number of registered photo-electrons, the amplitude of the integrated pulse is used.

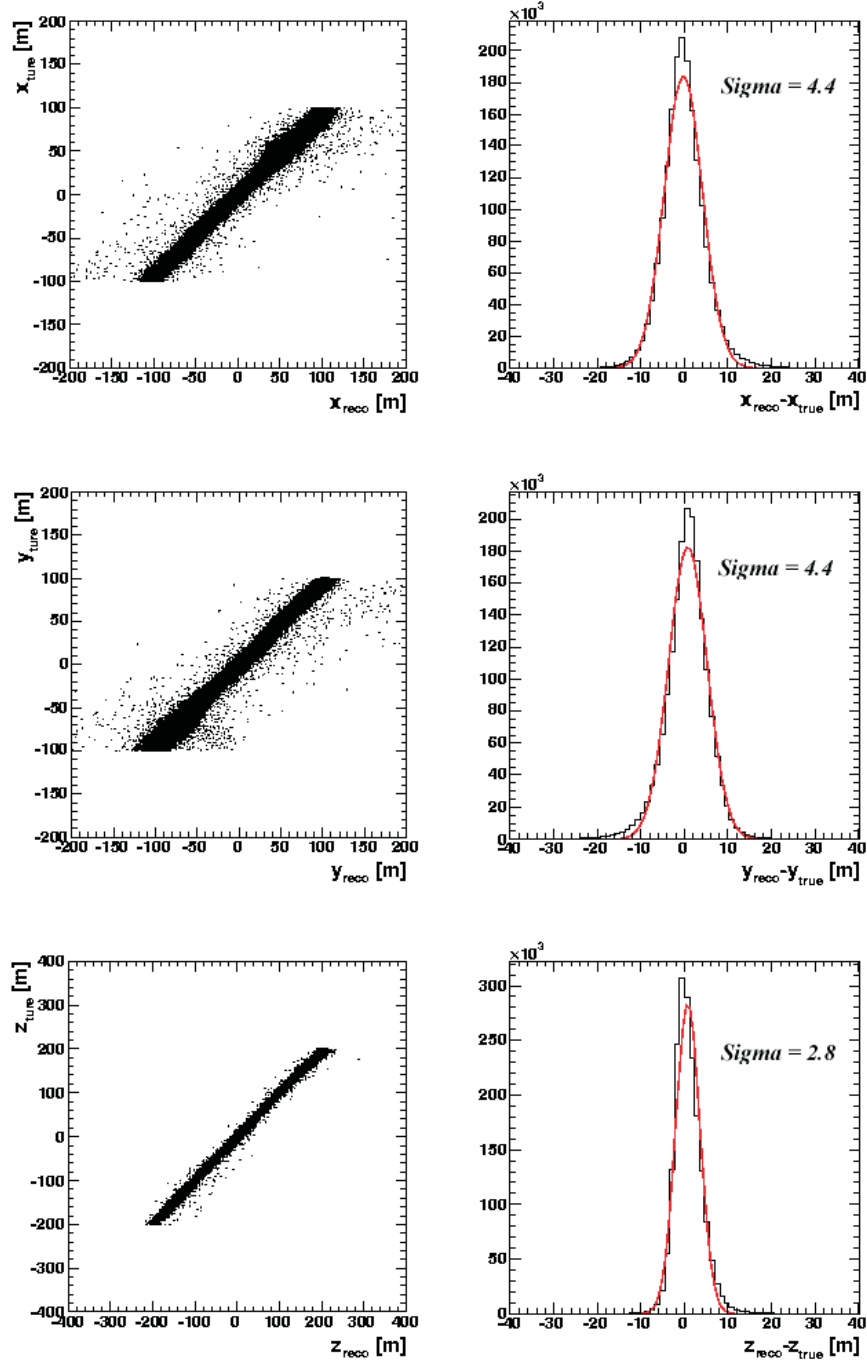


Figure 6.3: The resolution results of the mpe-likelihood vertex reconstruction for the  $x, y, z$  vertex position coordinates in the AMANDA detector.

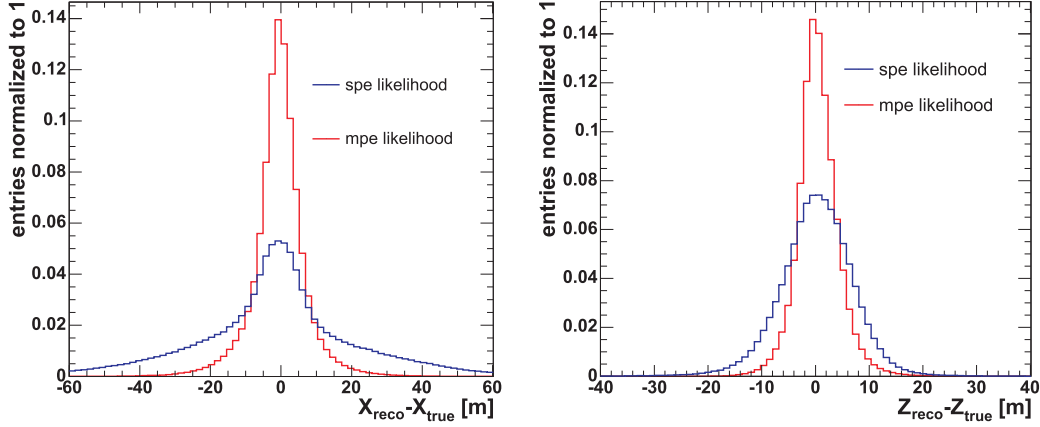


Figure 6.4: The resolution for the x and z vertex coordinates obtained from single photo-electron likelihood reconstruction (blue line) compared to the resolution obtained from multi photo-electron likelihood reconstruction (red curve).

Figure 6.3 shows the results for the vertex reconstruction of 1 TeV cascades using the *multi photo-electron* (mpe) likelihood method. The resolution for the x and y vertex position coordinates is about 4.4 m, and for the z coordinate is 2.8 m. The resolution for the x and y coordinates is similar due to the fact that the Optical Modules in AMANDA are spaced regularly in a horizontal plane. For the vertical direction, z, they are distributed more frequently, hence the vertex position resolution is better.

The vertex position resolutions obtained by spe and mpe likelihood methods are compared in Figure 6.4. In general the resolution for mpe reconstruction is better; this fit was used for the analysis.

## 6.4 Energy Reconstruction

The maximum likelihood method was used also for the energy reconstruction. The difference respect to the vertex reconstruction is that the likelihood here is given by the probability of observing a certain hit pattern. The number of photo-electrons detected by a photo-multiplier follows Poisson statistics:

$$P(N) = \frac{\eta^N e^{-\eta}}{N!}, \quad (6.7)$$

where  $\eta$  is the expected number of photo-electrons. In AMANDA the number of photo-electrons cannot be measured directly but one can compute the

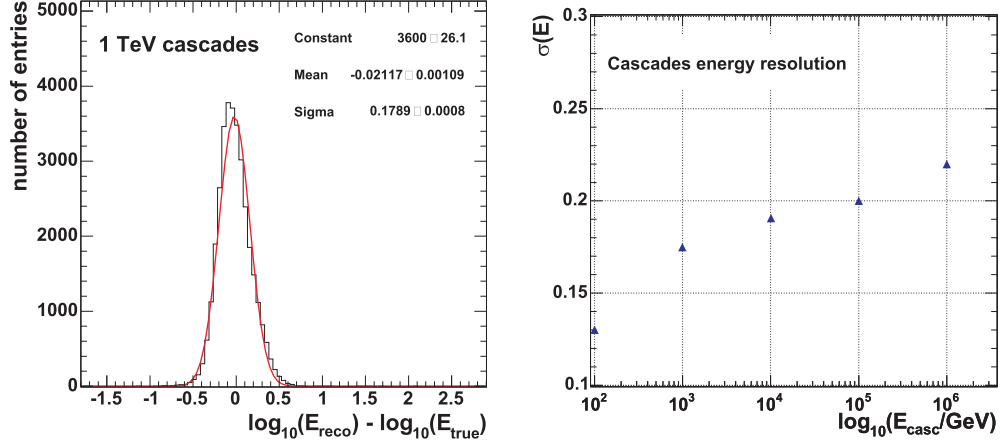


Figure 6.5: The performance of the energy reconstruction with AMANDA using phit-pnohit algorithm. Left: the energy resolution for 1 TeV cascades. Right: The reconstructed energy resolution as a function of the cascade energy.

probability for each Optical Module to obtain at least one hit due to cascade light emission:

$$P_{hit}^{casc} = 1 - P_{nohit}^{casc} = 1 - e^{-\eta}, \quad (6.8)$$

where  $e^{-\eta} = P_{nohit}^{casc}$  is the probability to obtain no hit. In order to perform a realistic estimate of the hit probability one has to include the probability to observe a PMT noise hit. To this aim, one can modify the equation including the probabilities of noise detection:

$$P_{hit} = P_{hit}^{casc} + P_{noise} - P_{hit}^{casc} P_{noise}. \quad (6.9)$$

For distances larger than the photon scattering length,  $d \gg \lambda_{scat}$ , Cherenkov photons undergo multiple scattering and the information on the direction of the photon vanishes. At these distances the scattering of light can be correctly represented by the effective scattering length  $\lambda_{scat}^{eff}$ , with an isotropic scattering angle. Note that the number of expected photons,  $\eta$  of Eq. (6.7), is a linear function of the cascade visible energy. For isotropically-emitting point-like cascades, one expects the following mean-number dependence on the distance [Kow04]:

$$\eta = I_0 \frac{E}{d} e^{-d/\lambda_{att}}, \quad (6.10)$$

where  $\lambda_{att} = \sqrt{\lambda_{scat}^{eff} \lambda_{abs}/3}$  is the attenuation length which is about 29 m for Cherenkov wavelengths. The normalization constant  $I_0$  depends on the OM orientation and the direction of the cascade and can be obtained fitting Eq. (6.8). Averaging over the angle and the OM orientation one obtains  $I_0 = 1.4 \text{ GeV}^{-1}$ . Both normalization constant and attenuation length values are calculated in [Kow04].

A likelihood function for the hit observation is constructed as the product of the  $P_{hit}$  and  $P_{nohit}$  functions:

$$\mathcal{L} = \prod_{i=1}^{all \ hit \ OM} P_{hit}(E, d) \prod_{i=1}^{all \ nohit \ OM} P_{nohit}(E, d), \quad (6.11)$$

$$L = -\frac{\mathcal{L}}{N_{OM} - N_{free}}. \quad (6.12)$$

Here  $N_{OM}$  is the total number of hit OMs and  $N_{free} = 1$  is the number of fit parameters. Similarly to the vertex likelihood function defined in Eq. (6.3), this function is also constructed as an analog to a reduced  $\chi^2$ . The resolution of this reconstruction depends on the cascade energy. In Figure 6.5, on the left, one can see the performance of the reconstruction for a cascade energy of 1 TeV. The right plot shows the resolution for different energies of the simulated cascades from  $10^2$  to  $10^6$  GeV. All events shown here have passed a vertex likelihood cut,  $L_{vertex} < 7.1$ .

## 6.5 Iterative Muon Likelihood Fit

Nearly all fits for this analysis are performed in order to reconstruct cascade-like events with the exception of the 16-iterative muon likelihood fit. The muon likelihood fit was used as a subsidiary reconstruction in order to build an important quality parameter used afterwards for cut optimization (see Chapter 7).

The iterative likelihood reconstruction uses the Pandel probability density function of Eq. (6.4). A correction for the PMT jitter, as well as a correction factor due to the anisotropic angular efficiency of the Optical Module, were taken into account [W<sup>+</sup>04]. The minimization procedure was performed on the resulting likelihood function:

$$\mathcal{L} = \prod_{i=1}^{all \ hits} p(t_{res}^i, \rho_i). \quad (6.13)$$

When a minimum,  $\min(-\mathcal{L})$ , is found, this procedure is repeated 16 times with different random track directions around the possible minimum candidate in order to find a better minimum. The track with the highest likelihood was used for the analysis.

# Chapter 7

## Data Analysis

The goal of this investigation is the detection of the astrophysical diffuse flux of high-energy electron and tau neutrinos through observation neutrino-induced cascades using 5 years (2000-2004) of the AMANDA data. The total number of triggered events during the five-year period is about  $10^{10}$  events; most of them are muons produced in the atmosphere. At each level of the analysis the main aim is to reject the background and to select a data sample containing cascade-like events.

The analysis chain consists of several filter levels, each of them having a particular purpose. The structure of the analysis chain is shown in Figure 7.1. The *level 0* hit-cleaning procedure was described in Section 6.1 and is applied to both Monte Carlo (MC) and data samples in order to remove hits with a non-physical origin. The task of the *level 1* filter is to make a fast estimation of the important analysis parameters; using this information, a large fraction of the background can be rejected. The more complicated and CPU-time consuming analysis is performed at *level 2* in order to compute precise reconstruction parameters. However, at this level, too many events are not reliable. Therefore, two additional quality cuts are applied at the next analysis level, where a significant part of the background is reduced improving the data quality.

In Table 7.1 we summarize the analysis efficiency for experimental data and muon and atmospheric neutrino background at each reconstruction level. In addition, we show efficiencies for a hypothetical astrophysical electron neutrino signal with a flux strength of  $10^{-6}(\text{E}/\text{GeV})^{-2}/(\text{GeV s sr cm}^2)$ .

All cuts of the analysis were developed using the *blind* analysis technique (see, for example, [KR05]) in order to prevent possible biases in the selection criteria. Only 20% of the 5-year data sample were used to study the data selection cuts; after the analysis was accepted by the IceCube collaboration, the remaining 80% of the data were processed without changing the cuts,

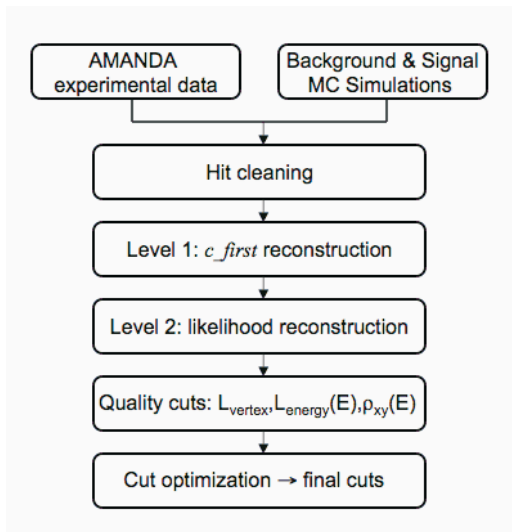


Figure 7.1: The block-diagram structure of the analysis described in this chapter.

leading to the final results.

In Section 7.1 and Section 7.2 the first- and second-level filters are described. Next, in Section 7.3, the additional quality cuts are analyzed in detail. The final event selection is discussed in Section 7.4.

## 7.1 First-Level Filter

The volume of the AMANDA detector, instrumented with more than 500 working Optical Modules, produces a large amount of information. At the trigger level the data sample is large to apply a full reconstruction. Therefore, the  $c\_first$  algorithm, described in Section 6.2, was used to perform a first-

cut variable	data	$\mu^{atm}$	$\nu_e^{atm}$	$E^{-2}\nu_e$ signal
$N_{early}/N_{hits}$	0.0018	0.0042	0.53	0.38
$N_{dir}^{0:200}$	0.0012	0.0022	0.49	0.33
$L_{vertex}$	$6.5 \times 10^{-4}$	$3.7 \times 10^{-4}$	0.32	0.24
$L_{energy}(E)$	$1.3 \times 10^{-4}$	$1.0 \times 10^{-4}$	0.27	0.17
$\rho_{xy}(E)$	$8.7 \times 10^{-5}$	$5.9 \times 10^{-5}$	0.12	0.095
$Q_S$	$3.5 \times 10^{-6}$	$2.1 \times 10^{-6}$	0.01	0.08

Table 7.1: The efficiencies of the analysis for experimental data, several types of background and an  $E^{-2}$  ( $\nu_e + \bar{\nu}_e$ ) signal.



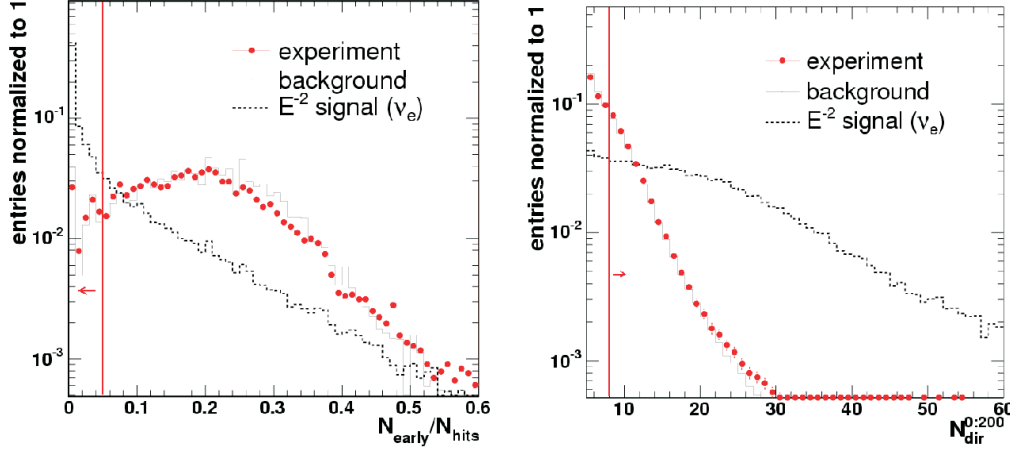


Figure 7.2: The parameters returned by the  $c$ -first reconstruction. Left: fraction of early hits over the total number of hits. Right: direct hits in the 200 ns time window. Experimental data, signal and background MC distributions are shown.

level reconstruction and to reduce the data to a few percent of the initial size.

The first variable returned by the first-guess algorithm,  $N_{dir}^{0:200}$ , is the number of hits with a residual time less than 200 ns after the estimated vertex time. Due to photon scattering, the delay time can be significant; taking this into account, all hits fulfilling the condition  $0 < t_{res} < 200$  ns are considered to be *direct* hits. Another important variable calculated by  $c\_first$  is the number of early hits,  $N_{early}$ . Early hits in cascade events are most likely generated by random noise or a wrong reconstruction of the vertex parameters. Both distributions,  $N_{dir}^{0:200}$  and  $N_{early}$ , have a high-discriminating potential to separate signal and background events. However, the analysis can be improved taking the ratio of  $N_{early}$  and  $N_{hits}$ . Moreover,  $N_{early}$  tends to increase with the growth of the cascade energy, as well as  $N_{hits}$  for high-energy cascades. Therefore, the ratio between these two variables is just slightly dependent on the energy.

Figure 7.2 illustrates the distributions of  $N_{early}/N_{hits}$  and  $N_{dir}^{0:200}$  for experimental data, atmospheric muon background and a hypothetical ( $\nu_e + \bar{\nu}_e$ ) signal falling as  $E^{-2}$ . The arrows in these plots show the fraction of events which are used in the analysis. The signal spectra for the fraction of early hits show that, for cascade events, the prediction for  $N_{early}/N_{hits}$  is very small. Experimental data and background MC distributions are clearly separated from the signal prediction. One can see that the background expect-

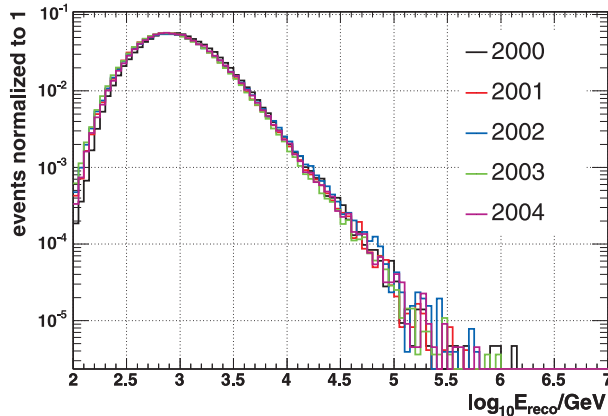


Figure 7.3: Reconstructed cascade energy for data of different years used in the analysis.

tation dominates over the signal one for events with  $N_{early}/N_{hits} > 0.05$  and for events with a low number of direct hits. Therefore, only events with  $N_{early}/N_{hits} < 0.05$  and  $N_{dir}^{0:200} > 8$  were selected for the analysis.

## 7.2 Second-Level Filter

The likelihood reconstruction of the cascade energy and vertex is performed at the second processing level. After the cuts applied at level 1, the data sample is small enough to be reconstructed by likelihood minimization methods.

### 7.2.1 Likelihood Vertex Position Reconstruction

The preliminary estimate of the cascade vertex position is done by the  $c\_first$  algorithm. The result of this reconstruction is used as a seed for the second level single photo-electron likelihood (spe-likelihood) reconstruction. The results of the spe-likelihood fit are used as an input for the next multi photo-electron likelihood (mpe-likelihood) fit. Both reconstruction methods were described in Section 6.3. The spe-likelihood reconstruction shows a slightly worse performance and it is used only as an auxiliary fit, while the result of the mpe-likelihood reconstruction is used for the further event selection.

## 7.2.2 Energy Likelihood Reconstruction

The energy reconstruction is performed by a likelihood minimization method. As it was shown in Section 6.4, the resolution for the cascade energy reconstruction is better than  $\Delta(\log_{10}(E_{reco})) < 0.2$ .

The likelihood algorithm for energy reconstruction is based on the hit information from all Optical Modules. The quality of the energy reconstruction strongly depends on the OM selection (see Section 6.1). Figure 7.3 shows the multi-year comparison of the reconstructed cascade energy. Note that the energy distribution shows a very good agreement for all years after the correct OM selection which has been done separately for each year.

## 7.3 Additional Quality Cuts

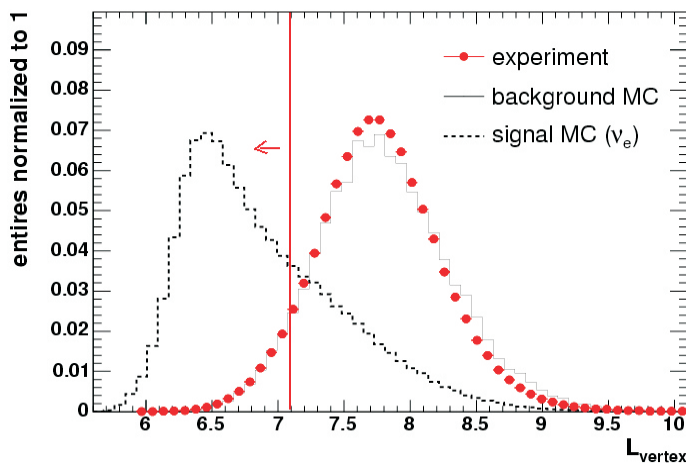


Figure 7.4: The mpe-likelihood vertex reconstruction parameter. The events shown here passed the first-level cuts. Experimental data, background MC and a hypothetical  $E^{-2}$  electron neutrino signal are shown in the plot.

After the data are processed and the first three cuts of the analysis have been implemented, three additional cuts were developed in order to improve the quality of the presented data and reduce the number of muon background events. The first cut uses the vertex likelihood parameter in order to assure the quality of the reconstructed cascade vertex. The second cut is applied on the energy likelihood parameter and the third one takes the radial distance of the reconstructed vertex position from the central axis of the detector.

### Vertex likelihood cut

The construction of the vertex likelihood parameter,  $L_{vertex}$ , was described in Section 6.3 (mpe-likelihood). Figure 7.4 shows the distribution of  $L_{vertex}$  for all events of the experimental, signal and background data samples which passed the first-level selection. Since the likelihood function was minimized in order to obtain the best vertex reconstruction, the best quality events correspond to those for which the  $L_{vertex}$  values are minimal. As one can see from the plot, this variable has also a high-discriminating potential. Here, a cut  $L_{vertex} < 7.1$  was applied in order to reduce the background to less than 10% of the initial size. Additionally, this cut removes also a fraction of about 30% of the hypothetical  $E^{-2}$  ( $\nu_e + \bar{\nu}_e$ ) signal. However, these events are very likely to be removed by the next level quality cuts, since they do not have a high probability to be part of the signal. The reconstructed

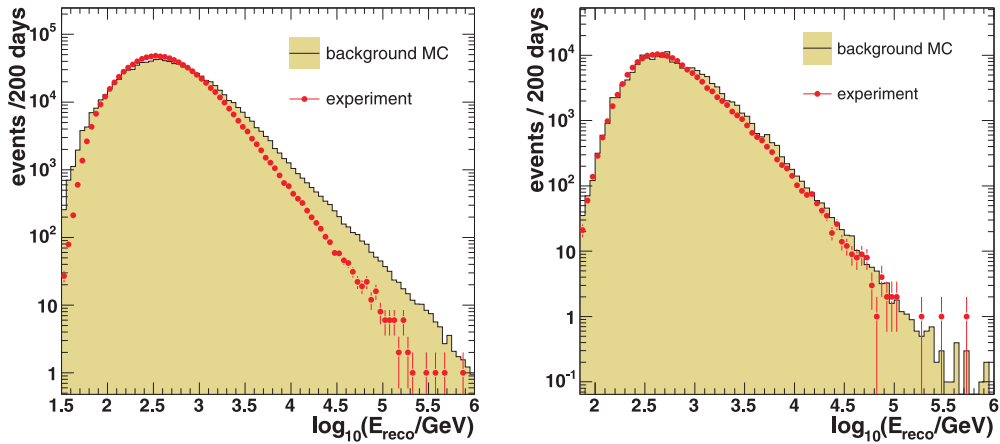


Figure 7.5: Left: reconstructed cascade energy for events which passed the vertex likelihood cut. Right: reconstructed energy for events which passed all quality cuts. Both pictures show the comparison of experimental data (20% of the full 5-year sample) to atmospheric muon background MC.

cascade energy distribution for the events which passed the first quality cut,  $L_{vertex}$ , is shown on the left plot in Figure 7.5. The reconstructed energy obtained for the experimental data sample corresponding to 20% of the 5-year data is compared to the atmospheric muon background Monte Carlo. The background expectation is scaled to the 200 days of the experimental data distribution. All events shown in the left plot passed the vertex likelihood cut. Note that the MC simulation does not describe the experimental data very well. Further quality cuts, discussed later in this section, were applied

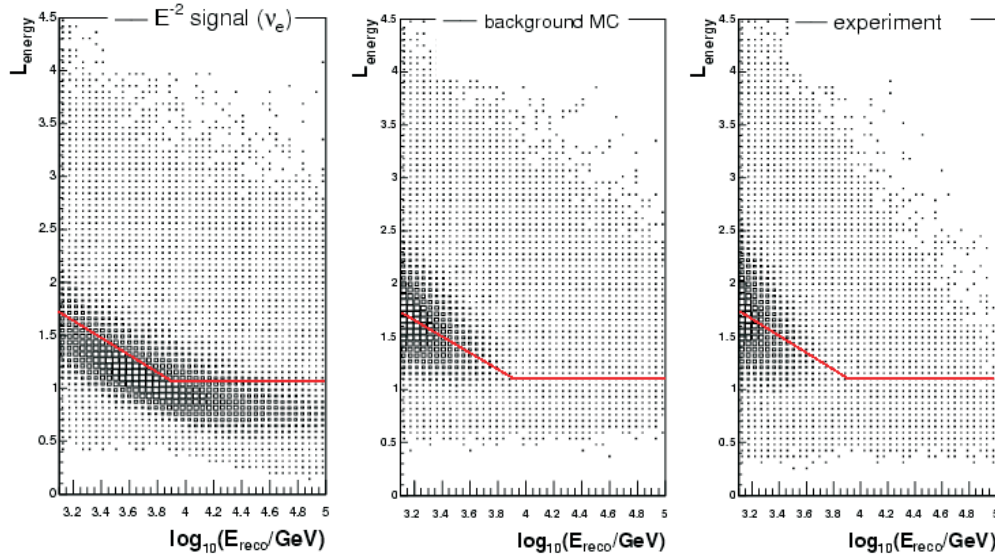


Figure 7.6: Energy likelihood reconstruction quality parameter as a function of the reconstructed cascade energy. The plots show an  $E^{-2}$  signal MC, atmospheric muon background MC and experimental data (from left to the right). The red line is the two-dimensional cut defined in Eq. (7.1).

in order to improve the description of the data and reduce the background.

The reconstructed cascade energy, compared to the experimental data and atmospheric background MC, is shown in the right plot in Figure 7.5 for events which passed all quality cuts. Note that the agreement between the MC and data samples significantly improves due to the quality-cut implementation which will be further described.

### Cut on the Energy Likelihood Parameter

The second quality cut uses the energy likelihood parameter. This variable, similar to the vertex likelihood,  $L_{vertex}$ , is a measure of the quality of the reconstruction. Small values of the parameter defined in Eq. (6.11) correspond to events with a good reconstruction. However,  $L_{energy}$  is energy dependent. A two-dimensional function was used to select an appropriate cut:

$$L_{energy} \leq \begin{cases} 1.1, & \log_{10}(E_{reco}) \leq 3.9 \\ -0.625 \times \log_{10}(E_{reco}/GeV) + 3.54, & \log_{10}(E_{reco}) > 3.9 \end{cases} \cdot (7.1)$$

Figure 7.6 shows the distribution of the energy likelihood function for the

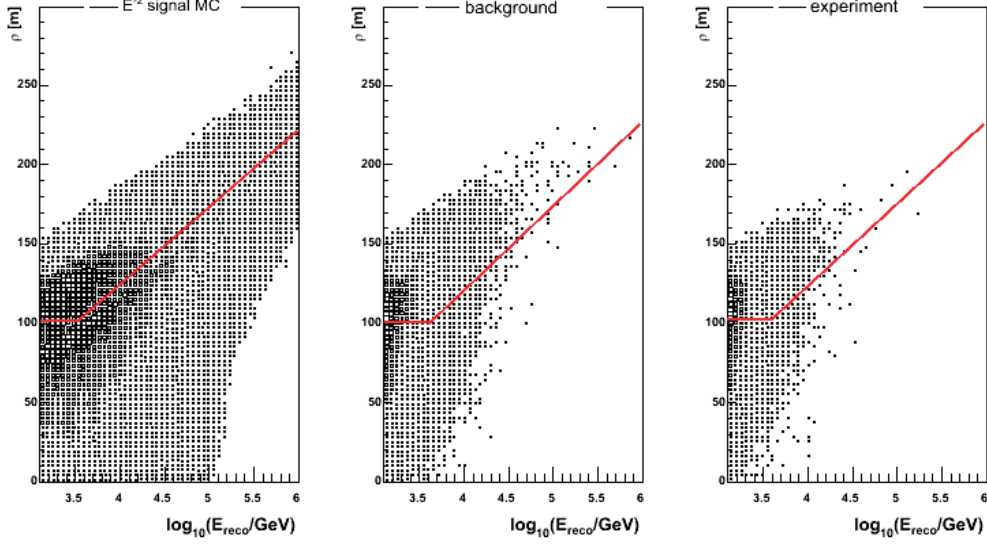


Figure 7.7: The reconstructed cascade vertex radial distance between the detector center and the vertex as a function of the reconstructed cascade energy. An  $E^{-2}$  ( $\nu_e + \bar{\nu}_e$ ) signal, background MC and experimental data are shown. The red line corresponds to the two-dimensional cut of Eq. (7.2) .

electron neutrino signal, background MC and experiment. The solid line shows the cut of Eq. (7.1). Only events below the line passed the cut. The choice for the cut function fulfills two requirements. First of all, events are selected in order to insure the quality of the energy reconstruction. This improves the agreement between data and background Monte Carlo. In addition, a significant fraction of background is reduced.

### Radial-Distance Cut

Only events reconstructed inside or close to the fiducial volume of the detector are trustworthy. In addition, the quality of the reconstructed events depends on their energy. If low-energy cascade-like events occur far from the detector, they are very unlikely to be properly reconstructed. The diameter of the fiducial volume of the AMANDA detector is limited by a radius of 100 m. In order to perform this selection, another quality cut was applied on the radial distance between the reconstructed cascade vertex and the central axis of the detector. For low-energy events, the radial cut at 100 m, which corresponds to the AMANDA fiducial volume, has been applied. For events with higher energies, this cut was relaxed in order to keep very bright

events with reconstructed vertices close to the detector. The cut is defined as:

$$\rho_{xy} \leq \begin{cases} 100 \text{ m}, & \log_{10}(E_{reco}) \leq 3.1 \text{ TeV} \\ 42.3 \times \log_{10}(E_{reco}/\text{GeV}) + 43.8 \text{ m}, & \log_{10}(E_{reco}) > 3.1 \text{ TeV} \end{cases} \quad (7.2)$$

Figure 7.7 illustrates the radial dependence of the reconstructed vertex on the energy of the cascade. This distribution is shown for experimental data, a hypothetical electron neutrino signal falling as  $E^{-2}$  and the atmospheric muon MC expectation. All events below the solid line, which represents the two dimensional cut, are chosen for the final selection.

## 7.4 Final Selection

The final selection of this analysis consists of two steps. In Subsection 7.4.1 we introduce an additional variable, the discriminating parameter  $Q_s$ . A two-dimensional cut optimization is performed using  $Q_s$  and the reconstructed cascade energy,  $E_{reco}$ . The final cut combination,  $(Q_s, E_{reco})$ , was selected in order to get the highest sensitivity of the detector to the astrophysical neutrino flux. This optimization process is discussed in Subsection 7.4.2.

### 7.4.1 Discriminating Parameter $Q_s$

#### Input parameters

For each event we construct the discriminating parameter  $Q_s$  as the probability for an event to belong to a signal class. In order to build this variable three variables are used:

- the vertex likelihood value  $L_{vertex}$ ;
- the radial distance,  $\Delta\rho_{xy}^{60}$ , between the vertex positions of two likelihood vertex fits; the second fit is thereby not using hits within a 60-meter sphere around the vertex position determined by the first fit;
- $\cos(\theta_\mu)$ , taken from muon track likelihood reconstruction (see Section 6.5).

The first variable,  $L_{vertex}$ , was previously discussed, and is used as a quality cut variable,  $L_{vertex} < 7.1$ . However, as one can see in the left plot of Figure 7.8, where the data, signal and background MC distributions for  $L_{vertex}$  are shown, this parameter has still some discriminating potential.

The second variable used to build the discriminating parameter is the radial distance,  $\Delta\rho_{xy}^{60}$ . The data, background and signal MC distributions

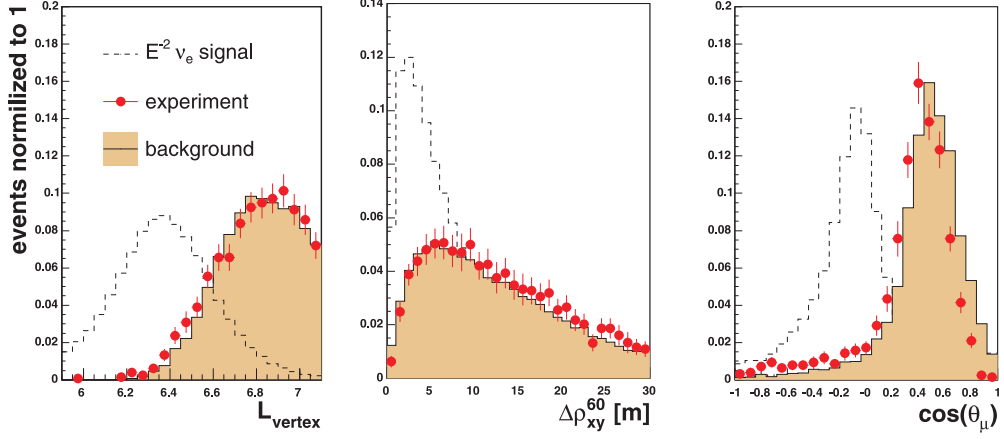


Figure 7.8: Experimental data,  $E^{-2} (\nu_e + \bar{\nu}_e)$  signal and background simulation as a comparison for the three parameters used to build the quality function,  $Q_s$ .

for this variable are shown in the middle plot of Figure 7.8. At this selection level there is still a fraction of muon events contaminating the data sample. These are mostly muon events with a bright cascade along the track. The cascade vertex reconstruction corresponds to this cascade. Removing the hits around the vertex, one emphasizes the muon track signature. Thus, the radial distance between the regular reconstructed vertex and the additional one, described above, has also a high potential to discriminate the signal from the muon background:

$$\Delta\rho_{xy}^{60} = \sqrt{(\rho_x - \rho_x^{60})^2 + (\rho_y - \rho_y^{60})^2}. \quad (7.3)$$

The last variable used for  $Q_s$  is based on the result of the 16-iterative spe muon likelihood reconstruction. From this fit  $\cos(\theta_\mu)$ , the cosine of the reconstructed zenith angle, is obtained; it is shown in the right of Figure 7.8, as usual for experimental data, signal and background MC. The signal events are mainly peaked around the value  $\cos(\theta_\mu) = 0$  because of the almost-isotropic cascade emission. Reconstructing such a signature with the muon hypothesis, the most preferable solution would be a horizontal muon track. There is some discrepancy between the simulated background MC distribution and the experiment. A reason for this difference could be an incorrect simulation of the ice structure. In Chapter 8 we will present studies of different ice models and a simulation of the light propagation in order to estimate the systematic uncertainties of the analysis.



### The construction of the discriminating parameter $Q_s$

For the construction of the discriminating parameter  $Q_s$  we used the set of observables described above,  $\vec{x} = (L_{vertex}, \Delta\rho_{xy}^{60}, \cos(\theta_\mu))$ . For this purpose the so-called Bayesian likelihood algorithm was chosen. It is motivated by Bayesian statistics which requires that the probability density function,  $P(\vec{x})$ , is known *a priori*. The conditional probability for observing  $\vec{x}$ , given the hypothesis  $\mathcal{H} = \{s, b\}$  to observe either a signal event ( $s$ ) or a background event ( $b$ ), is  $P(\vec{x}|\mathcal{H})$ . The Bayesian theorem gives the probability for  $\mathcal{H}$  under the observation of  $\vec{x}$ :

$$P(\mathcal{H}|\vec{x}) = \frac{P(\mathcal{H})P(\vec{x}|\mathcal{H})}{P(\vec{x})}. \quad (7.4)$$

In our case, the probability  $P(\mathcal{H})$  to have a certain hypothesis is not known. Therefore, the *a priori*  $P(\mathcal{H})$  is assumed to be a constant, with  $P(s) = P(b) = 0.5$ . The probability to observe  $\vec{x}$  is:

$$P(\vec{x}) = P(\vec{x}|s)P(s) + P(\vec{x}|b)P(b). \quad (7.5)$$

The Bayesian theorem of Eq (7.4) for observing the signal in this case can be written as:

$$P(s|\vec{x}) = \frac{P(\vec{x}|s)}{P(\vec{x}|s) + P(\vec{x}|b)}. \quad (7.6)$$

For our purposes, we face the problem of dealing with more than one observable. We adopt the simple solution of [A<sup>+</sup>01a], assuming no correlation between the observables. The probability to observe  $\vec{x}$  given a signal event,  $P(\vec{x}|s)$ , is then approximated to be the product of the one-dimensional probability density functions (PDFs) for each observable:

$$Q_s = \frac{\prod_i p_i^s(x_i)}{\prod_i p_i^s(x_i) + \prod_i p_i^b(x_i)}, \quad (7.7)$$

where the one-dimensional PDFs for the signal and background observations are defined as:

$$p_i^s(x_i) = \frac{f_i^s(x_i)}{f_i^s(x_i) + f_i^b(x_i)}, \quad p_i^b(x_i) = \frac{f_i^b(x_i)}{f_i^s(x_i) + f_i^b(x_i)}, \quad (7.8)$$

where  $i = 1, 2, 3$ . The functions  $f_i$  used for constructing the PDFs are  $f = (L_{vertex}, \Delta\rho_{xy}^{60}, \cos(\theta_\mu))$ . Each function for data, signal and background distributions is shown in Figure 7.8. They have been normalized to 1 and can

be considered to be PDFs. For each event, the values of the signal and background functions ( $f_s$  and  $f_b$ ) were evaluated for  $f = (L_{vertex}, \Delta\rho_{xy}^{60}, \cos(\theta_\mu))$  and used to build the discriminating parameter  $Q_s$ .

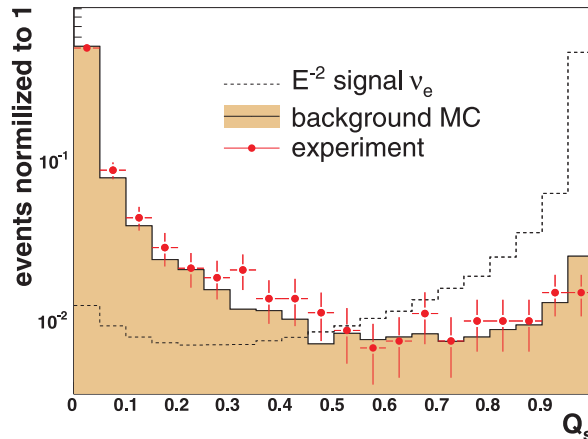


Figure 7.9: Distribution of the discriminating parameter  $Q_s$ . The distributions of experimental data, signal and background MC are normalized to 1. Events shown passed all the quality selection criteria defined before the final level selection.

Figure 7.9 illustrates the resulting distribution of the discriminating parameter  $Q_s$ . The experimental data are shown in comparison with the atmospheric muon background and a hypothetical  $E^{-2}$  electron neutrino flux. The differences between background distribution and experimental data in the range  $0.3 < Q_s < 0.5$  stems mainly from the disagreement in the  $\cos(\theta_\mu)$  distribution. The related uncertainties are included in the final result.

## 7.4.2 Cut Optimization

### Sensitivity

The detector sensitivity to the astrophysical neutrino flux is related to the detector effective area, as it will be shown in Chapter 9. In case of no background, one can optimize the performance for detection or rejection of the flux by maximizing the effective area. However, for the AMANDA detector, a large atmospheric muon background is always present. Hence, one has to find the optimum where the background is low and, at the same time, the neutrino effective area is still large enough to detect a signal neutrino flux.

We define the sensitivity of our analysis as the average flux upper limit that can be set with 90% confidence,  $\phi_{90\%}^{sens} \equiv \bar{\phi}$ .

The method we used to calculate this average upper limit was proposed by Feldman and Cousins in [FC98]. Firstly, assuming no signal observation, the possible number of observed events,  $n$ , is calculated for each possible number of background events,  $b$ . If the experiment is repeated many times, the number of observed events should follow a Poisson distribution:  $P(n|b)$ . The limit for a possible number of signal events, compatible with this background observation,  $\mu_{90\%}^{limit}$ , can be computed for each combination  $(n, b)$ . The average upper limit is calculated averaging over the probabilities for the experimental outcomes:

$$\bar{\mu}_{90\%}^{limit} = \sum_{n=0}^{\infty} \mu_{90\%}^{limit}(n, b) P(n|b). \quad (7.9)$$

This average upper limit depends only on the expected number of background events. One can calculate the sensitivity with respect to a certain neutrino flux with strength  $\phi_0$  dividing the  $\bar{\mu}_{90\%}^{limit}$  by the number of signal events,  $n_{sig}(\phi_0)$ , expected from this flux:

$$\phi_{90\%}^{sens} = \frac{\bar{\mu}_{90\%}^{limit}}{n_{sig}(\phi_0)} \phi_0. \quad (7.10)$$

Using Eq. (7.10) one can calculate the sensitivity, i.e. the average flux upper limit, for any spectrum of the neutrino flux. In Chapter 9 we will present the sensitivity of this analysis to various atmospheric and astrophysical neutrino flux models.

### Optimization procedure

The cut optimization was performed for the quality parameter  $Q_s$  and for the reconstructed cascade energy. The optimal cut doublet,  $(Q_s^{cut}, \log_{10}(E_{cut}))$ , was chosen in order to obtain the highest detector sensitivity. The optimization was performed in two dimensions:

1. the  $Q_s$  parameter (see Figure 7.9) was scanned in an interval  $[0.9, 0.99]$  with a step of 0.01; at each step the average upper limit ( $\bar{\phi}$ ) was calculated for different energy cuts ( $E_{cut}$ ). This is illustrated for  $Q_s^{cut} > 0.92$  in the left plot of Figure 7.11;
2. after the optimal  $E_{cut}$  was obtained for each  $Q_s$ , the corresponding average upper limit for each  $(Q_s, E_{cut})$  combination was expressed as a function of  $Q_s^{cut}$  (see right plot in Figure 7.11).

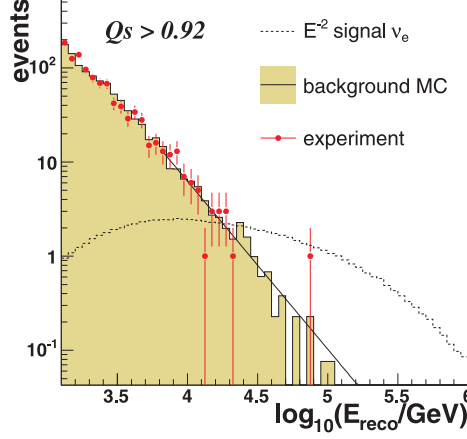


Figure 7.10: The reconstructed cascade energy for the quality parameter cut  $Q_s^{cut} > 0.92$ . The distributions of signal and background MC are normalized to the 20% of the experimental data shown here. The power-law fit to the background, shown as a black solid line, was used for the cut optimization.

The average upper limit depends on the number of background events remaining in the sample after the cuts. The statistical fluctuations can considerably influence the output of the optimization. To avoid this effect, the background distribution of the reconstructed energy was fitted with a power-law function for each value of  $Q_s^{cut}$  (first optimization step) starting from  $\log_{10}(E_{reco}) = 3.81$ . The parametrization for the fit was used to calculate the number of background events for the average upper-limit computation in the optimization procedure. In order to maintain blindness, the optimization was performed using only 20% of the experimental data sample. The reconstructed energy distribution for the 20% statistics is shown in Figure 7.10. The background spectrum was rescaled to the experimental data in order to obtain the 5-year background expectation for the total detector up-time used in this analysis. Hence, using this method of re-scaling, we optimized our cuts for the 5-year AMANDA data following all restrictions of the IceCube collaboration blindness policy and keeping 80% of the data unprocessed. The left plot in Figure 7.11 shows the average upper limit,  $\bar{\phi}$ , for the energy cut ranging in an interval given by  $\log_{10}(E_{cut}) \in [4.4, 6.0]$ , with a step of 0.03 and a discriminating parameter cut fixed at  $Q_s^{cut} > 0.92$ .

The right plot in Figure 7.11 illustrates the average upper limit values obtained from the first step of the optimization as a function of the  $Q_s^{cut}$ . The minimum of this distribution is given by cut parameters  $Q_s^{cut} > 0.92$  and  $E_{cut} > 4.65$ . For a hypothetical  $\nu_e$  flux falling as  $E^{-2}$  with a strength

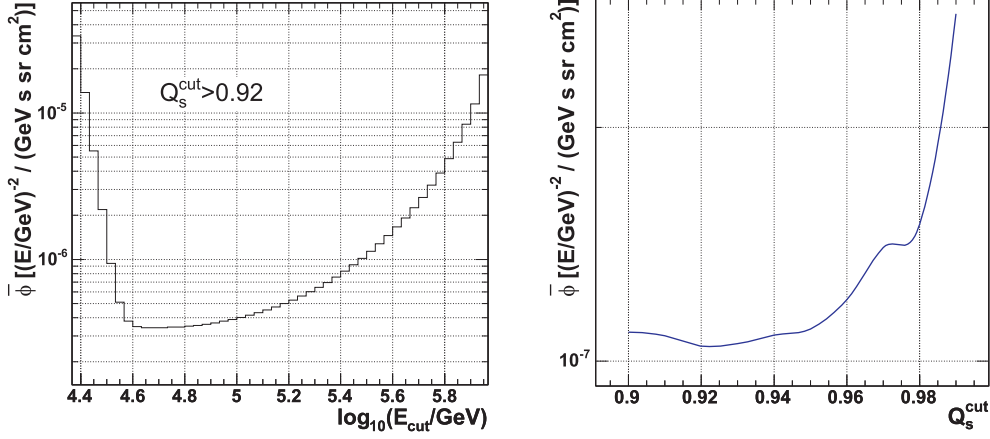


Figure 7.11: Left: Average upper limit for a  $\nu_e$  flux as a function of the energy cut. The distribution is shown for  $Q_s^{\text{cut}} > 0.92$ . Right: The average upper limit, according to the energy optimization, is shown as a function of  $Q_s^{\text{cut}}$ . The minimum corresponds to the best average upper limit for a  $\nu_e$  flux equal to  $2.7 \cdot 10^{-7} (E/\text{GeV})^{-2}/(\text{GeV s sr cm}^2)$ .

of  $10^{-6}(E/\text{GeV})^{-2}/(\text{GeV s sr cm}^2)$ , the cuts obtained from the optimization lead to an average upper limit equal to  $2.7 \cdot 10^{-7}(E/\text{GeV})^{-2}/(\text{GeV s sr cm}^2)$ . Note that we used the power-law fit for the background distribution in order to perform the optimization. However, the final sensitivity has been obtained with the number of background events coming from the distribution itself.

All selection parameters obtained in this analysis were finally applied to 100% of the AMANDA data sample as well as to signal and background MC. The results obtained from the final data sample, as well as the effective detector size for the analysis, are presented in Chapter 9. The estimate of the systematic errors which were taken into account to obtain the final results are discussed in the next chapter.



# Chapter 8

## Systematic Uncertainties

The analysis performed in this thesis is biased by several systematic effects, which will be described in this chapter. Two groups of systematic uncertainties can be recognized. The first one is related to the limited accuracy of the measurement of each event parameter: the precision of the detector space and time calibration, as well as the time dependence of the sensitivity of the Optical Modules, contribute to the systematic error. The second source of systematic uncertainties is connected to the Monte Carlo simulation of the signal and background expectations. As we showed in Section 3.1, at high energies the predictions for the neutrino cross section are rather uncertain. Furthermore, the simulation of the neutrino propagation through the Earth is affected by the limited knowledge of the Earth structure. Another problem of the Monte Carlo simulation is the description of the photon propagation through the ice. Here one needs a precise ice model where the ice structure is represented with high accuracy. However, the ice model used for the simulation performed in this analysis describes the Antarctic ice just approximately. This additional effect has to be included in the systematic error of the measurement.

In Section 8.1 we discuss details of the implementation of the ice properties in our analysis. Next, in Section 8.2, we describe the Photo-Multiplier efficiency and in Section 8.3 we analyze other possible systematic effects.

### 8.1 Ice Properties and Photon Propagation

A correct simulation of the light propagation in the Antarctic glacier is far from being a trivial task, since the ice contains dust layers flown by the wind from the coast. The problem of air bubbles is less relevant, because, although the upper ice layers are contaminated with bubbles, at the depth

of the AMANDA detector the bubbles disappear under the pressure of the ice cap.

### 8.1.1 Photon-Propagation Simulation

The detector simulation program AMASIM, discussed in Chapter 5, uses pre-computed tables which contain the probability density functions for each Optical Module to detect a photon emitted at a given distance.

The simulations performed in this analysis use the PTD tables [Kar98] which were obtained employing the Muon Absorption Model (MAM) as model for the ice [H<sup>+</sup>b]. The more precise MILLENNIUM [A<sup>+</sup>06b] ice model has been used for the creation of the PHOTONICS set of tables [L<sup>+</sup>]. However, the full detector simulation with the latter is very cpu-time consuming, roughly speaking twice the one performed with the PTD tables. In addition, the results obtained through the PHOTONICS tables have not been thoroughly tested. Therefore, we employed the PHOTONICS tables just in order to estimate the effect of different simulation programs on our analysis and evaluate the systematic uncertainty. The new AHA ice model has been developed in 2007, employing results of dust-logger measurements performed during the deployment of the IceCube strings. We used the AHA-based PHOTONICS set of tables [PHO] to have a better understanding of the systematic error of our analysis due to the ice description.

The simulation of the photon propagation by PTD and PHOTONICS determines:

- $p$ , the probability density function for the arrival time of detected photons;
- $\mu_\gamma$ , the mean value of the Poisson distribution for the number of expected photons per meter of track length.

These two variables can be computed as functions of the following parameters:

- the zenith angle of the track,  $\theta$ ;
- the vertical coordinate of the Optical Module,  $z_{OM}$ ;
- the coordinates of the Optical Module in a plane perpendicular to the track direction,  $\rho$  and  $\phi$ ;
- $L$ , the distance from the track origin at which this plane intersects the particle trajectory;



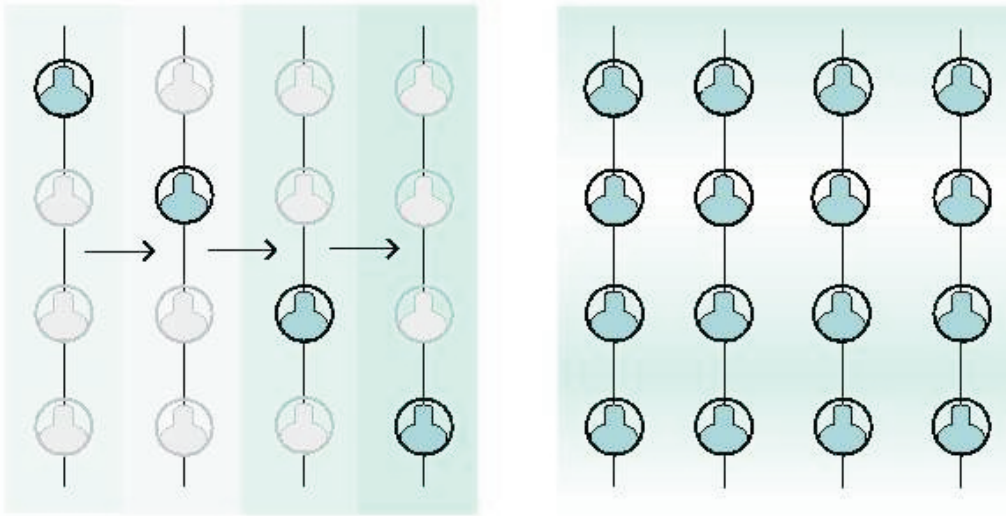


Figure 8.1: The difference between the ice modeling concepts of PTD and PHOTONICS is shown. In PTD (left plot) each Optical Module has its own ice properties and the photon detected by each individual module is assumed to propagate through an ideal isotropic ice with the same properties of the detecting module. In PHOTONICS (right plot), the correct anisotropic ice properties are taken into account.

- $t_{res}$ , the difference between the actual and the arrival time, expected from light propagation without scattering (see Section 4.4).

## PTD

The PTD program was developed in [Kar98] to pre-calculate the probability density function for the arrival time of the photons detected by the AMANDA Optical Modules. The photon-propagation description is simplified and  $p$  and  $\mu_\gamma$  are two-dimensional functions.

Note that PTD relies on a series of simplifications. First of all, the Cherenkov light has a certain wave-length spectrum; however, PTD assumes a mean value of 420 nm for simulating the photon propagation. In addition, in PDT each Optical Module is surrounded by ice with constant ice properties. This is a rough assumption because, as it was mentioned above and illustrated in Figure 8.1, the ice cap at the South Pole is not homogeneous. In the standard PTD ice model, MAM, four classes of ice with different absorption and scattering properties are defined.

The simplified description of the real ice properties leads to discrepancies between data and Monte Carlo, some of which will be later shown in this

chapter. The errors due to the simplified model description were partly compensated using effective ice properties instead of real ones. In MAM, the scattering and absorption coefficients for each of the four ice classes are fitted in order to provide the highest-possible accuracy in the description of the arrival-time delay of events triggered by cosmic-ray induced muons [H<sup>+</sup>b].

## PHOTONICS

The PHOTONICS program [L<sup>+</sup>] is more elaborated than PTD. First of all, the simulation of photons in PHOTONICS is performed for the full Cherenkov spectrum. Moreover, the coefficients for absorption and scattering in the ice were taken from the measurements of in-situ light sources. In addition, the simulation takes into account the quantum efficiency of the Photo-Multiplier Tube and the optical properties of the gel and glass of each Optical Module. Finally, at variance with PTD,  $p$  and  $\mu_\gamma$  are six-dimensional functions; as a result, the tables are less compact than those produced by PTD.

The calculation of  $p$  and  $\mu_\gamma$  leads to a better agreement between Monte Carlo and experiment. However, the resulting PHOTONICS tables reach sizes of several tenths of GigaBytes and slow down the simulation process. As mentioned in the beginning of this chapter, for this reason the PTD program was used for the full simulation of our analysis. Recently, the results of PHOTONICS were tested and declared trustworthy for the muon channel [Ack06, Lan05]. In our work, we will show that they can be considered reliable also for a cascade analysis.

### 8.1.2 PTD and PHOTONICS Comparison

In order to understand the difference between the PHOTONICS and PTD reconstructions, signal Monte Carlo samples were produced with both tables. The PTD tables were employed for the full 2000-2004 simulation. Due to the large PHOTONICS processing time and to the fact that the new detector calibration constants were available only for year 2003, all comparisons presented here were done only for this year. We compare simulations relying on PTD tables generated with the MAM ice model and on PHOTONICS tables generated with both MILLENNIUM and AHA models. In the following, we will denote as PHOTONICS<sub>M</sub> (PHOTONICS<sub>A</sub>) the simulations performed with the MILLENNIUM- (AHA-) based PHOTONICS tables. A detailed comparison of these Monte Carlo samples can be found in Appendix B.

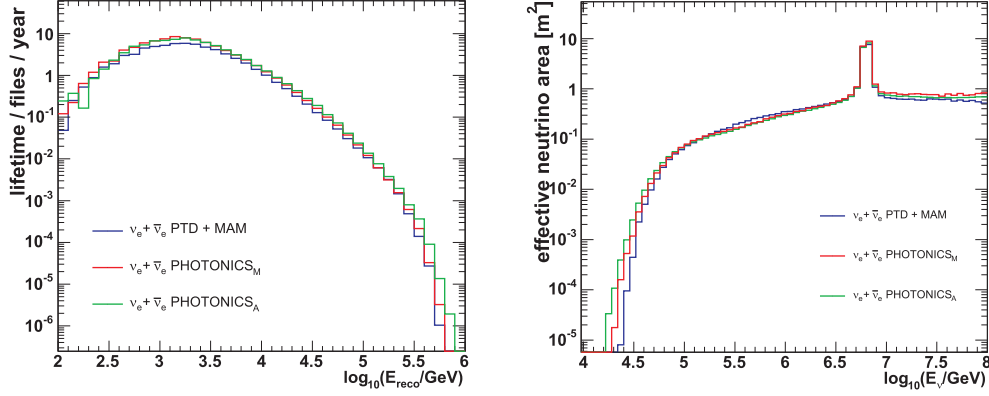


Figure 8.2: Left: a comparison of the reconstructed cascade energy for the PTD, PHOTONICS<sub>M</sub> and PHOTONICS<sub>A</sub> signal Monte Carlo samples. Right: the  $(\nu_e + \bar{\nu}_e)$  effective area. For both distributions, the shown events passed all analysis cuts.

For the signal events which passed all quality cuts of this analysis the reconstructed cascade energy is shown in Figure 8.2 on the left. The difference between the reconstructed energy spectra is visible for the high-energy region. In the right plot we show the distributions of the  $(\nu_e + \bar{\nu}_e)$  effective area. There is only a slight difference between the PTD and PHOTONICS spectra for high energies. This discrepancy is probably caused by the different description of the dust layers in the ice implemented in these samples. Comparing the final efficiency of this analysis for these three Monte Carlo samples, the variations do not exceed several percents (see Table 8.1). In order to estimate the effect of the ice model simulation on atmospheric muon background, one has to compare the results of the analysis using background sam-

	PHOTONICS <sub>M</sub>	PHOTONICS <sub>A</sub>
$E^{-2}$ signal $(\nu_e + \bar{\nu}_e)$	102%	101%
Atmospheric $\nu_e$	119%	138%
Atmospheric $\nu_\mu$	118%	129%
Atmospheric $\mu$	118%	121%

Table 8.1: Summary of  $E^{-2}$   $(\nu_e + \bar{\nu}_e)$  signal expectations, expected rates from atmospheric  $\nu_e$  and  $\nu_\mu$  and atmospheric muons for Monte Carlo samples produced with PHOTONICS<sub>M</sub> and PHOTONICS<sub>A</sub>. All numbers are shown as percentage of the rates obtained using PTD simulations.

ples produced with the various ice models (MAM, MILLENNIUM, AHA). As explained in Chapter 5, the simulation of the muon background is a very cpu-time consuming task. For this reason, we simulated two additional samples of background Monte Carlo with PHOTONICS<sub>M</sub> and PHOTONICS<sub>A</sub>, corresponding to a limited number of days of the detector lifetime. However, one can perform the usual vertex and energy reconstruction for these samples. Scaling the distributions for the reconstructed energy to the total lifetime of the analysis, one can compare then the normalization constants in order to estimate the systematic effect due to the ice description. Table 8.1 summarizes all results for the  $E^{-2}$  signal electron neutrino expectations obtained with PHOTONICS<sub>M</sub> and PHOTONICS<sub>A</sub>. In addition, the expectations for atmospheric electron and muon neutrino as well as the atmospheric muon predictions from both PHOTONICS samples are presented. All numbers are shown as percentage of the number of events obtained with the PTD Monte Carlo sample.

## 8.2 Photo-Multiplier Efficiency

The total light-collection efficiency of the Optical Modules (OMs) includes the quantum efficiency of the Photo-Multiplier Tube and the transmissivity of the optical gel and the glass sphere of each module. The information about the quantum efficiency of each Photo-Multiplier Tube used by the AMANDA detector has been provided by the manufacturer of the PMTs (Hamamatsu).

The laboratory measurements of the AMANDA glass and gel transmissivity are described in [Sud]. Note that the optical gel used for the IceCube Digital OMs is the same one as the gel used for the AMANDA modules. The measurements of the gel transparency for different cycles of the IceCube module production show similar results [Voi]. Variations up to about 10 % were observed using 10-mm thick gel samples. However, the thickness of the gel in each OM is larger, a fact which results in a larger uncertainty [Sud]. The variations due to the Photo-Multiplier quantum efficiency and glass transparency can be safely neglected. In addition, the measurements performed under laboratory conditions are different from those performed at the South Pole ice glacier, where temperatures reach about  $-45^{\circ}$  C. Earlier measurements performed using an in-situ calibration equipment and cosmic-ray induced muons estimated an uncertainty of the efficiency of the OMs to be about  $\pm 30\%$ .

A later analysis was performed in [Lan05], where fluctuations of the individual OM sensitivity were studied with respect to their average. In order to perform these studies, a selection of well-reconstructed downward -going

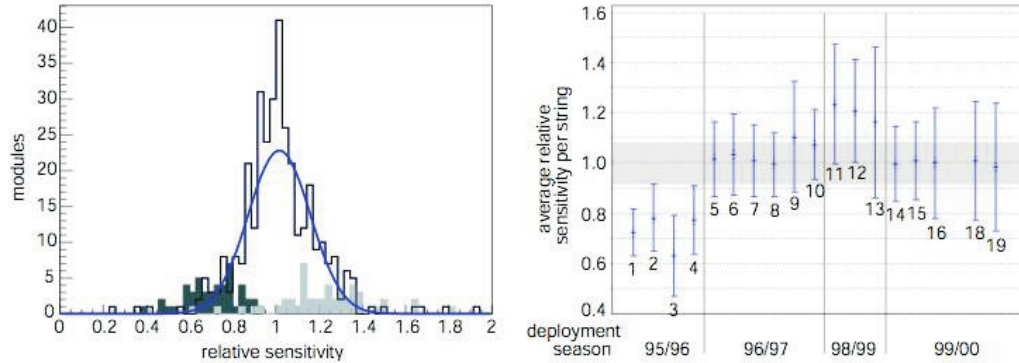


Figure 8.3: Left: photon collection efficiencies of Optical Modules normalized to the average efficiency for 2001 data. Right: average sensitivity for each string. Pictures are adapted from [Lan05].

muons of year 2001 has been used and variations of about 11 % between the modules were obtained. Figure 8.3 (left) shows the efficiencies of individual OMs divided by the average efficiency. Three distributions can be recognized: the central peak in the gaussian distribution corresponds to strings 5-10 and 14-19; strings 1-4, related to the light-blue distribution, have a lower sensitivity; strings 11-13 (the dark-blue distribution), have a higher sensitivity. On the right of Figure 8.3, the average sensitivity of the OM for each string is shown together with the standard deviation.

Later, these studies were repeated for the data collected in 2003 [Wal]. On the left plot of figure 8.4 one can see the photon collection efficiency of Optical Modules normalized to the average efficiency for 2003 data. The right plot shows the distribution of the difference between the relative OM sensitivity from 2001 and 2003 for each OM. In general, the sensitivity does not change substantially. Strings 1-4 show the largest deviation of about 10%. The sigma obtained from the Gaussian fit to the distribution in the left plot of Figure 8.4 gives a dispersion of about 15%. The sigma obtained from the same distribution of the signal Monte Carlo data is 8%. This results in a variation of the OM sensitivity for year 2003 of about 13%. We conservatively assume a 13% systematic error for the OM sensitivity, corresponding to the worst value found for the different year-wise data sub-samples analyzed here.

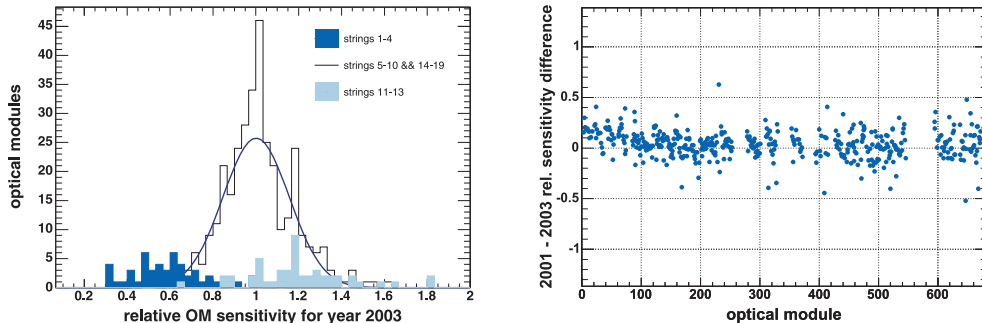


Figure 8.4: Left: photon collection efficiencies of Optical Modules normalized to the average efficiency for 2003 data. Right: difference between the photon collection efficiency of the Optical Modules obtained from the data collected in years 2001 and 2003.

## 8.3 Other Possible Systematic Effects

### Cut efficiencies

In Chapter 7 we described the reconstruction steps and the selection criteria of our analysis. The passing rates of experimental data and the muon background prediction are different for each quality cut, and they are usually higher for the experiment. The reconstruction of real and simulated events after the trigger level is identical. However, the simulated events could miss some features which affect the real data at an earlier level. The first typical example is the electronic cross-talk of the AMANDA detector, described in Section 6.1. The cross-talk filter has been applied to the Monte Carlo background events; however, the effect itself was not simulated. In addition, the short time effects, like variations of the Optical Module noise rates, could lead to an insufficient simulation of the detector response.

In order to estimate this effect we introduce the following procedure. The passing rates for the experimental data and muon background, after all cuts apart the last two, are  $3.3 \cdot 10^{-6}$  and  $2.1 \cdot 10^{-6}$ . This difference could be possibly due to the insufficient detector response and/or ice properties simulation. The cut on the discriminating parameter  $Q_s$  has been lowered for the Monte Carlo sample down to  $Q_s > 0.83$  in order to get approximately the same fraction of events passing this cut as for experimental data. Next, the background distribution has been normalized to the data corresponding to the total lifetime of 1001 days, as described in Chapter 7. The number of background events obtained above the final energy cut ( $\log_{10}(E_{reco}) > 4.65$ ) is 7.3 events, which is about 12% more with respect to the result described

in Chapter 7.

### Year-wise variations

This analysis is performed using 5 years of the AMANDA data collected between 2000 and 2004. The expected flux of astrophysical neutrinos, as well as atmospheric neutrinos and muons, is not different from year to year. However, the detector configuration is not the same for the various time periods. In Section 6.1 we described how the selection of the operating OMs is different for each year. Several other parameters, as the trigger time window and the detector calibration constants, are also year-wise selected. The overall effect results in a slightly-different yearly reconstruction efficiency for the experimental data. We estimated the event passing rates for every year of the analyzed data sample, with relaxed final cut on the discriminating parameter ( $Q_s > 0.7$ ), in order to get sufficient statistics for each year. The same selection was performed on the muon background events, optimized for high energies ( $\log_{10}(E_{reco}) > 3.5$ ). The variations of the passing rates from the mean value for experimental data for each year were compared with variations from Monte Carlo expectations. On average, the deviation of event rates does not exceed 16%.

### Limited statistics

Only the muon background simulation suffers from the problem of limited statistics. In order to estimate this effect, we consider two data sets: experimental data and simulated muon background after all cuts of the analysis apart the last two. In addition, the cut on the reconstructed cascade energy has been applied at  $\log_{10}(E_{reco}) > 3.5$  in order to use the background Monte Carlo adjusted for these energies in addition to the regular one. Here, we introduce the effective lifetime of the Monte Carlo sample. It is based on the available statistics of experimental data and Monte Carlo events which passed the selection described above, and it is  $N_{lifel} = N_{MC}/N_{dat} = 2.5$  larger than that of the experiment. The number of atmospheric muon events which passed all cuts is 16. This corresponds to an expectation of 6.42 background events for the full data sample after re-scaling by a factor of  $1/N_{lifel}$ . As a next step, we evaluate the statistical uncertainty for this number using the upper and lower bound for the 68.2% C.L. obtained from [FC98], since it is well suited for the small signals. Re-scaling all numbers by a factor of  $1/N_{lifel}$ , we obtain the following number for the estimate of the muon background uncertainty from the limited statistics:  $N_{\mu^{atm}} = 6.42_{-24\%}^{+28\%}$ .

### Theoretical uncertainties

The uncertainties from the theoretical predictions affect this analysis in several ways. As we have shown in Section 3.1, the prediction for the neutrino cross section is rather uncertain especially for high energies. In order to estimate the uncertainties related to the cross-section data, the comparison of different cross-section calculations has been performed in [GQRS96]. They compare the results obtained with different extrapolations of the structure functions for energies up to  $10^{21}$  eV. The variations obtained for the energy range of our interest ( $< 10^8$ ) are less than 5%.

The muon background simulation for our analysis is affected by the uncertainties in the predictions for the flux and the composition of the primary cosmic-ray spectra. The detailed studies of the cosmic-ray energy spectrum measured for different elements by various experiments are described in [Hör03]. The uncertainty in the slope of the primary cosmic-ray spectrum has been evaluated to be  $\Delta\gamma = 0.02$  for protons and helium nuclei. For other nuclei contributing to the spectrum, the error is larger mainly due to the limited statistics. To generate atmospheric muon background we used the CORSIKA air shower generator [HST<sup>+</sup>] with the SYBILL 2.1 [EGSL99] model for high-energy interactions. It currently shows the best agreement with the results of various direct and indirect measurements. Re-weighting the events with a factor  $\propto E_{primary}^{\pm\Delta\gamma}$ , we estimate the change in the spectral slope to be less than 5%. The uncertainty due to the variation of the chemical composition are even smaller.

In addition, one has to take into account the uncertainties from the muon propagation in the dense medium. The impact of this effect for atmospheric muons has been presented in [BSK] and has been estimated to be less than 3%.

The uncertainty in theoretical predictions for the primary atmospheric neutrino flux has been estimated in [GH02]. They estimated the uncertainty of the conventional atmospheric neutrino flux predictions to be less than 20%.

#### 8.3.1 Summary of systematic uncertainties

In this section we evaluated the possible systematic effects which could bias the result of our analysis. For the hypothetical neutrino signal, as well as for the atmospheric-neutrino expectation, the systematic error is symmetric. In case of atmospheric muon background, instead, the upper and lower bounds for the systematic uncertainty estimate must be calculated separately. For the expected signal we measured  $N_{sig} = 20.10 \pm 2.9$  events; the expectations



---

for the atmospheric electron and muon neutrino are  $N_{\nu_e^{atm}} = 0.016 \pm 0.006$  and  $N_{\nu_\mu^{atm}} = 0.065 \pm 0.023$ . The muon background expectation, including all systematic effects, is  $N_{\mu^{atm}} = 6.42_{-2.38}^{+2.50}$ . Adding upper and lower error bounds in quadrature, the total number of expected background is  $6.50_{-2.38}^{+2.50}$  events.



# Chapter 9

## Results

In this chapter we discuss the results of the search for neutrino-induced cascades performed in this thesis. The final energy spectra for the experimental data and the MC simulation, as well as the characteristics of the events which passed the final selection, are presented in Section 9.1. In Section 9.2 and Section 9.3 we describe the resulting capabilities of the AMANDA detector to detect the astrophysical neutrino flux by showing our results for the neutrino effective volume and effective area. Finally, the resulting limits on the neutrino flux are discussed in Section 9.4.

### 9.1 Final Sample

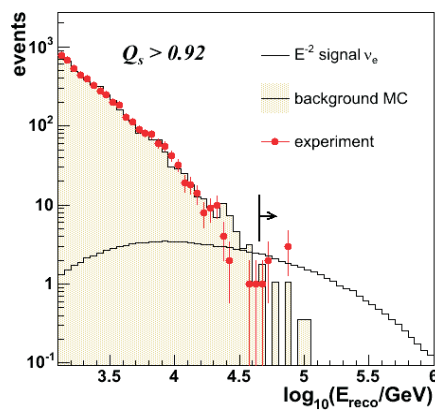


Figure 9.1: Reconstructed cascade energy distributions for experimental data,  $E^{-2}$  ( $\nu_e + \bar{\nu}_e$ ) signal and background Monte Carlo.

Event #	1	2	3	4	5	6
<i>Year</i>	2002	2002	2002	2002	2003	2004
<i>GPS day</i>	179	181	273	285	129	56
$V_x$ , m	14.62	19.08	84.92	1.19	26.59	51.9
$V_y$ , m	111.64	103.72	7.89	125.36	-87.65	101.3
$V_z$ , m	-95.64	-102.52	-48.12	-102.99	-126.70	-108.10
$L_{vertex}$	6.521	6.360	6.215	6.588	6.818	6.550
$\log_{10} E_{reco}$ , GeV	4.884	4.672	4.895	4.725	4.728	4.867
$L_{energy}$	0.663	0.591	0.586	0.772	1.089	0.596
$N_{early}/N_{hits}$	0.0231	0.0083	0.0001	0.0258	0.0070	0.0041
$N_{direct}$	23	16	29	30	16	62
$N_{hits}$	520	485	497	388	282	478
$N_{ch}$	227	208	267	188	175	208
$Q_s$	0.948	0.986	0.988	0.951	1.00	0.939

Table 9.1: The observables and the reconstructed quantities of the six experimental events which passed all analysis cuts.

The final reconstructed cascade energy spectrum for 5 years of experimental data, corresponding to 1001 days of the detector up-time, is shown in Figure 9.1 together with the expected  $E^{-2}$  ( $\nu_e + \bar{\nu}_e$ ) signal and the background Monte Carlo. The events shown here have passed all the cuts of the analysis except the cut on the reconstructed cascade energy, which was obtained from the optimization procedure. This cut,  $\log_{10} E_{reco} > 4.65$ , is indicated as an arrow. There are six experimental events passing this cut.

These cascade-like events are illustrated in Appendix A. The observable quantities for these six events are summarized in Table 9.1. The parameters which were used for the data selection and characterize the quality of the remaining events are also listed. The vertices for these events are mainly reconstructed in the lower part of the detector. This can be understood looking at the reconstructed event distribution as a function of the detector depths (see Chapter 8). Due to the dust layers in the antarctic ice cap, the reconstructed vertex positions are concentrated in three layers. The six events are mainly concentrated in the lowest one.

The expected number of background events is 6.50, which is consistent with the number of observed events. The background for this analysis consists of two sources: the atmospheric muon background and the background induced by neutrinos produced in the atmosphere. The event rate for muon neutrinos produced in the atmosphere is higher than that for electron neutrinos (see Section 2.2). Even the higher selection efficiency for  $\nu_e$  will not

change this fact. The expected numbers of muon and electron neutrinos are 0.065 and 0.016 events respectively. Taking into account the systematic error, studied in detail in Chapter 8, the final rates for experimental data and expected background from atmospheric muons and neutrinos are shown in Table 9.2.

Taking into account systematic errors from atmospheric muon, as well as muon and electron neutrinos, the total background for this analysis is  $6.50^{+2.50}_{-2.38}$  events.

experiment	atmospheric $\mu$	atmospheric $\nu_e$	atmospheric $\nu_\mu$
6	$6.42^{+2.50}_{-2.38}$	$0.016 \pm 0.006$	$0.065 \pm 0.023$

Table 9.2: The event rates for experiment and expected background from atmospheric muons, electron and muon neutrinos including the systematic uncertainties.

## 9.2 Detector Effective Volume

In order to calculate the effective volume of the AMANDA detector, sensitive to high-energy neutrino-induced cascades, we use the signal MC sample obtained after the application of all analysis cuts. The simulated neutrino sample corresponds to the total lifetime of the experimental data set used for this analysis. The effective volume,  $V_{eff}$ , can be defined as:

$$V_{eff} = \lim_{V_{gen} \rightarrow \infty} \lim_{N_{gen} \rightarrow \infty} \frac{N_{final}}{N_{gen}} V_{gen}, \quad (9.1)$$

where  $N_{final}$  is the number of signal events recorded with the detector which passed all cuts on  $N_{dir}^{200}$ ,  $N_{early}/N_{hits}$ ,  $L_{vertex}$ ,  $L_{energy}$ ,  $\rho_{xy}$ ,  $Q_s$ , and  $E_{reco}$ ;  $N_{gen}$  is the number of particles generated in a volume  $V_{gen}$ . Note that, in general,  $V_{eff}$  is a function of the neutrino energy and the zenith angle; moreover, it depends on the neutrino flavor. In Figure 9.2 the effective volume is shown as a function of the neutrino energy for each neutrino flavor. The effective volumes presented here are averaged over the zenith angles from  $0^\circ$  to  $180^\circ$ . For each flavor the distribution has a cut-off at around 30 TeV, as a result of the final cut on the reconstructed cascade energy. As one can see, the distributions for the three neutrino flavors are different.

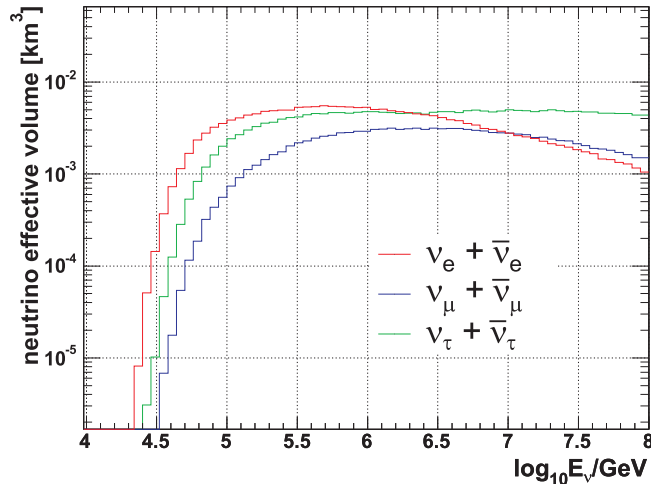


Figure 9.2: Effective volume for  $\nu_e, \nu_\mu$  and  $\nu_\tau$  as a function of the neutrino energy.

The effective volume for  $(\nu_e + \bar{\nu}_e)$  increases for lower values of the energy, has a maximum between 100 TeV and 1 PeV, reaching a volume of about  $6 \cdot 10^{-3} \text{km}^3$ , and then slowly decreases with rising energy. The reduction effect follows mainly the neutrino absorption in the Earth. Furthermore, in Section 6.4, we showed how the energy resolution for higher energies is worse than for lower ones. This contributes also to the reduction of the effective volume for higher energies.

For  $(\nu_\mu + \bar{\nu}_\mu)$ , the visible energy is typically smaller than the one for  $(\nu_e + \bar{\nu}_e)$  and  $(\nu_\tau + \bar{\nu}_\tau)$  at low energies. Because of this, the effective volume for this flavor is smaller. In addition, in the case of a charged-current interaction, the muon can be mis-identified as an atmospheric muon and rejected from the sample, a fact which reduces the efficiency. The declination of the spectrum for high energies is due to the same reasons mentioned above for  $\nu_e$ .

The effective volume for tau neutrinos has a different energy dependence compared to  $\nu_e$  and  $\nu_\mu$ , since different processes affect the neutrino during the propagation through the Earth. Instead of being absorbed, tau neutrinos regenerate at lower energies (see Section 3.1). The effective volume for the  $(\nu_\tau + \bar{\nu}_\tau)$  flux grows up to  $5 \cdot 10^{-3} \text{km}^3$  at about 500 TeV and remains constant up to higher energies due to this regeneration effect and partly to contributions from double-bang events, described in Section 3.1. For an energy of about 2 PeV, the distance between the  $\nu_\tau$  interaction vertex and a  $\tau$ -lepton decay is close to 100 m and increases by an amount of about 50 m per PeV [C<sup>+</sup>07]. For energies of several PeV both bangs still may occur in

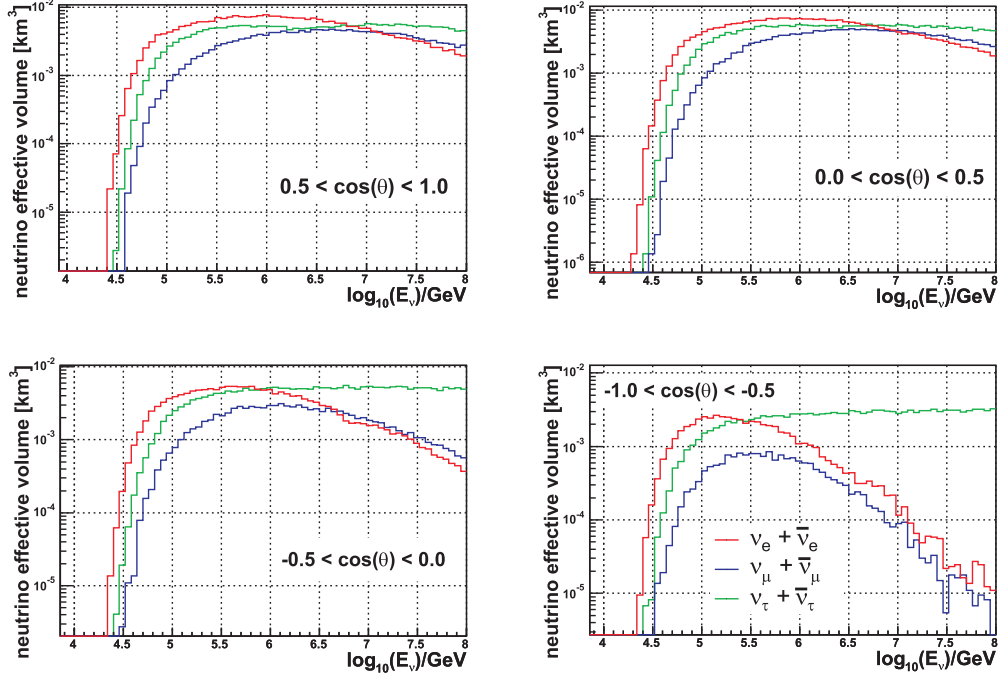


Figure 9.3: Effective volume for  $\nu_e$ ,  $\nu_\mu$  and  $\nu_\tau$  as a function of the neutrino energy and the zenith angle. The two upper plots show the effective volume for neutrinos coming from the southern hemisphere and the plots below correspond to events from the northern hemisphere which propagated through the Earth.

the detector providing unmistakable double-bang signature; however, due to the geometrical constraints and limited energy range, the expected rates for these events are rather low. For energies above  $\sim 10$  PeV, the AMANDA detector is not capable to distinguish double-bang signature from a regular cascade. At these energies, the probability to detect a cascade from either a vertex or a decay of such events increases by at most a factor of two.

The effect of the neutrino absorption during the propagation through the Earth is well illustrated in Figure 9.3. Here the effective volume at the final analysis level for  $\nu_e$ ,  $\nu_\tau$  and  $\nu_\mu$  is shown for four different bins of the zenith angle. As one can see from these distributions, the neutrino absorption effect becomes significant for neutrinos from the northern hemisphere. For tau neutrinos, the  $V_{eff}$  distribution saturates for high energies due to the tau regeneration effect.

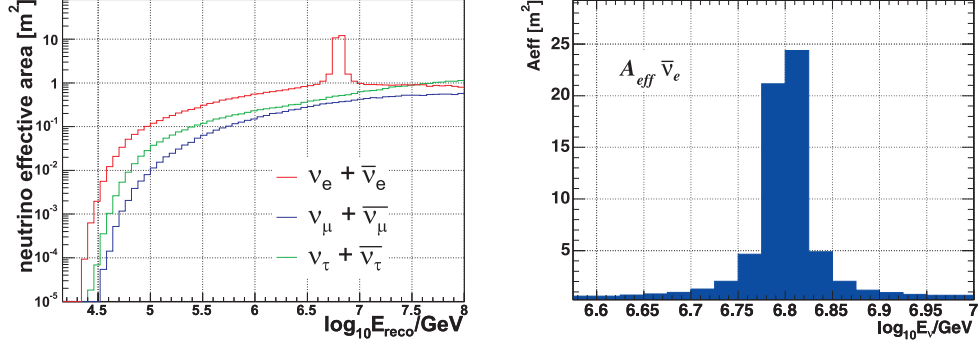


Figure 9.4: Left: the effective neutrino area of the detector as a function of the neutrino energy. Here, distributions for all neutrino (and anti-neutrino) flavors are shown. Right: the effective area for  $\bar{\nu}_e$  in the energy region of the Glashow resonance.

### 9.3 Detector Effective Area

For any given model flux, the effective area of the detector can be used to evaluate the sensitivity of the detector to the given flux prediction. Let us assume an ideal detector, where the detection of all neutrinos with a given flux  $\phi(E_\nu, \theta)$  can be performed with full efficiency. For neutrino generated on the surface of the Earth with an energy  $E_\nu$  and a zenith angle  $\theta$ , the total number of observed events in an ideal detector is:

$$N_{event} = T \int \int \phi(E_\nu, \theta_\nu) A_{eff}(E_\nu, \theta_\nu) dE_\nu d\Omega, \quad (9.2)$$

where  $T$  is the exposure time of the detector and  $A_{eff}$  is the neutrino effective area. Similarly to Eq. (9.1), after averaging over all the neutrino directions, the effective area can be calculated by:

$$A_{eff} = \lim_{A_{gen} \rightarrow \infty} \lim_{N_{gen} \rightarrow \infty} \frac{N_{final}}{N_{gen}} \times A_{gen} \times P_{int}, \quad (9.3)$$

where  $A_{gen}$  is the generation plane.  $V_{gen}$ , the volume where neutrinos were generated for our analysis, has a cylindrical shape. The generation plane is the cross section of the cylinder with a central axis along the direction of the incoming neutrino. The number of generated events,  $N_{gen}$ , and the final number of events,  $N_{final}$ , are the same as in Eq. (9.1). The last factor,  $P_{int}$ , is the probability for a neutrino which passes through the cylindrical volume to interact inside this volume.



The left plot in Figure 9.4 shows the neutrino effective area of the detector calculated for  $(\nu_e + \bar{\nu}_e)$ ,  $(\nu_\mu + \bar{\nu}_\mu)$  and  $(\nu_\tau + \bar{\nu}_\tau)$ . From Eq. (9.3) it follows that the effective area is proportional to the neutrino cross section, being proportional to  $P_{int}$ . For muon and tau neutrinos and antineutrinos the cross section is similar, hence the effective area distributions have similar behavior. For electron antineutrinos, the cross section increases due to the Glashow resonance (see Chapter 3), which results in a peak at around 6.3 PeV in the  $(\nu_e + \bar{\nu}_e)$  distribution. The effective area for  $\bar{\nu}_e$  is shown separately on the right plot of Figure 9.4. Averaging this distribution in an energy range between  $10^{6.7}$  GeV and  $10^{6.9}$  GeV, the effective area due to the resonance is:

$$\bar{A}_{eff}^{\bar{\nu}_e} = \frac{1}{0.2} \int_{6.7}^{6.9} A_{eff}(E_\nu) d \log E_\nu = 7.8 \text{ m}^2. \quad (9.4)$$

In general, the effective area rises with the energy for muon and tau neutrinos for the analyzed energy range,  $50 \text{ TeV} < E_{reco} < 100 \text{ PeV}$ . In the case of electron neutrinos, the distribution grows up to the resonant peak and saturates for higher energies. The neutrino absorption effect is partly compensated by the increase of the neutrino cross section with the energy. For all neutrino flavors, the effective detector area reaches about  $1 \text{ m}^2$  for energies around 100 PeV.

The neutrino effective area for different zenith angle bands is shown in Figure 9.5. As for the effective volume, the absorption effect becomes visible for the effective area at  $\cos \theta < 0$ . In addition, the tau-regeneration effect takes place here. However, it is less pronounced than in case of the effective volume, because for the area the interaction probability is taken into account by means of Eq. (9.3). The regenerated  $\tau$  particles have lower energies, hence the interaction probability is relatively low with respect to the original ones. For  $(\nu_e + \bar{\nu}_e)$  the increase due to the Glashow resonance is not visible for neutrinos coming from below since they are likely to interact during the propagation.

## 9.4 Limits on the Diffuse Flux of Neutrinos

The resulting number of events in the experimental sample after the implementation of all selection criteria is consistent with the expected background from atmospheric muons and neutrinos. Therefore, as a result of this analysis, we place an upper limit on the diffuse flux of astrophysical neutrinos.

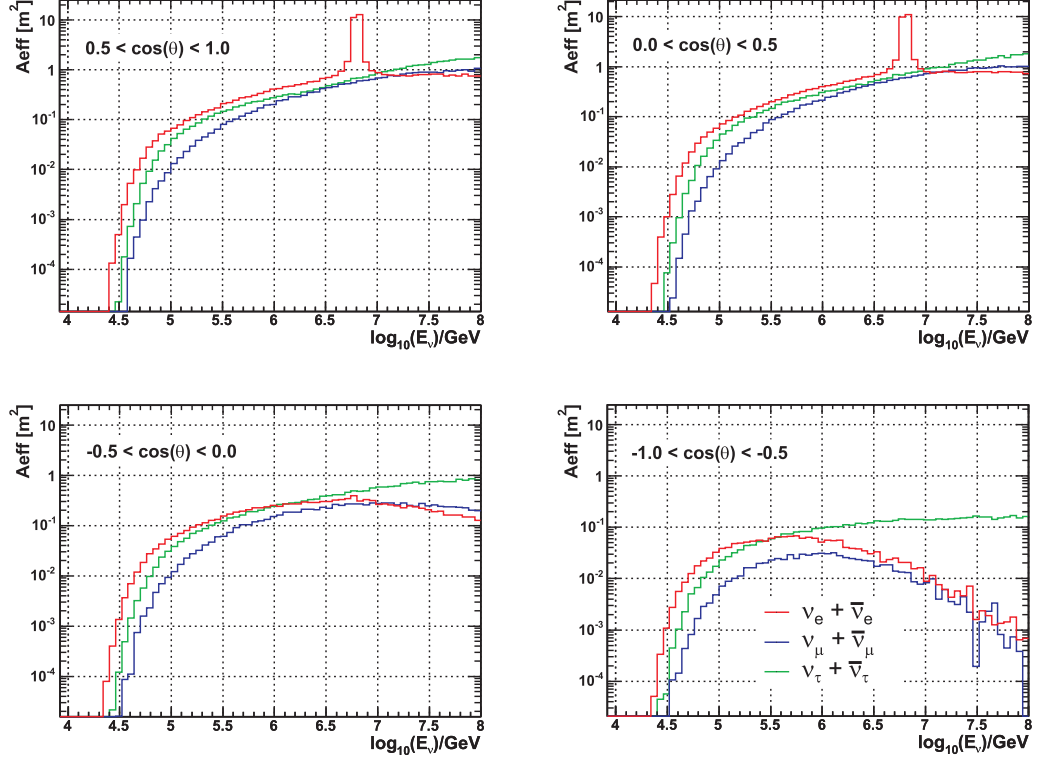


Figure 9.5: The AMANDA detector effective neutrino area is shown as a function of the neutrino energy for four different ranges of the zenith angle. Distributions for electron, muon and tau neutrinos are shown separately. The tau regeneration effect is mainly visible in the two lower plots, which correspond to the up-going neutrinos.

### 9.4.1 Event Upper Limit

The search for the neutrino-induced cascades described in this thesis depends on the comparison of the number of observed events,  $n_{obs} = 6$ , to the total number of events from the background expectation,  $b = 6.50^{+2.50}_{-2.38}$ . We use these numbers to compute the event upper limit; this represents the limit on how many signal events from the hypothetical neutrino source,  $s$ , are compatible with our observation. In order to perform this calculation we follow the method proposed by Feldman and Cousins [FC98] for constructing the unique confidence belt, summing over the probability  $P(n_{obs}|s+b)$ , calculated for all  $n_{obs}$ , to see  $n_{obs}$  events while expecting  $s+b$ . According to [FC98] the event upper limit in this case is  $\mu_{90\%} = 4.99$  at 90% C.L.

However, this number does not include the systematic uncertainties which

are not negligible for the AMANDA data. A "semi-Bayesian" approach was proposed in [C<sup>+</sup>03] to include the systematic errors in the calculation of limits or confidence belts. The idea of this approach is to average the probabilities  $P(n_{obs}|s+b)$  over the allowed range of the systematic uncertainty:

$$\hat{P}(n_{obs}|s, b) = \int_{-\infty}^{\infty} P(n_{obs}, s', b') f_b(b') f_s(s') db' ds', \quad (9.5)$$

where  $f_b(b')$  and  $f_s(s')$  are the probabilities for the background and signal to be  $b$  and  $s$  respectively. We assume a Gaussian distribution for the error on the signal with a sigma equal to the estimated systematic uncertainty  $\pm 14\%$ . For the error on the background we assume also a Gaussian distribution. Since the error for the background is asymmetric, we construct this distribution choosing the peak position in the centre of the error interval. Taking into account these assumptions, the probability densities for background and signal are:

$$f_b(b') = \frac{1}{\sqrt{2\pi}\sigma_b} \exp\left(-\frac{(b' - b_{exp})^2}{2\sigma_b^2}\right), \quad (9.6)$$

$$f_s(s') = \frac{1}{\sqrt{2\pi}\sigma_s} \exp\left(-\frac{(s' - s_{exp})^2}{2\sigma_s^2}\right). \quad (9.7)$$

Here  $b_{exp}$  and  $s_{exp}$  are the expected background and signal and  $\sigma_b$  and  $\sigma_s$  denote the widths of their assumed Gaussian distributions. In order to include the systematic uncertainties in the limit calculation we use the POLE++ software presented in [C<sup>+</sup>03]. This program performs the integration of Eq. 9.5 and returns the corrected event upper limit at any coincidence level from which the flux limit can be derived.

## 9.4.2 Flux Upper limit

One can calculate the expected event rate for every hypothetical neutrino flux prediction,  $N_{event}$ , using the neutrino effective area as in (9.2). A flux upper limit can be derived from the event upper limit,  $\mu_{90\%}$ , using the event expectation derived from a given model:

$$\frac{d\Phi}{dE} = \Phi_0 f(E), \quad (9.8)$$

with a flux strength  $\Phi_0$  and a spectral shape given by  $f(E)$ . The flux upper limit is the normalization constant,  $\Phi_{limit}$ , determined by dividing the event

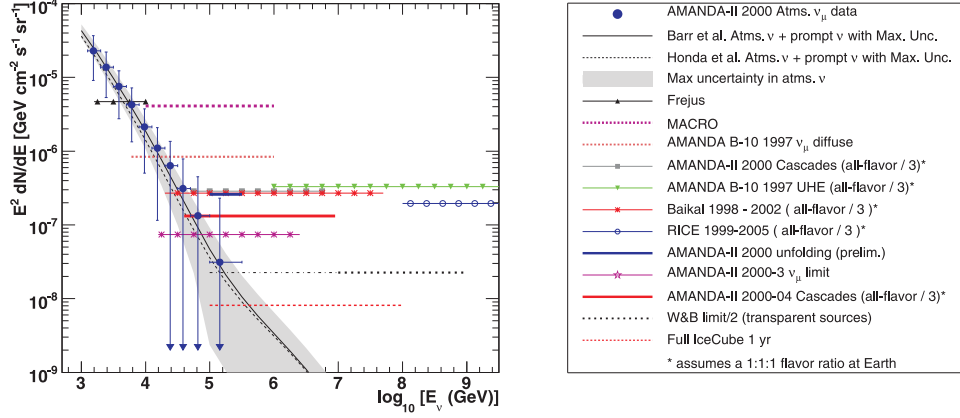


Figure 9.6: The upper limits on a diffuse neutrino flux from sources with an  $E^{-2}$  energy spectrum are shown for muon and all-flavor analysis. All-flavor upper limits were divided by a factor of three, assuming the flavor ratio at the Earth to be  $\phi_{\nu_e+\bar{\nu}_e} : \phi_{\nu_\mu+\bar{\nu}_\mu} : \phi_{\nu_\tau+\bar{\nu}_\tau} \approx 1 : 1 : 1$ .

upper limit with the expected number of events,  $N_{event}$ :

$$\frac{d\Phi^{limit}}{dE} = \frac{\mu_{90\%}}{N_{event}} f(E). \quad (9.9)$$

According to expectations from first-order Fermi acceleration, the signal spectrum for astrophysical neutrinos is proportional to  $E^{-2}$ . Results for this energy spectrum, as well as other theoretical predictions, are presented further in this Chapter.

### Results for $E^{-2}$ spectrum

Here we consider a signal hypothesis consisting of a flux

$$E^2\Phi_0 = 1.0 \times 10^{-6} (E/GeV)^{-2} / (GeV \text{ s sr cm}^2).$$

For this signal strength we expect 6.96  $\nu_e$ , 2.32  $\nu_\mu$  and 3.99  $\nu_\tau$  signal events at the final analysis level. According to this event expectation we can calculate the flux limit using Eq. (9.9). Including all systematic uncertainties, the event upper limit obtained in this analysis is  $\mu_{90\%} = 5.28$ . This leads to the upper limit on the diffuse all-flavor neutrino flux at the Earth at 90% C.L.:

$$E^2\Phi_{90\%CL} = 3.96 \cdot 10^{-7} GeV \text{ s}^{-1} \text{ sr}^{-1} \text{ cm}^{-2}. \quad (9.10)$$

In order to define the energy range where the limit has to be placed, we used the simulated true neutrino energy. The range in this distribution defined by the central 90% of the signal with a reconstructed cascade energy  $\log_{10}(E_{reco}) > 4.65$  is the energy range where the limit is placed. In our analysis this interval extends from 40 TeV to 9 PeV.

In Figure 9.6 this limit is shown together with the results obtained by other experiments. The upper limits on the  $(\nu_\mu + \bar{\nu}_\mu)$  flux placed by Frejus [R<sup>+</sup>96], MACRO [A<sup>+</sup>03b] and AMANDA-B10 [A<sup>+</sup>03a] are illustrated here, as well as the unfolded atmospheric spectrum from 2000 AMANDA-II data [A<sup>+</sup>05a]. In addition to the result of this analysis several other all-flavor neutrino upper limits are shown here. The limit obtained with five years of BAIKAL data [A<sup>+</sup>06d], the RICE [K<sup>+</sup>06] six-year upper limit, the upper limit on UHE neutrino flux obtained with AMANDA-B10 data [A<sup>+</sup>05b] and the cascade analysis derived using one year of the AMANDA-II data [A<sup>+</sup>04a] are presented. Note that for consistency all results from the all-flavor neutrino flux were adjusted for a single-limit plot, assuming 1:1:1 flavor ratio at the Earth. As one can see here, the result of this analysis provides the most sensitive limit existing at the moment on a diffuse all-flavor astrophysical neutrino flux with  $E^{-2}$  energy spectrum.

### Results for other energy spectra

Using this data set, we tested various models which predict the flux of high-energy neutrinos with energy spectra different from  $\Phi \propto E^{-2}$ . For each model, the number of events expected from this analysis,  $N_{model}$ , has been calculated following Eq. (9.2). The meaningful variable which quantifies the sensitivity for a model flux is the Model Rejection Factor,  $MRF = \mu_{90\%} / N_{model}$ . If the number of signal events expected from a given model exceeds the event upper limit ( $MRF < 1$ ), this model is ruled out at 90% C.L. To place a limit on a given neutrino flux,  $\Phi_{model}(E_\nu)$ , one has to re-scale the signal strength assumed for this flux to  $MRF \times \Phi_{model}(E_\nu)$ . The flux of neutrinos is ruled out at 90% C.L. if  $MRF < 1$ , i.e. the placed limit violates the theoretical prediction.

Here the effect of the neutrino oscillations becomes important. Most models predict a flux ratio of  $\phi_{\nu_e + \bar{\nu}_e} : \phi_{\nu_\mu + \bar{\nu}_\mu} : \phi_{\nu_\tau + \bar{\nu}_\tau} \approx 1 : 2 : 0$  at the source which transfers to a  $\phi_{\nu_e + \bar{\nu}_e} : \phi_{\nu_\mu + \bar{\nu}_\mu} : \phi_{\nu_\tau + \bar{\nu}_\tau} \approx 1 : 1 : 1$  flavor ratio at the Earth due to the oscillation effect. For many models the predictions have been made only for  $\nu_\mu$  and the effects of neutrino oscillations have not been taken into account. For these models we included the corrections for the oscillation effects in the limit calculation.

model	$\nu_e + \bar{\nu}_e$	$\nu_\mu + \bar{\nu}_\mu$	$\nu_\tau + \bar{\nu}_\tau$	all-flavors	MRF
$10^{-6} E^{-2}$	6.96	2.32	3.99	13.3	0.40
SDSS (2005)	1.08	0.37	0.60	2.05	2.58
MPR (AGN jet)	1.07	0.50	0.72	2.50	2.29
MPR ( $\tau < 1$ )	8.52	7.56	2.77	19.07	0.28
WB GRB	0.025	0.021	0.014	0.059	89.50
Charm D	2.06	0.68	-	2.74	1.92
Naumov RQPM	0.42	0.15	-	0.57	9.24
Martin GBW	0.035	0.012	-	0.047	112.34

Table 9.3: The summary of expected event rates from various astrophysical and atmospheric prompt neutrino models. The assumed event upper limit with all systematic uncertainties is  $\mu_{90\%} = 5.28$ .

In Table 9.3 we summarize the resulting MRF for several astrophysical and atmospheric prompt neutrino models tested with this data set. The MRF has been calculated for the sum of all-flavor events,  $\nu_e + \nu_\mu + \nu_\tau$ , for a given flux.

The first astrophysical neutrino model with the flux spectra different from  $E^{-2}$  is the model initially proposed by Stecker, Done, Salamon and Sommers (SDSS) [SS96] and revised by Stecker in 2005 [Ste05]. This model predicts a neutrino flux from cores of AGNs, especially from Seyfert galaxies. The model rejection factor established for this prediction is MRF=2.58, leading to a flux upper limit of  $2.58 \cdot \Phi_{SDSS}$ . An upper bound for high-energy neutrino flux from AGN jets as well as an upper bound for neutrinos from generic optically thin pion photoproduction sources have been calculated by Mannheim, Protheroe and Rachen (MPR) [MPR00]. These predictions were also tested in this work. The limits on the MPR AGN jet upper bound and the MPR bound for optically thin sources are  $2.29 \cdot \Phi_{MPR(AGN)}$  and  $0.28 \cdot \Phi_{MPR(\tau < 1)}$  correspondingly. Another tested model has been proposed by Waxman and Bahcall [WB97] in 1996 and until now it remains the lowest neutrino flux prediction. In this model neutrinos are assumed to be produced in Gamma Ray Bursts. Even after 5 years of operation the AMANDA detector sensitivity is still too small to make a meaningful conclusion about this model. The obtained model rejection factor for this prediction is MRF=89.50, and the corresponding flux upper limit is  $89.50 \cdot \Phi_{WBGRB}$ . All astrophysical models listed here are shown in Figure 9.7 on the left. The horizontal line represents the single flavor upper limit for an energy spectrum falling as  $E^{-2}$  obtained by this analysis:

$$E^2 \Phi_{90\%CL} = 1.32 \cdot 10^{-7} \text{GeV s}^{-1} \text{sr}^{-1} \text{cm}^{-2}.$$

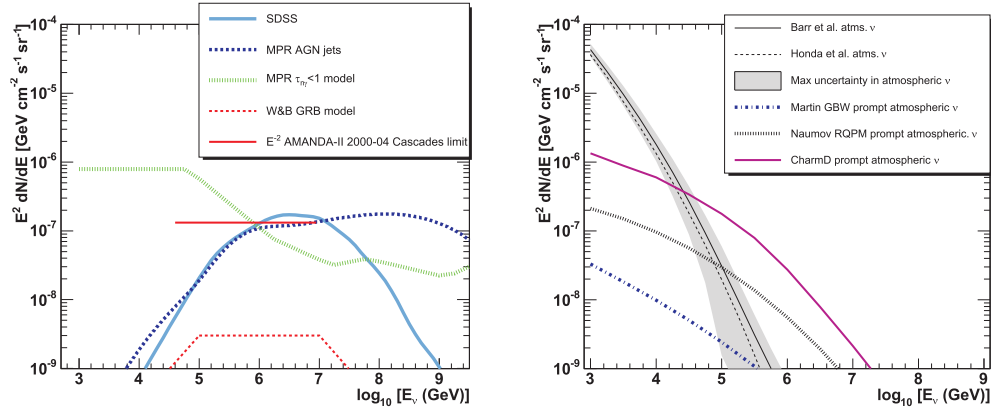


Figure 9.7: Flux prediction for several models of astrophysical neutrino sources (left) and atmospheric neutrinos due to charm production (right).

In addition to astrophysical models, three models for atmospheric neutrinos from prompt charm production were tested with this data set. The flux spectra for these prompt models are shown in the right plot of Figure 9.7. The upper solid curve corresponds to the prompt neutrino model proposed by Zas, Halzen and Vazquez [ZHV93] (Charm D). This prediction is based on a non-perturbative cross-section model [VFGS87]. The event expectation for this model leads to  $\text{MRF}=1.92$ . The second prompt atmospheric neutrino model tested here is the Naumov RQPM model [BNSZ89, Fio01]. This non-perturbative model uses the data from primary cosmic rays and hadronic interaction experiments. As one can see in the left plot of Figure 9.7, the prediction for the neutrino flux according to this model is lower than for the Charm D. Thus, the model rejection factor obtained with our data set is  $\text{MRF}=9.24$ .

The last model which was tested (Martin *et al.* [Mar03]) predicts prompt-lepton fluxes based on the Golec, Biernat and Wüsthoff (GBW) model of deep inelastic scattering (DIS) [Gol99]. The production cross section for this model is lower than for the models described above; this fact can be explained by gluon saturation effects included in the model. The sensitivity of our data set is about two orders of magnitude above the predicted flux. The model rejection factor for this model is  $\text{MRF}=112.34$ .

There are other theoretical models which predict the flux of high-energy astrophysical neutrinos and atmospheric neutrinos due to the prompt charm production. Since several models have been already ruled out by analysis with sensitivities worse than the sensitivity we obtained, we do not consider them here. Only the MPR model for optically thin sources ( $\text{MPR}_{(\tau < 1)}$ ) has a

MRF=0.28. This model is excluded at 90% C.L. All other models described above are not ruled out according to the results based on the 2000-2004 AMANDA II data.



# Chapter 10

## Summary

In this dissertation we performed the search for high-energy neutrino-induced cascades using five years of the AMANDA-II data collected in 2000-2004. Isolated electromagnetic or hadronic cascades can be produced by charged-current interactions of high-energy electron or tau neutrinos, as well as by neutral-current interactions of neutrinos of any flavor.

The search is based on the full reconstruction of the position and energy of the resulting events. The precise reconstruction has been performed using likelihood techniques on the pre-selected event sample. The pre-selection was performed using the cascade filter based on the Sieglinde [Sie] reconstruction program developed by the AMANDA group. The final quality cuts have been optimized using the all-neutrino-flavor signal Monte Carlo and atmospheric muon background simulations.

After all analysis selections there are six remaining events in the 5-year AMANDA-II data sample, while  $6.50_{-2.38}^{+2.50}$  background events from atmospheric muons and neutrinos were expected. The number of the observed events is consistent with the background expectation; therefore, we place the upper limit on the expected signal of astrophysical neutrinos.

The systematic uncertainties for the neutrino signal have been estimated to be 14% and they have been incorporated into the final neutrino limit calculation. Assuming a flavor ratio 1:1:1 at the detector site and an  $E^{-2}$  differential spectrum, the upper limit on the diffuse all-flavor neutrino flux at the 90% C.L. is:

$$E^2 \Phi_{90\%CL} = 3.96 \cdot 10^{-7} \text{GeV s}^{-1} \text{ sr}^{-1} \text{ cm}^{-2}. \quad (10.1)$$

The energy range where the limit was placed has been defined using the distribution of the simulated true neutrino energy at the final selection level. The upper and lower bounds were defined by the central 90% of the distribution where the energy region extends from 40 TeV to 9 PeV. In addition, we tested

the predictions for the neutrino flux obtained using various astrophysical and atmospheric neutrino models.

# Chapter 11

## Outlook

This analysis has been performed using data from the AMANDA-II detector collected from 2000 to 2004. During the austral summer 2004/2005 the construction of the next-generation neutrino telescope, IceCube, has started. The strings of IceCube surround the AMANDA-II detector. The IceCube detection principles are the same as those of AMANDA. When completed, it will consist of 4800 Digital Optical Modules (DOMs) regularly distributed over 80 strings in a volume of one cubic kilometer. The potential of the cascade channel analysis using IceCube is very promising. First of all, due to the large detection volume, IceCube will be sensitive to neutrinos of all flavors in a large energy range. The classic double-bang signature from  $\nu_\tau$  charged-current interactions should be detectable for energies up to 20 PeV when IceCube will be fully operative.

The current detector configuration is 32 in-ice strings and 80 ice-top tanks deployed on the surface, and even more modules will be deployed this season. The space among the DOMs in IceCube is larger than in the AMANDA configuration: this could result in a worse cascade position reconstruction. However, the cascade reconstruction with the IceCube data can benefit from the usage of a full pulse information from the DOMs, which is not available for the AMANDA data.

In order to achieve a good quality of the detector calibration, two types of in-situ light sources have been deployed in IceCube. Each DOM contains 12 bright LEDs and, in addition, a laser light source (Standard Candle) was mounted on the in-ice string. The light from these calibration sources can be used as an artificial cascade for testing the new reconstruction techniques developed for IceCube. The performance of the IceCube reconstruction is currently very close to the AMANDA one and might be improved by optimization of the reconstruction algorithms.

Another important step, currently under investigation, is the reconstruc-

tion of the cascade direction. The direction reconstruction can be improved taking into account the longitudinal development of cascades. Electromagnetic cascades above 10 PeV have a length of several tens of meters and their signature should be detectable by IceCube.

Although recent multi-year searches for extraterrestrial neutrinos performed with the AMANDA data did not detect any extraterrestrial flux, the limits placed by the current available analysis have already ruled out several theoretical models. In 2011, when the construction of the IceCube detector will be completed, the sensitivity of the full apparatus should allow to test those models which have not been yet ruled out by the current experiments and, hopefully, to detect the flux of astrophysical neutrinos.

# Bibliography

- [A<sup>+</sup>] Abbasi, R.; et al. (the HiRes collaboration): Observation of the GZK cutoff by the HiRes experiment. *astro-ph/0703099*.
- [A<sup>+95</sup>] Ahmed, T.; et al. (the H1 collaboration): A measurement of the proton structure function  $f_2(x, Q^2)$ . In: *Nucl. Phys. B*, volume 439:p. 471, 1995. *hep-ex/9503001*.
- [A<sup>+99</sup>] Apollonio, M.; et al. (the CHOOZ collaboration): Limits on neutrino oscillations from the CHOOZ experiment. In: *Phys. Lett. B*, volume 466:p. 415, 1999. *hep-ex/9907037*.
- [A<sup>+01a</sup>] Achard, P.; et al. (the L3 collaboration): Standard Model Higgs boson with the L3 experiment at LEP. In: *Phys. Lett. B*, volume 517:p. 319, 2001. *hep-ex/0107054*.
- [A<sup>+01b</sup>] Aharonian, F.; et al. (the HEGRA collaboration): The TeV energy spectrum of Mkn 501 measured with the stereoscopic telescope system of HEGRA during 1998 and 1999. In: *Astrophys. J.*, volume 546:p. 898, 2001. *astro-ph/0008211*.
- [A<sup>+02</sup>] Ahmad, Q. R.; et al. (the SNO collaboration): Direct evidence for neutrino flavor transformation from neutral-current interactions in the Sudbury Neutrino Observatory. In: *Phys. Rev. Lett.*, volume 89:p. 011301, 2002. *nucl-ex/0204008*.
- [A<sup>+03a</sup>] Ahrens, J.; et al.: Limits on diffuse fluxes of high energy extraterrestrial neutrinos with the amanda-b10 detector. In: *Phys. Rev. Lett.*, volume 90:p. 251101, 2003. *astro-ph/0303218*.
- [A<sup>+03b</sup>] Ambrosio, M.; et al. (MACRO): Search for diffuse neutrino flux from astrophysical sources with MACRO. In: *Astropart. Phys.*, volume 19:p. 1, 2003. *astro-ph/0203181*.

- [A<sup>+</sup>04a] Ackermann, M.; et al. (AMANDA): Search for neutrino induced cascades with AMANDA. In: *Astropart. Phys.*, volume **22**:p. 127, 2004. [astro-ph/0405218](#).
- [A<sup>+</sup>04b] Ahrens, J.; et al. (the SPASE and AMANDA collaborations): Calibration and survey of AMANDA with the SPASE detectors. In: *Nucl. Instrum. Meth. A*, volume **522**:p. 347, 2004.
- [A<sup>+</sup>05a] Achterberg, A.; et al. (IceCube): The IceCube collaboration: Contributions to the 29th international cosmic ray conference (ICRC 2005), Pune, India, Aug. 2005. In: , 2005. [astro-ph/0509330](#).
- [A<sup>+</sup>05b] Ackermann, M.; et al.: Flux limits on ultra high energy neutrinos with amanda- b10. In: *Astropart. Phys.*, volume **22**:pp. 339–353, 2005.
- [A<sup>+</sup>05c] Aguilar, J. A.; et al. (the ANTARES collaboration): Transmission of light in deep sea water at the site of the Antares neutrino telescope. In: *Astropart. Phys.*, volume **23**:p. 131, 2005. [astro-ph/0412126](#).
- [A<sup>+</sup>05d] Aharonian, F.; et al. (the H.E.S.S. collaboration): A new population of very high energy gamma-ray sources in the Milky Way. In: *Science*, volume **307**:p. 1938, 2005. [astro-ph/0504380](#).
- [A<sup>+</sup>06a] Achterberg, A.; et al. (the IceCube collaboration): On the selection of AGN neutrino source candidates for a source stacking analysis with neutrino telescopes. In: *Astropart. Phys.*, volume **26**:p. 282, 2006. [astro-ph/0609534](#).
- [A<sup>+</sup>06b] Ackermann, M.; et al. (the IceCube collaboration): Optical properties of deep glacial ice at the South Pole. In: *Journ. of Geophys. Res.*, volume **111**(D13203), 2006.
- [A<sup>+</sup>06c] Aynutdinov, V.; et al. (the BAIKAL collaboration): BAIKAL experiment: Main results obtained with the neutrino telescope NT200. In: *Nucl. Instrum. and Meth. in Phys. Res. A*, volume **567**:p. 423, 2006. [astro-ph/0609711](#).
- [A<sup>+</sup>06d] Aynutdinov, V.; et al. (BAIKAL): Search for a diffuse flux of high-energy extraterrestrial neutrinos with the NT200 neutrino telescope. In: *Astropart. Phys.*, volume **25**:p. 140, 2006. [astro-ph/0508675](#).

- [A<sup>+</sup>07a] Aharonian, F.; et al. (the H.E.S.S. collaboration): First ground based measurement of atmospheric Cherenkov light from cosmic rays. In: *Phys. Rev. D*, volume **75**:p. 042004, 2007. [astro-ph/0701766](#).
- [A<sup>+</sup>07b] Amore, I.; et al. (the NEMO collaboration): NEMO: A Project for a km<sup>3</sup> Underwater Detector for Astrophysical Neutrinos in the Mediterranean Sea. In: *IJMPA*, volume **21**:p. 3509, 2007. [arXiv:0709.3991\[astro-ph\]](#).
- [Ack06] Ackermann, M.: *Searches for signals from cosmic point-like sources of high energy neutrinos in 5 years of AMANDA-II Data*. Ph.D. thesis, Humboldt Universität Berlin, 2006.
- [AJY00] Athar, H.; Jezabek, M.; Yasuda, O.: Effects of neutrino mixing on high-energy cosmic neutrino flux. In: *Phys. Rev. D*, volume **62**:p. 103007, 2000. [hep-ph/0005104](#).
- [AMAA] AMANDA home page: <http://amanda.uci.edu/>.
- [AMAB] AMANDA monitoring: <http://butler.physik.uni-mainz.de/>.
- [AUG07] AUGER collaboration: Correlation of the highest-energy cosmic rays with nearby extragalactic objects. In: *Science*, volume **318**:p. 938, 2007.
- [B<sup>+</sup>96] Briggs, M. S.; et al.: BATSE observations of the large-scale isotropy of gamma-ray bursts. In: *Astropart. J.*, volume **459**:p. 40, 1996. [arXiv:astro-ph/9509078](#).
- [B<sup>+</sup>99] Burenin, R. A.; et al.: GRANAT/SIGMA observation of the early afterglow from GRB 920723 in soft gamma-rays. In: *Astron. Astrophys.*, volume **344**:p. L53, 1999. [astro-ph/9902006](#).
- [B<sup>+</sup>00] Bai, X.; et al. (presented by J. Edsjö for the AMANDA Collaboration): WIMP searches with AMANDA-B10. In: *Proceedings of the 3rd International Workshop on the Identification of Dark Matter*. York, United Kingdom, 2000. [astro-ph/0012285](#).
- [B<sup>+</sup>05] Bramall, N. E.; et al.: A deep high-resolution optical log of dust, ash, and stratigraphy in South Pole glacial ice. In: *Geophys. Res. Lett.*, volume **32**:p. 21815, 2005.

- [Bed98] Bednarek, W.: Inverse Compton scattering model for gamma-ray production in MeV blazars. In: *Mon. Not. Roy. Astron. Soc.*, volume **294**:p. 439, 1998. [astro-ph/9711188](#).
- [BNSZ89] Bugaev, E.V.; Naumov, V.A.; Sinegovsky, S.I.; Zaslavskaya, E.S.: Prompt leptons in cosmic rays. In: *Nuovo Cim. C*, volume **12**:p. 41, 1989.
- [BS98] Birkel, M.; Sarkar, S.: Extremely high energy cosmic rays from relic particle decays. In: *Astropart. Phys.*, volume **9**:p. 297, 1998. [hep-ph/9804285](#).
- [BS00] Bhattacharjee, P.; Sigl, G.: Origin and propagation of extremely high energy cosmic rays. In: *Phys. Reports*, volume **327**:p. 109, 2000. [astro-ph/9811011](#).
- [BSK] Bugaev, E. V.; Sokalski, I. A.; Klimushin, S. I.: Simulation accuracy of long range muon propagation in medium: Analysis of error sources. [hep-ph/0010323](#).
- [C+03] Conrad, J; et al.: Including systematic uncertainties in confidence interval construction for Poisson statistics. In: *Phys. Rev. D*, volume **67**:p. 012002, 2003.
- [C+07] Cowen, D. F.; et al. (IceCube): Tau neutrinos in icecube. In: *J. Phys. Conf. Ser.*, volume **60**:p. 227, 2007.
- [CB98] Colafrancesco, S.; Blasi, P.: Clusters of galaxies and the diffuse gamma-ray background. In: *Astropart. Phys.*, volume **9**:p. 227, 1998. [astro-ph/9804262](#).
- [CR] Chirkin, D.; Rhode, W.: Muon Monte Carlo: A high-precision tool for muon propagation through matter. [hep-ph/0407075](#).
- [D+95] Derrick, M.; et al. (the ZEUS collaboration): Measurement of the proton structure function F2 from the 1993 HERA data. In: *Z. Phys. C*, volume **65**:p. 379, 1995.
- [D+00] Digel, S. W.; et al. (the GLAST collaboration): What can GLAST say about the origin of cosmic rays in other galaxies? In: *AIP Conf. Proc.*, volume **528**:p. 449, 2000. [astro-ph/0003407](#).
- [DA81] Dziewonski, A. M.; Anderson, D. L.: Preliminary reference earth model. In: *Phys. Earth Planet. Interiors*, volume **25**:p. 297, 1981.



- [Dav07] Davour, A.: *Search for low mass WIMPs with the AMANDA neutrino telescope*. Ph.D. thesis, Uppsala University, 2007.
- [Dre02] Dremin, I. M.: Cherenkov radiation by particles traversing the background radiation. In: *JETP Lett.*, volume **75**:p. 167, 2002. [astro-ph/0201235](#).
- [DRS00] Dutta, S. I.; Reno, M. H.; Sarcevic, I.: Tau neutrinos underground: Signals of  $\nu_\mu \rightarrow \nu_\tau$  oscillations with extragalactic neutrinos. In: *Phys. Rev. D.*, volume **62**:p. 123001, 2000. [arXiv: hep-ph/0005310](#).
- [EGSL99] Engel, R.; Gaisser, T. K.; Stanev, T.; Lipari, P.: Air shower calculations with the new version of SIBYLL. In: *Proceedings of the 26th ICRC*. Salt Lake City, United States, 1999.
- [F<sup>+</sup>98] Fukuda, Y.; et al. (the Super-Kamiokande collaboration): Evidence for oscillation of atmospheric neutrinos. In: *Phys. Rev. Lett.*, volume **81**:p. 1562, 1998. [hep-ex/9807003](#).
- [FC98] Feldman, G. J.; Cousins, R. D.: A Unified approach to the classical statistical analysis of small signals. In: *Phys. Rev. D*, volume **57**:p. 3873, 1998. [physics/9711021](#).
- [Fer49] Fermi, E.: On the Origin of the Cosmic Radiation. In: *Phys. Rev.*, volume **75**:p. 1169, 1949.
- [Fio01] Fiorentini, Giovanni and Naumov, Vadim A. and Villante, Francesco L.: Atmospheric neutrino flux supported by recent muon experiments. In: *Phys. Lett.*, volume **B510**:p. 173, 2001. [hep-ph/0103322](#).
- [G<sup>+</sup>90] Ginzburg, V. L.; et al.: *Astrophysics of cosmic rays*. North-Holland, Amsterdam, the Netherlands, 1990.
- [G<sup>+</sup>94] Gabriel, T. A.; et al.: Energy dependence of hadronic activity. In: *Nucl. Instrum. Meth. A*, volume **338**:p. 336, 1994.
- [G<sup>+</sup>98] Ghisellini, G.; et al.: A theoretical unifying scheme for gamma-ray bright blazars. In: *Mon. Not. Roy. Astron. Soc.*, volume **301**:p. 451, 1998. [astro-ph/9807317](#).
- [GA03] Guetta, D.; Amato, E.: Neutrino flux predictions for galactic pleions. In: *Astropart. Phys.*, volume **19**:p. 403, 2003. [astro-ph/0209537](#).

- [Gai90] Gaisser, T.: *Cosmic rays and particle physics*. Cambridge University Press, Cambridge, United Kingdom, 1990.
- [GH02] Gaisser, T. K.; Honda, M.: Flux of atmospheric neutrinos. In: *Ann. Rev. Nucl. Part. Sci.*, volume **52**:p. 153, 2002. [hep-ph/0203272](#).
- [GIT96] Gondolo, P.; Ingelman, G.; Thunman, M.: Charm production and high energy atmospheric muon and neutrino fluxes. In: *Astropart. Phys.*, volume **5**:p. 309, 1996. [hep-ph/9505417](#).
- [GK05] Gazizov, A.; Kowalski, M.: ANIS: high-energy neutrino generator for neutrino telescopes. In: *Comput. Phys. Commun.*, volume **172**:p. 203, 2005.
- [Gla60] Glashow, S. L.: Resonant scattering of antineutrinos. In: *Phys. Rev.*, volume **118**:p. 316, 1960.
- [Gla61] Glashow, S. L.: Partial symmetries of weak interactions. In: *Nucl. Phys.*, volume **22**:p. 579, 1961.
- [Gol99] Golec-Biernat, Krzysztof, J. and Wusthoff, M.: Saturation effects in deep inelastic scattering at low  $Q^2$  and its implications on diffraction. In: *Phys. Rev.*, volume **D59**:p. 014017, 1999. [hep-ph/9807513](#).
- [GQRS96] Gandhi, R.; Quigg, C.; Reno, M.H.; Sarcevic, I.: Ultrahigh-energy neutrino interactions. In: *Astropart. Phys.*, volume **5**:p. 81, 1996. [hep-ph/9512364](#).
- [Gre66] Greisen, K.: End to the cosmic-ray spectrum? In: *Phys. Rev. Lett.*, volume **16**:p. 748, 1966.
- [H<sup>+</sup>a] Helbing, K; et al.: Light emission in AMANDA pressure spheres. AMANDA internal report, 2003.
- [H<sup>+</sup>b] Hill, G.; et al.: Ice property investigations with muons and implications for AMANDA analysis. Contribution to the AMANDA Collaboration Meeting, Berkeley, 2002.
- [H<sup>+</sup>94] Hayashida, N.; et al. (the AGASA collaboration): Observation of a very energetic cosmic ray well beyond the predicted 2.7 k cutoff in the primary energy spectrum. In: *Phys. Rev. Lett.*, volume **73**:p. 3491, 1994.

- [H<sup>+</sup>99] Hartman, R. C.; et al. (the EGRET collaboration): The Third EGRET catalog of high-energy gamma-ray sources. In: *Astrophys. J. Suppl.*, volume 123:p. 79, 1999.
- [Hil06] Hillas, A. M.: Cosmic rays: recent progress and some current questions, 2006. astro-ph/0607109.
- [Hör03] Hörandel, J. R.: On the knee in the energy spectrum of cosmic rays. In: *Astropart. Phys.*, volume 19:p. 193, 2003.
- [HP98] He, Y. D.; Price, B.: Remote sensing of dust in deep ice at the South Pole. In: *Geophys. Res.*, volume 103(17141), 1998.
- [HSFP99] Hoffman, C. M.; Sinnis, C.; Fleury, P.; Punch, M.: Gamma-ray astronomy at high energies. In: *Rev. Mod. Phys.*, volume 71:p. 897, 1999.
- [HST<sup>+</sup>] Heck, D.; Schatz, G.; Thouw, T.; Knapp, J.; Capdevielle, J. N.: CORSIKA: A Monte Carlo code to simulate extensive air showers. Technische Report 6019, Forschungszentrum Karlsruhe, Germany, 1998.
- [HT06] Hanson, K.; Tarasova, O. (for the IceCube collaboration): Design and production of the IceCube digital optical module. In: *Nucl. Instrum. Meth. A*, volume 567:p. 214, 2006.
- [Hun99] Hundertmark, S: AMASIM Neutrino Detector Simulation Program. In: *Proceedings of the International Workshop on Simulations and Analysis Methods for Large Neutrino Telescopes*. Zeuthen, Germany, 1999.
- [IT] Ingelman, G.; Thunman, M.: Particle Production in the Interstellar Medium. hep-ph/9604286.
- [Jac52] Jackson, J. D.: *Classical electrodynamics*. John Wiley & Sons, New York, United States, 1952.
- [JKG96] Jungman, G.; Kamionkowski, M.; Griest, K.: Supersymmetric dark matter. In: *Phys. Rept.*, volume 267:p. 195, 1996. hep-ph/9506380.
- [JWDK93] Jadach, S.; Was, Z.; Decker, R.; Kühn, J. H.: The tau decay library TAUOLA: Version 2.4. In: *Comput. Phys. Commun.*, volume 76:p. 361, 1993.

- [K<sup>+</sup>01] Krennrich, F.; et al.: Cutoff in the TeV energy spectrum of Markarian 421 during strong flares in 2001. In: *Astrophys. J.*, volume 560:p. L45, 2001. astro-ph/0107113.
- [K<sup>+</sup>06] Kravchenko, I.; et al.: RICE limits on the diffuse ultra-high energy neutrino flux. In: *Phys. Rev.*, volume D73:p. 082002, 2006. astro-ph/0601148.
- [Kar98] Karle, A.: Monte Carlo simulation of photon transport and detection in deep ice: Muons and cascades. In: *Proceedings of the International Workshop on Simulations and Analysis Methods for Large Neutrino Telescopes*. Zeuthen, Germany, 1998.
- [Kow] Kowalski, M.: On the Cherenkov light emission of hadronic and electromagnetic cascades. AMANDA internal report, 2002.
- [Kow99] Kowalski, M.: *On the reconstruction of cascade-like events in the AMANDA detector*. Master's thesis, Humboldt Universität Berlin, 1999.
- [Kow04] Kowalski, M.: *Search for neutrino-induced cascades with the AMANDA-II detector*. Ph.D. thesis, Humboldt Universität Berlin, 2004.
- [KR05] Klein, J. R.; Roodman, A.: Blind analysis in nuclear and particle physics. In: *Ann. Rev. of Nucl. and Part. Science*, volume 55:p. 141, 2005.
- [KT01] Kowalski, M.; Taboada, I.: Cascade Reconstruction in AMANDA. In: *Proceedings of the 2nd Workshop on Methodical Aspects of Underwater/Ice Neutrino Telescopes*. Hamburg, Germany, 2001.
- [L<sup>+</sup>] Lundberg, J.; et al.: Light tracking for glaciers and oceans: Scattering and absorption in heterogeneous media with photonics. astro-ph/0702108.
- [L<sup>+</sup>00] Lai, H. L.; et al. (the CTEQ collaboration): Global QCD analysis of parton structure of the nucleon: CTEQ5 parton distributions. In: *Eur. Phys. J. C*, volume 12:p. 375, 2000. hep-ph/9903282.
- [L<sup>+</sup>04] Lorenz, E.; et al. (the MAGIC collaboration): Status of the 17-m MAGIC telescope. In: *New Astron. Rev.*, volume 48:p. 339, 2004.
- [Lan05] Lang, R.: *Search for point sources of high-energy neutrinos with the AMANDA detector*. Master's thesis, Universität Ulm, 2005.

- [Lip93] Lipari, P.: Lepton spectra in the earth's atmosphere. In: *Astropart. Phys.*, volume 1:p. 195, 1993.
- [LLD53] Landau L. D., Pomeranchuk I. J.: Limits of applicability of the theory of Bremsstrahlung electrons and pair production at high-energy. In: *Dokl. Akad. Nauk. SSSR*, volume 92:p. 535, 1953.
- [LM00] Learned, J.; Mannheim, K.: High-Energy neutrino astrophysics. In: *New Astron. Rev. Nucl. Part. Sci.*, volume 50:p. 697, 2000.
- [M<sup>+</sup>06] MacTavish, C. J.; et al.: Cosmological parameters from the 2003 flight of BOOMERANG. In: *The Astrophysical Journal*, volume 647:p. 799, 2006. [astro-ph/0507503](#).
- [Man95] Mannheim, K.: High-energy neutrinos from extragalactic jets. In: *Astropart. Phys.*, volume 3:p. 295, 1995.
- [Mar60] Markov, M. A.: *Proceedings of the Rochester Conference on High Energy Physics*. Rochester/Interscience, Rochester, United States, 1960.
- [Mar03] Martin, A. D. and Ryskin, M. G. and Stasto, A. M.: Prompt neutrinos from atmospheric c anti-c and b anti-b production and the gluon at very small x. In: *Acta Phys. Polon.*, volume B34:p. 3273, 2003. [hep-ph/0302140](#).
- [Mig56] Migdal, A. B.: Bremsstrahlung and pair production in condensed media at high energies. In: *Phys. Rev.*, volume 103:p. 1811, 1956.
- [MPE<sup>+</sup>03] Muecke, A.; Protheroe, R. J.; Engel, R.; Rachen, J. P.; Stanev, T.: BL Lac objects in the synchrotron proton blazar model. In: *Astropart. Phys.*, volume 18:p. 593, 2003. [astro-ph/0206164](#).
- [MPR00] Mannheim, K.; Protheroe, R. J.; Rachen, J. P.: Cosmic ray bound for models of extragalactic neutrino production. In: *Phys. Rev. D*, volume 63:p. 023003, 2000.
- [MR93] Meszaros, P.; Rees, M. J.: Relativistic fireballs and their impact on external matter - Models for cosmological gamma-ray bursts. In: *Astrophys. J.*, volume 405:p. 278, 1993.
- [N<sup>+</sup>07] Nysewander, M.; et al.: PROMPT observations of the early-time optical afterglow of GRB 060607A, 2007. [arXiv:0708.3444\[astro-ph\]](#).

- [NMB93] Nellen, L.; Mannheim, K.; Biermann, P. L.: Neutrino production through hadronic cascades in AGN accretion disks. In: *Phys. Rev. D*, volume 47:p. 5270, 1993.
- [Olb03] Olbrechts, P. (for the AMANDA Collaboration): Search for muons from WIMP annihilation in the center of the earth with the AMANDA-B10 detector. In: *Proceedings of the 28th ICRC*. Tsukuba, Japan, 2003.
- [Pan96] Pandel, D: *Bestimmung von Wasser- und Detektorparametern und Rekonstruktion von Muonen bis 100 TeV mit den Baikal-Neutrino teleskop NT-72*. Master's thesis, Humboldt Universität Berlin, 1996.
- [PB97] Price, B.; Bergström, L.: Optical properties of deep ice at the south pole: scattering. In: *Appl. Opt.*, volume 36:p. 4181, 1997.
- [PHO] PHOTONICS tables: <http://photonics.tsl.uu.se/tables.php>.
- [PJ96] Protheroe, R. J.; Johnson, P. A.: Propagation of ultrahigh-energy protons over cosmological distances and implications for topological defect models. In: *Astropart. Phys.*, volume 4:p. 253, 1996. [astro-ph/9506119](https://arxiv.org/abs/astro-ph/9506119).
- [Pon] Pontecorvo, B: *Zh. Exp. Teor. Fiz.* Volume 33:p. 549, 1957.
- [Q+96] Quinn, J.; et al.: Detection of gamma-rays with  $E > 300$ -GeV from Markarian 501. In: *Astrophys. J.*, volume 456:p. L83, 1996.
- [R+96] Rhode, W.; et al. (Frejus): Limits on the flux of very high-energetic neutrinos with the Frejus detector. In: *Astropart. Phys.*, volume 4:p. 217, 1996.
- [Ree84] Rees, M. J.: Black hole models for Active Galactic Nuclei. In: *Ann. Rev. Astron. Astrophys.*, volume 22:p. 471, 1984.
- [Rib] Ribordy, M: AMANDA-II/2000 data statistics, OM selection and retriggering procedure. AMANDA internal report, 2002.
- [Ros52] Rossi, B.: *High-energy particles*. Prentice-Hall, New York, United States, 1952.
- [S+] Sambruna, R. M.; et al. (the HEGRA collaboration): Correlated intense X-ray and TeV activity of Mrk 501 in 1998 June. [astro-ph/0002215](https://arxiv.org/abs/astro-ph/0002215).

- [S<sup>+</sup>98] Sreekumar, P.; et al. (the EGRET collaboration): EGRET observations of the extragalactic gamma ray emission. In: *Astrophys. J.*, volume 494:p. 523, 1998. astro-ph/9709257.
- [S<sup>+</sup>06] Sanchez, G. A.; et al.: Cosmological parameters from CMB measurements and the final 2dFGRS power spectrum. In: *Mon. Not. Roy. Astron. Soc.*, volume 366:p. 189, 2006. astro-ph/0507583.
- [Sal68] Salam, A.: Weak and electromagnetic interactions. In: *Proceedings Of The 1968 Nobel Symposium*. Stockholm, Sweden, 1968.
- [Sch02] Schmidt, T.: *Aufbau und Funktionsnachweis eines Optischen Moduls mit optisch-analoger Pulsübertragung für den AMANDA-II- und IceCube-Detektor*. Ph.D. thesis, Humboldt Universität Berlin, 2002.
- [Sie] Sieglinde program, see the AMANDA software webpage: <http://internal.icecube.wisc.edu/amanda/software/>.
- [Sig98] Sigl, G.: Towards the millennium in astrophysics, problems and prospects. In: *Proceedings of the 10th Course of the International School of Cosmic Ray Astrophysics*. Erice, Italy, 1998.
- [Sig01] Sigl, G.: Ultra-high energy cosmic rays: A probe of physics and astrophysics at extreme energies. In: *Science*, volume 291:p. 73, 2001. astro-ph/0104291.
- [SS96] Stecker, F. W.; Salamon, M. H.: High energy neutrinos from quasars. In: *Space Sci. Rev.*, volume 75:p. 341, 1996. astro-ph/9501064.
- [Ste] Steffen, P., the CORAMA program, see the following webpage: <http://www-zeuthen.desy.de/~steffenp/>.
- [Ste05] Stecker, Floyd W.: A note on high energy neutrinos from AGN cores. In: *Phys. Rev.*, volume D72:p. 107301, 2005. astro-ph/0510537.
- [Sud] Sudhoff, P.: Transmission measurements with AMANDA glass evaluation for IceCube. AMANDA Internal Report 20010701, 2001.
- [Tab02] Taboada, I.: *Search for High Energy Neutrino Induced Cascades with the AMANDA-B10 Detector*. Ph.D. thesis, University of Pennsylvania, 2002.

- [Tar05] Tarasova, O. (for the IceCube collaboration): Design, production, and first results from the ICECUBE digital optical module. In: *Proceedings of the 9th ICATPP Conference on Astroparticle, Particle, Space Physics, Detectors and Medical Physics Applications*. Como, Italy, 2005.
- [Tlu03] Tluczykont, M.: *Beobachtung und Nachweis von Aktiven Galaktischen Kernen und Suche nach Galaktischen Objekten in TeV-Energiebereich mit den HEGRA-Cherenkov-Teleskopen sowie Modellierung eines Photonspektrums durch den Zerfall neutraler Pionen aus schockbeschleunigten Hadronen*. Ph.D. thesis, Universität Hamburg, 2003.
- [VFGS87] Volkova, L. V.; Fulgione, W.; Galeotti, P.; Saavedra, O.: Prompt muon production in cosmic rays. In: *Nuovo Cim.C*, volume 10:p. 465, 1987.
- [Voi] Voigt, B.: Private communication.
- [Vol80] Volkova, L. V.: Energy Spectra and Angular Distributions of Atmospheric Neutrinos. In: *Sov. J. Nucl. Phys.*, volume 31:p. 784, 1980.
- [W<sup>+</sup>04] Wiebusch, C.; et al. (the AMANDA collaboration): Muon track reconstruction and data selection techniques in AMANDA. In: *Nucl. Instrum. Meth. A*, volume 524:p. 169, 2004. astro-ph/0407044.
- [Wal] Walter, M., Relative AMANDA OM's Sensitivity for 2001/2003: [http://www-zeuthen.desy.de/~walter/OMsensitivity/comparison\\_OM\\_sens20012003/omrelsens0103.html](http://www-zeuthen.desy.de/~walter/OMsensitivity/comparison_OM_sens20012003/omrelsens0103.html).
- [WB97] Waxman, E.; Bahcall, J.: High energy neutrinos from cosmological gamma-ray burst fireballs. In: *Phys. Rev. Lett.*, volume 78:p. 2292, 1997. astro-ph/9701231.
- [Wee00] Weekes, T. C.: Status of vhe astronomy c.2000, 2000. astro-ph/0010431.
- [Wei67] Weinberg, S.: A Model of Leptons. In: *Phys. Rev. Lett.*, volume 19:p. 1264, 1967.
- [Wie96] Wiebusch, C.: *Detection of Faint Light in Deep Underwater Neutrino Telescopes*. Ph.D. thesis, Rheinisch Westälische Hochschule Aachen, 1996.



- [Y<sup>+</sup>] Yamamoto, T.; et al. (the Pierre Auger collaboration): The UHECR spectrum measured at the Pierre Auger Observatory and its astrophysical implications. [arxiv:0707.2638\[astro-ph\]](#).
- [Y<sup>+</sup>06] Yao, W. M.; et al. (Particle Data Group): Review of particle physics. In: *J. Phys.*, volume **G33**:p. 1, 2006.
- [ZHV93] Zas, E.; Halzen, F.; Vazquez, R. A.: High-energy neutrino astronomy: Horizontal air shower arrays versus underground detectors. In: *Astropart. Phys.*, volume **1**:pp. 297–, 1993.
- [ZK66] Zatsepin, G. T.; Kuzmin, V. A.: Upper limit on the spectrum of cosmic rays. In: *JETP Lett.*, volume **4**:78, 1966.

\*



# Appendix A

## The Remaining Events

Six events which passed all selection criteria remain in the 5 years of the AMANDA-II data. All of them are illustrated in Figure A.1 as they appear in the AMANDA detector. The sizes of the circles represent the registered amplitudes: the larger the amplitude is, the larger is the circle in the event view. Four of these events appeared in year 2002, one in 2003 and the last event has been registered in the beginning of 2004. All events have an energy larger than 45 TeV. All parameters which have been used for the data selection and characterize the quality of these six events are summarized in Table 9.1.

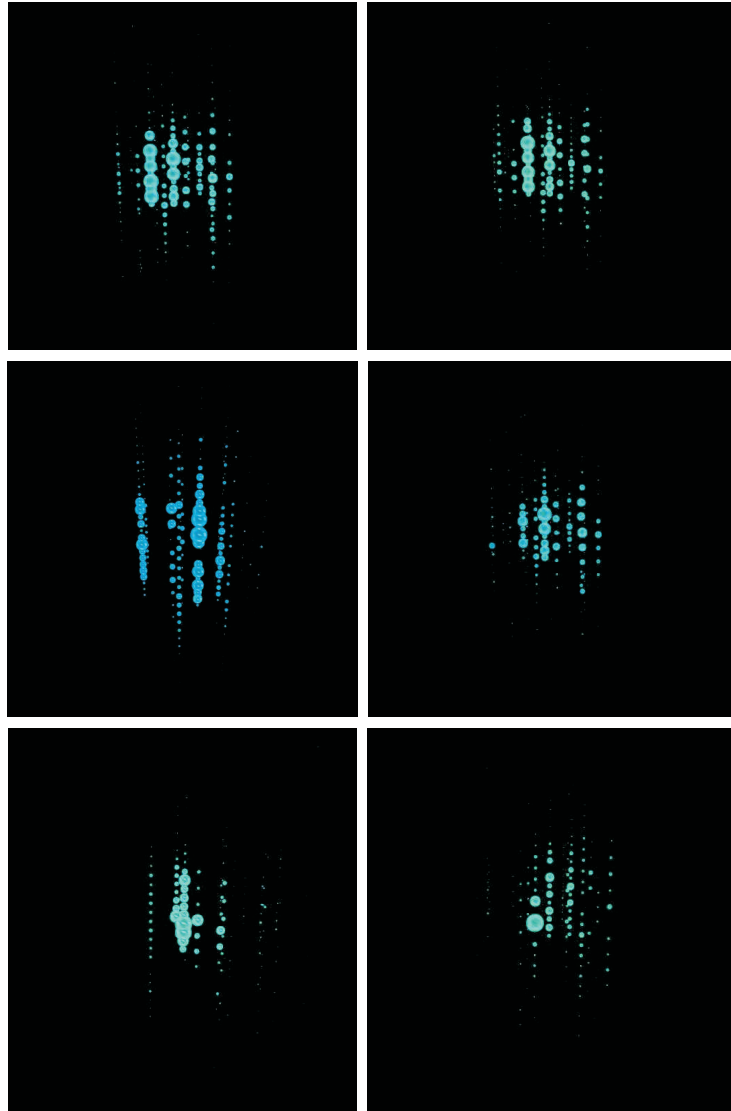


Figure A.1: The six events of the experimental data sample which have passed all the analysis selections are displayed from the side of the AMANDA detector.

# Appendix B

## PTD and Photonics Comparison

In Section 8.1 we introduced the two programs used to describe the properties of the Antarctic ice. In addition, we discussed three signal Monte Carlo samples: PTD, used for this analysis, and PHOTONICS<sub>M</sub> and PHOTONICS<sub>A</sub>, generated for estimating the systematic error due to the simulation of the ice properties.

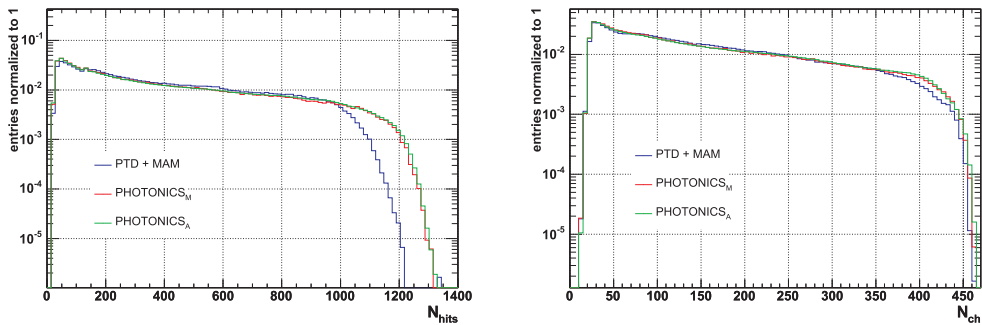


Figure B.1: The number of hits (left) and the number of channels (right) as a comparison of the three signal Monte Carlo samples generated with PTD (blue), PHOTONICS<sub>M</sub> (red) and PHOTONICS<sub>A</sub> (green) tables.

In general, at different reconstruction levels, distributions for PHOTONICS<sub>M</sub> and PHOTONICS<sub>A</sub> look very similar. The distributions obtained with the PTD data are slightly different. This is due to the more accurate modeling of the ice implemented in both PHOTONICS programs, which takes into account the anisotropy of the Antarctic ice. In Figure B.1 one can see the typical characteristics of the data set: number of hits (on the left) and

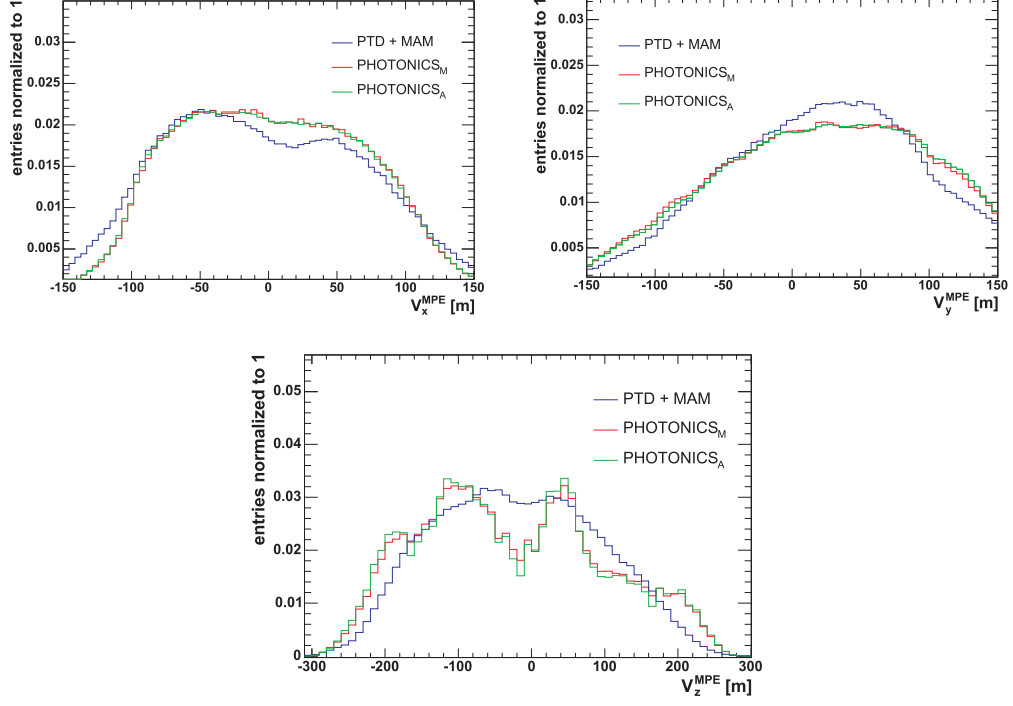


Figure B.2: Distributions of the  $x$ ,  $y$  and  $z$  reconstructed cascade vertex coordinates for the PTD,  $\text{PHOTONICS}_M$  and  $\text{PHOTONICS}_A$  Monte Carlo. All events shown in these distributions passed the vertex likelihood cut  $L_{\text{vertex}} < 7.1$ .

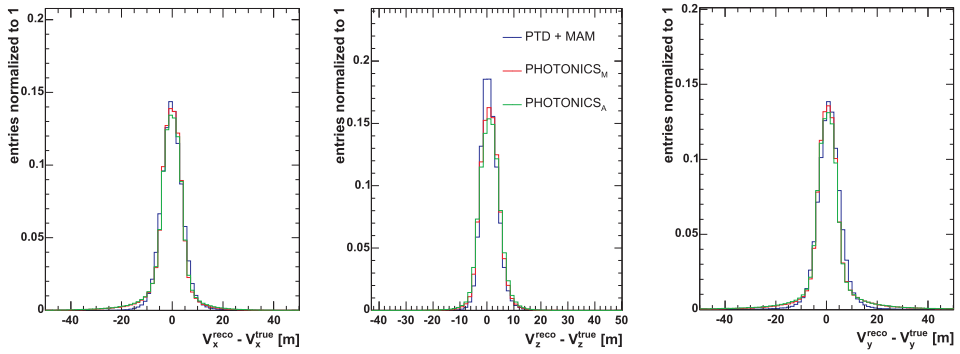


Figure B.3: Resolution of the  $x$ ,  $y$  and  $z$  coordinates for  $\text{PHOTONICS}_M$ ,  $\text{PHOTONICS}_A$  and PTD.

	$\sigma(V_x)$	$\sigma(V_y)$	$\sigma(V_z)$
PTD	4.1 m	4.2 m	2.9 m
PHOTONICS <sub>M</sub>	3.9 m	3.9 m	3.4 m
PHOTONICS <sub>A</sub>	4.0 m	4.0 m	3.5 m

Table B.1: Summary of space resolution for Monte Carlo produced with PTD and PHOTONICS.

number of channels (Optical Modules) fired for each event as a comparison of samples produced with PTD and the two types of PHOTONICS tables.

All PTD, PHOTONICS<sub>M</sub> and PHOTONICS<sub>A</sub> simulations show variations for high-level cascade reconstruction. However, the difference between the two samples generated with PHOTONICS employing different ice models is rather negligible. In Figure B.2 one can see the distribution of the  $x$ ,  $y$  and  $z$  coordinates of the reconstructed cascade vertex. For the  $xy$  plane, also the difference between the PHOTONICS and PTD distributions is not large. For the  $z$  distribution, instead, one can see quite large variations between samples generated with PTD and PHOTONICS. This discrepancy is due to the different ice structure modeling used in each of these simulations. The resolution of the cascade vertex reconstruction (the difference between the reconstructed and generated values of the  $x$ ,  $y$  and  $z$  coordinates) is shown in Figure B.3 for the three signal Monte Carlo samples. A Gaussian function was fitted to all distributions and the parameters of each fit function are summarized in Table B.1. At last, the reconstruction of the cascade energy has been performed using the *phit-pnohit* function, described in Section 6.4. The effect of the implementation of different ice models on the energy reconstruction and on the final result of this analysis is presented in Section 8.1.





# Acknowledgements

I would like to thank Prof. Dr. Hermann Kolanoski for giving me the chance to work at DESY and for taking the responsibility for this thesis. I want also to express my gratitude to Dr. Christian Spiering, who gave me the opportunity to join the AMANDA collaboration and made it possible that I went to the South Pole. It is a great pleasure to thank Dr. Michael Walter for advising me the work on my dissertation and for providing an invaluable help in solving computing problems. I want also to express my gratitude to Dr. Stefan Schlenstedt, for being an excellent group leader during my Ph.D. studies.

I have benefited from the help of Dr. Rolf Nahnauer during the early stage of my work at DESY; his support has been essential when I have been involved in the first year of production and testing of the the IceCube DOMs. I am indebted to many people for the great team work: my co-workers at the DESY site, Reiner Heller, Karl-Heinz Sulanke, Dr. Hubert Waldmann and Bernhard Voigt and colleagues from the University of Wisconsin and Uppsala Universitet, in particular, I would like to mention Prof. Dr. Allan Hallgren, Dr. Kael Hanson, Dr. Jim Haugen, Dr. Mark Krasberg and Jim Braun.

It is a pleasure to thank Dr. Elisa Bernardini, whose suggestions during my Ph.D. studies were always extremely helpful. I enjoyed also numerous fruitful discussions with Dr. Markus Ackermann, who introduced me the principles of the AMANDA data processing. I am indebted to Bernhard Voigt for numerous fruitful conversations and hints on the programming. I would like to thank Dr. David Boersma, Dr. Peter Steffen, Prof. Dr. Christopher Wiebusch Dr. Ralf Wischnewski who developed algorithms and programs for AMANDA data reconstruction and always answered my questions about its implementation.

A special thanks go to Dr. Marek Kowalski, for enlightening discussions in the field of cascade analysis: without him, the analysis shown in this thesis would not have been possible.

I appreciated very much the atmosphere at DESY Zeuthen: many thanks

go to my fellow graduate students Anna Franckowiak, Stefan Klepser, Robert Lauer, Konstancja Satalecka, Sebastian Panknin, Delia Tosi and Bernhardt Voigt, Jose Luis Bazo as well as to the post-docs, Dr. Julien Belmont, Dr. Sebastian Boser, Dr. Martin Tluczykont and Dr. Jens Berdermann, and to the diploma students, Robert Franke, Fabian Kislak, Sirin Odrowski, Anna Mohr.

Many thanks go to the proof readers of my thesis: Dr. Marek Kowalski, Dr. Michael Walter and Bernhardt Voigt.

Finally, thanks to my husband Stefano for enormous support and patience during the most difficult time of my Ph.D. studies !

# Selbständigkeitserklärung

Hiermit erkläre ich, die vorliegende Arbeit selbständig ohne fremde Hilfe verfasst und nur die angegebene Literatur und Hilfsmittel verwendet zu haben.

Oxana Actis

Berlin, den 14 Januar 2008